



Strål
säkerhets
myndigheten

Swedish Radiation Safety Authority

Authors:

Tobias Backers
Tobias Meier
Peter Gipper
Ove Stephansson

Technical Note

2014:10

Rock Mechanics - Confidence of
SKB's models for predicting the
occurrence of spalling

Main Review Phase

SSM perspektiv

Bakgrund

Strålsäkerhetsmyndigheten (SSM) granskar Svensk Kärnbränslehantering AB:s (SKB) ansökningar enligt lagen (1984:3) om kärnteknisk verksamhet om uppförande, innehav och drift av ett slutförvar för använt kärnbränsle och av en inkapslingsanläggning. Som en del i granskningen ger SSM konsulter uppdrag för att inhämta information och göra expertbedömningar i avgränsade frågor. I SSM:s Technical Note-serie rapporteras resultaten från dessa konsultuppdrag.

Projektets syfte

Det övergripande syftet med projektet är att ta fram synpunkter på SKB:s säkerhetsanalys SR-Site för den långsiktiga strålsäkerheten hos det planerade slutförvaret i Forsmark. Projektet undersöker huruvida den möjliga utvecklingen av bergspänningsförhållanden i deponeringsområdet kan leda till spjälkning av deponeringshålen och deponeringstunnlar utöver den omfattning som redovisas i SR-Site. Konsulterna kommer också att utvärdera om förståelsen för spjälkning, uppskattning av dess förekomst och nuvarande osäkerheter är acceptabla ur en vetenskaplig synvinkel vid detta steg i tillståndprocessen. Spjälkning samt dragsprickor kommer att kunna fungera som ledande flödesvägar för vatten samt radionuklider längs med deponeringshålen eller deponeringstunnlarna i slutförvaret.

Författarnas sammanfattning

Denna granskningsstudie placeras inom ramen för SSM:s huvudgranskningsfas för SKB:s säkerhetsanalys SR-Site. Uppdraget benämns "Bergmekanik – Tilltro till SKB:s modeller för att skatta förekomsten av spjälkning". I rapporten presenteras författarnas bedömning som svar på de frågor som SSM har ställt.

Granskningen koncentrerade på två huvudfrågor: (1) analys av de antaganden som gjorts av SKB om bergspänningsfältet vid det planerade slutförvaret för kärnbränsle i Forsmark och (2) analys av potentialen för spjälkning och dragbrott i deponeringshål och deponeringstunnlar i slutförvaret.

Analys av tillgängliga data om bergspänningsfältet kombinerade med strukturgeologiska analyser ledde till slutsatsen att bergspänningsmodellen föreslagen av SKB (kallad "mest trolig spänningsmodell") är osannolik ur ett strukturellt samt geomekaniskt perspektiv och är oförenlig med de hållfasthetsparametrar för bergmassan som är framtagna av SKB. Dock, SKB:s modell kan antas vara konservativ. Omvärderingen av tillgängliga bergspänningsmätningar i kombination med ytterligare beräkningar av möjliga spänningsfält ledde till konsulternas förslag på en alternativ spänningsmodell. Den alternativa bergspänningsmodellen förutsätter en revers regim på förvarsdjup med spänningar $S_v \approx S_h < S_H$ och cirka $S_v \approx S_h = 13$ MPa och $S_H = 35$ MPa på 500 m djup.

Analysen av potentialen för spjälkning och dragbrott byggde på en analytisk beräkning av den tangentiella spänningen vid schaktväggarna i förvaret för ett antal lastfall innefattande schaktning-, drift- och termisk

fas samt istidsscenario. Analysen utfördes för tre befintliga SKB:s bergspänningsmodeller och för konsulternas förslag på en alternativ spänningsmodell.

Det blev tydligt att spjälkning kan förekomma redan under utschaktningssfasen men den är potentiellt allvarlig framför allt under den termiska fasen när spjälkning förväntas inträffa i mer än 90% av deponeringshålen med ett spjälkningsdjup på uppemot flera decimeter.

En numerisk analys antog olika initiala spänningstillstånd, olika spänningsutvecklingar samt ett utvalt istidsscenario. Analysen bekräftade den allmänna uppfattningen som resulterade från de analytiska beräkningarna. För SKB:s bergspänningsmodell samt konsulternas alternativa spänningsmodell är spjälkning sannolik under den termiska fasen. För villkor med låga spänningar, t.ex. i modellen med Ask et al. (2007), skulle endast mindre spjälkning förekomma. En stor osäkerhet finns gällande effekterna på spjälkning av det valda istidsscenario. SKB har antagit flera möjliga scenarier som skiljer sig ganska kraftigt från varandra och som kan påverka spjälkningspotentialen på olika sätt.

Frågan om sprickbildning orsakad av dragspänningar, som inte har diskuterats av SKB i SR-Site, har tagits fram i denna studie. Det finns en tydlig potential för sprickbildning i drag parallellt med tunnlarna för vissa belastningsscenarier. Sådana dragsprickor kan fungera som ledande flödesvägar längs med deponeringstunnlarna i slutförvaret.

Projektinformation

Kontaktperson på SSM: Flavio Lanaro

Diarienummer ramavtal: SSM2011-3630

Diarienummer avrop: SSM2013-2462

Aktivitetsnummer: 3030012-4061

SSM perspective

Background

The Swedish Radiation Safety Authority (SSM) reviews the Swedish Nuclear Fuel Company's (SKB) applications under the Act on Nuclear Activities (SFS 1984:3) for the construction and operation of a repository for spent nuclear fuel and for an encapsulation facility. As part of the review, SSM commissions consultants to carry out work in order to obtain information and provide expert opinion on specific issues. The results from the consultants' tasks are reported in SSM's Technical Note series.

Objectives of the project

The general objective of the project is to provide review comments on SKB's post-closure safety analysis, SR-Site, for the proposed repository at Forsmark. The project explores whether the range of possible evolution of the stress conditions in the deposition volume could lead to spalling of the deposition holes and tunnels outside the extent reported in SR-Site. The consultants should also evaluate whether the understanding of spalling, the estimation of its occurrence and current level of uncertainty are acceptable from a scientific point of view at this stage of the licensing process. Spalling and tensile cracks will serve as leading flow paths for water and radionuclides along the deposition holes and tunnels in the repository.

Summary by the authors

This review study is placed in the context of SSM's Main Review Phase for SKB's safety assessment SR-Site. The assignment is titled "Rock Mechanics – Confidence of SKB's models for predicting the occurrence of spalling". The report presents the authors' assessment in response to the questions raised by SSM.

The review concentrated on two main issues: (1) the analysis of the assumptions made by SKB about the stress field at the planned repository for nuclear fuel at Forsmark, and (2) the analysis of the potential for spalling and tensile failure in deposition holes and tunnels in the repository.

The analysis of the available data on the stress field and additional structural geology based approaches yielded the conclusion that the stress field model proposed by SKB (referred to as "most likely") is unlikely from a structural-geomechanical perspective, i.e. it is inconsistent with strength parameters of the rock mass provided by SKB; however, SKB's model can be assumed to be conservative. Re-evaluating the available stress related data in combination with additional calculations of possible stress field scenarios lead to the proposal of an alternative stress model. The alternative stress model assumes a transpressional stress regime at repository depth with $S_v \approx S_h < S_H$, and about $S_v \approx S_h = 13$ MPa and $S_H = 35$ MPa at 500 m depth.

The analysis of the potential for spalling and tensile failure was based on a straight forward analytical calculation of the tangential stress at the excavation walls for a number of loading cases for the repository, including the excavation, operation and thermal phase as well as glacia-

tion scenario. The analysis was performed for three existing stress field models and for the newly proposed alternative stress model.

It became clear that spalling is an issue already during the excavation phase and spalling is potentially severe during the thermal phase. Spalling can be expected during the thermal phase for more than 90% of the deposition holes, and the calculated spalling depth for certain scenarios is several decimeters deep.

A numerical simulation campaign provided the stress path evolution for different initial stress states and one chosen glacial scenario. These confirmed the general trends found in the analytical calculations. For SKB's stress model as well as for the alternative stress field model, spalling is very likely during the thermal phase. Only for conditions of low stresses as in the model by Ask et al. (2007), minor spalling would be to be expected. A large uncertainty lies in the impact of chosen glaciation scenario on the spalling. SKB provides several possible scenarios that differ quite considerably and that impact differently on the spalling potential.

The issue of stress induced tensile fracturing, which has not been discussed by SKB in SR-Site, has been brought forward in this study. There is a clear potential for persistent tensile fractures parallel to the excavations for certain loading scenarios. Such fractures would serve as conductive fluid pathways along the deposition tunnels in the repository.

Project information

Contact person at SSM: Flavio Lanaro



Strål
säkerhets
myndigheten

Swedish Radiation Safety Authority

Authors: Tobias Backers, Tobias Meier, Peter Gipper
and Ove Stephansson
Geomecon GmbH, Potsdam, Germany

Technical Note 49

2014:10

Rock Mechanics - Confidence of
SKB's models for predicting the
occurrence of spalling

Main Review Phase

Date: December 2013

Report number: 2014:10 ISSN: 2000-0456

Available at www.stralsakerhetsmyndigheten.se

This report was commissioned by the Swedish Radiation Safety Authority (SSM). The conclusions and viewpoints presented in the report are those of the author(s) and do not necessarily coincide with those of SSM.

Contents

1. Introduction	3
2. In situ stress field model	5
2.1. SKB's presentation of the current stress field	5
2.1.1. Stress measurements	6
2.1.2. Comprehensive analyses	12
2.2. Motivation of the Consultants' assessment on the understanding of the stress field	13
2.3. Assessment of the stress modelling	15
2.3.1. Stress polygon analysis	15
2.3.2. Discussion of the validity of the existing stress models	18
2.3.3. Discussion of an alternative stress model	19
2.4. The Consultants' assessment on the stress models	23
2.5. Stress models for further analysis	25
3. Analytical analysis of spalling	27
3.1. SKB's understanding of the potential of spalling	27
3.1.1. Spalling strength	27
3.1.2. Spalling occurrence	29
3.2. Motivation of the Consultants' assessment	30
3.3. Calculation of spalling potential	30
3.3.1. Methodology	30
3.3.2. Employed failure criteria	32
3.3.3. Stress evolution model	33
3.3.4. Results of the analytical spalling analysis	36
3.4. Summary of the analytical analysis of spalling	43
3.5. The Consultants' assessment on analytical analysis of spalling	49
4. Numerical simulation of spalling	51
4.1. SKB's presentation	51
4.2. Motivation of the Consultants' assessment	52
4.3. The Consultants' Assessment on the simulation of stress field evolution and spalling	52
4.3.1. Model description	52
4.3.2. Simulation of temperature evolution	62
4.3.3. Simulation of stress evolution and spalling potential from initial stress field models	62
4.4. The Consultants' assessment on the numerical simulation of spalling	73
5. The Consultants' overall assessment on spalling	75
6. References	77
APPENDIX 1 Coverage of SKB reports	81
APPENDIX 2 Results from analytical spalling analyses	85
Spalling in deposition holes	85
Spalling in deposition tunnels	95
Tensile failure in deposition holes	110
Tensile failure in deposition tunnels	118
APPENDIX 3 Stress data	127

1. Introduction

This report summarizes external review work in the context of SSM's Main Review Phase for SKB's safety assessment SR-Site. The assignment is titled "Rock Mechanics – Confidence of SKB's models for predicting the occurrence of spalling".

This review work explores whether the range of possible evolution of the stress conditions in the repository volume could lead to spalling of the deposition holes and tunnels outside the extent reported by SKB. This review involves independent modelling of rock spalling around the excavations to assess the confidence of SKB's models for predicting the occurrence of spalling at Forsmark.

Moreover, it is evaluated whether the current level of uncertainty of the understanding of spalling, of the rock stresses and their evolution at Forsmark can be considered appropriate prior to proceeding into the construction phase of the repository.

The review consists of three main parts. The first part discusses the current understanding of the in situ stress field at Forsmark. Two main models and some derivatives have been proposed in the past. Out of those SKB is utilising the stress field model termed "most likely" for most of their analyses. This work reviews the validity of the data points, the arguments leading to the conclusions, and continues to propose a stress field model that makes use of the remaining information after ranking the confidence in the stress data available.

The second part summarizes an extensive analytical approach to the stress evolution from present conditions as presented by SKB. The stress evolution during the thermal and glaciation phases will change the stress magnitudes and differential stresses acting on the deposition tunnels and holes. The analytical approach compares the implication for spalling that result from the evolution of the stress field from different present day in situ stress field models as derived in Chapter 2.

In the third part, the repository compartment is modelled using the finite element package COMSOL Multiphysics. The evolution of the stresses is simulated by changing the appropriate boundary conditions on the simplified model. The spalling potential is analyzed by combining the stress history with different spalling criteria to gain an understanding of the robustness of SKB's analysis to predict spalling throughout the lifetime of the repository.

In the context, spalling is understood as any failure of the excavation, i.e. deposition tunnels and holes walls, irrespective if the disintegrated material (fractured rock) may be loose and fall into the excavation. The formation of an excavation disturbed or excavation damage zone (EDZ) is not analyzed, but spalling during excavation of the tunnels and holes may play into the formation of EDZ.

The report presents the authors' assessment in response to the questions raised by SSM as defined in the description of the assignment SSM2013-2462, Activity No 3030012-4061.

2. In situ stress field model

One of the most important aspects in each geomechanical analysis is the appropriate understanding of the stress field, i.e. the in situ stresses including the pore pressure with their spatial and temporal variation. The stresses define the mechanical performance of the rock, the behavior of fractures, fracture networks and faults. The virgin rock stresses also determine the hydraulic behavior of the system. Any geomechanical or geohydraulic model used is generally bound directly or indirectly to the assumptions about the stress field. Hence, the knowledge of the in situ stress field, the pore pressure and their evolution over time is a necessary prerequisite for the analysis of the long term safety of a repository for spent nuclear fuel.

Any inaccuracy in the estimate of the initial stress field will inevitably influence the majority of mechanical interpretations of the repository performance, including safety during construction, spalling during the thermal phase, fracturing in periods of increased fluid pressures during and at the end of glaciation cycles, and the impact of earthquakes on the existing faults and fractures.

Therefore, the existing current stress model of Forsmark by SKB is revisited in this assessment, the proposed models are discussed and an alternative model is presented.

All stresses are denoted using the geomechanical sign convention with compressive stresses taken as positive. All stress orientations are given with respect to magnetic North, using a right-hand rule notation.

2.1. SKB's presentation of the current stress field

SKB mostly rely on the stress field model proposed by Martin (2007), and base most of their geomechanical analyses on that. The stress model indicates a reverse faulting regime. The pore pressure is stated to follow a hydrostatic gradient. The model is referred to as "most likely" in the SKB site reports. In addition a "unlikely maximum stress scenario" and "unlikely minimum stress scenario" are used for selected analyses of the stresses (e.g. SKB R-08-116).

An alternative stress model for the repository site based on hydraulic stress measurements was proposed by Ask et al. (2007). It promotes both lower differential stress and stress gradients compared to Martin (2007), indicating a strike-slip faulting regime. SKB's "unlikely minimum scenario" is similar to the model of Ask et al. (2007) for the repository depth (Table 2.1)

Figure 2.1 summarizes SKB's current understanding of the stress field at the Forsmark site. The depicted data (maximum horizontal stress, minimum horizontal stress and vertical stress, all assumed to be principal stresses) consists to a large percentage of overcoring (OC) measurement results for the depth interval 0-500m; but also a stress model based on hydraulic fracturing (HF) and hydraulic testing of pre-existing fractures (HTPF) data at 500m below ground surface. The direction of the principal stresses is generally consistent between the presented models, however varying by 20°. The vertical stress is calculated from the weight of the overburden of the rock mass.

Table 2.1: Stress magnitudes at repository level for the high stress and low stress models at a depth of 500 m.

S_H [MPa]	S_h [MPa]	S_v [MPa]	P_p [MPa]	Stress regime	Reference
41.0 ± 6.2	23.2 ± 4.6	13.3 ± 0.3	5	reverse	SKB's "most likely", Martin (2007, SKB R-07-26)
22.7 ± 1.1	10.2 ± 1.6	13	5	strike-slip	SKB's "unlikely minimum" (SKB R-08-116)
56 ± 6 *)	35 ± 15 *)	13.3 ± 0.3	5	reverse	SKB R-08-116 SKB's "unlikely maximum"
22.7 ± 1.1	10.2 ± 1.6	13	5	strike-slip	Ask et al. (2007, SKB P-07-206)

*) for 475 m. SKB's "unlikely minimum" stress field makes no reference to Ask et al. (2007), but appears astonishing similar.

The regression lines presented in Figure 2.1 (red) are based on the overcoring measurements only. Omitting data that is assumed to be of low confidence without further justification, the regression shows a bi-linear fit for the minimum horizontal stress and a three-linear fit for the maximum horizontal stress. Consistently for both the maximum and minimum horizontal stress, the first change in slope is at the transition from fracture domain FFM02 to FFM01 at about -150 m. It is argued by SKB that this change in stress gradient could be related to the change in fracture densities in the two fracture domains. The second change in slope at about -400 m does not coincide with a change of geological conditions in situ. The change in slope is only applied to the maximum horizontal stress and not for the minimum horizontal stress.

The data from the hydraulic stress measurements are not used in SKB's modelling of the stress field for Forsmark. The arguments brought forward to exclude the data are given in the SKB's Site Descriptive Model Report (SKB TR-08-05, p.216) are:

- It is suspected that the hydraulic measurements do not measure the correct minimum horizontal stress, but rather the vertical stress (reference to SKB R-07-26), and
- The results do not indicate that a thrust regime is prevailing, and this does not agree with the evaluated state of stress in the Fennoscandian shield (reference to Stephansson et al., 1991).

2.1.1. Stress measurements

There have been a number of stress measurement campaigns at the Forsmark site until 2007. Table 2.2 lists the reports that document the measurements together with those that re-evaluate single measurement campaigns. Additionally, two comprehensive stress analyses have been carried out. Those are Sjöberg et al. (2005) who evaluate the data collected during 2004 and earlier, and Martin (2007) that presents the most recent stress analysis. The boreholes that have been tested are located at the drill sites shown in Figure 2.2.

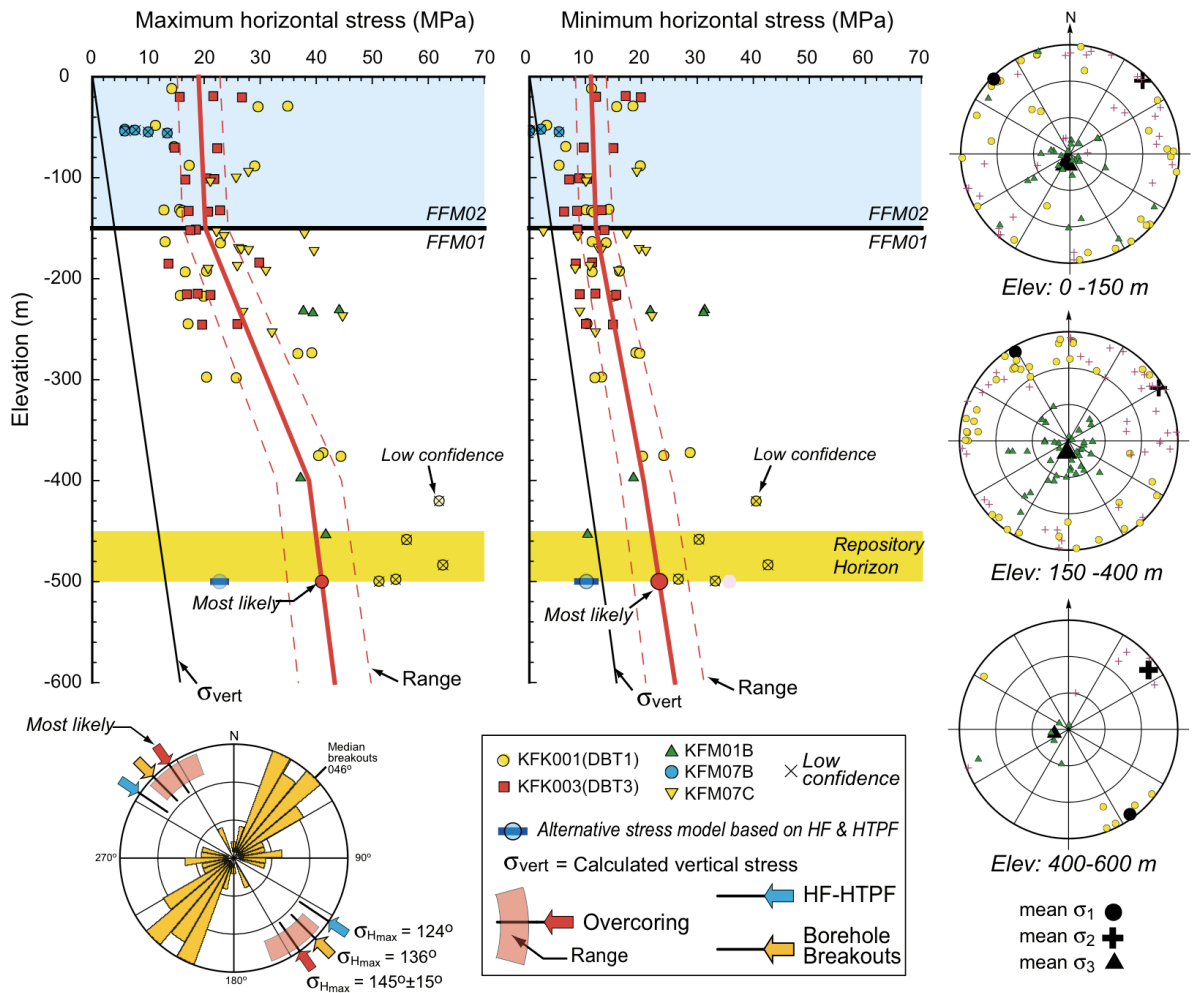


Figure 2.1: SKB's in situ stress field model for fracture domains FFM01 and FFM02 with selected data from stress measurements (from SKB TR-10-52, p.293, Figure 6-48).

Many stress measurements have failed or delivered unreliable results due to difficulties that come along with the specific methods that have been employed. As indicated above, the two methods that are somewhat competing due to varying results are the overcoring method and hydraulic tests. The following chapter presents an overview on the reports with focus on difficulties during the measurements and validity of the presented data points. The problems associated with the measurement of stress and strain in the Earth crust are manifold, especially at the Forsmark site, but only the main findings are summarised here.

Overcoring stress measurements in boreholes DBT1 and DBT3

The first stress measurements were performed by Ingevald and Strindell (1981) in boreholes DBT1 and DBT3 during the construction of the Forsmark Power Plant 3. They used the overcoring method and worked with the prototype of the Swedish State Power Board (SSPB) stress cell, which did not record strain readings during the overcoring process. The according reports have later been revisited by Perman and Sjöberg (SKB P-03-119, 2003) and some unexplained inconsistencies were

found between the reported stresses in different reports (Ingevald and Strindell 1981; SSPB 1982), in the order of few MPa. Also, there are some uncertainties regarding the reported testing results for the elastic constants, E and ν , as it was not clear whether the presented values represent axial or horizontal direction or an average of those. Those constants were tested in a concrete testing machine that probably has a softer loading frame than today's state of the art. No further elaboration on the effect is presented, as there are no details given on the testing machine in the reports.

Table 2.2: Overview of reports on stress measurements. The borehole numbers and type of measurement are shown where measurements have been performed. Boreholes are marked with an x where measurements have been reviewed by the respective authors. OC: overcoring, HF: hydraulic fracturing.

Report	Author	Year	Borehole number														
			01A	01B	02A	02B	04A	07A	07B	07C	08A	09A	09B	DBT1	DBT3		
L-543:2	Ingevald, Strindell	1981														OC	OC
P-03-119	Perman, Sjöberg	2003														x	x
P-04-83	Sjöberg	2004		OC													
P-04-311	Klee, Rummel	2004	HF	HF	HF		HF										
P-04-312	Rummel, Weber	2004	x	x	x		x										
R-05-35	Sjöberg, Lindfors, Perman, Ask	2005	x	x	x		x									x	x
P-05-66	Lindfors, Perman, Sjöberg	2005		x													
P-06-93	Lindfors	2007								OC							
P-07-130	Lindfors, Perman, Berg, Ask	2007									OC						
P-07-205	Lindfors, Berg, Perman	2007					OC										
P-07-206	Ask, Cornet, Brunet, Fontbonne	2007							HF		HF	HF	HF	HF			
P-07-234	Ask	2007	x	x	x		x									x	x
R-07-26	Martin	2007	x	x	x	x	x	x			x	x	x	x	x	x	x

Successful measurements were carried out in DBT3 until its final depth of 250m. In the 500m deep borehole DBT1 extensive core dinking hampered the measurements at depths below 320m. In the original measurement report of Ingevald and Strindell (1981) the measurements were interpreted to show a jump in horizontal stresses at 320m depth. After re-evaluation however, it has been shown that the data can be fit to a linear increase of stress vs. depth. The number of data points is apparently too low to conclusively state either of the two possibilities. Perman and Sjöberg (2003)

performed a transient strain analysis after the method of Hakala et al. (2003) and found that below 250m the amount of unexplained strain is exceptionally high and tensile stresses become high enough to likely damage the overcored sample which influences the test results.

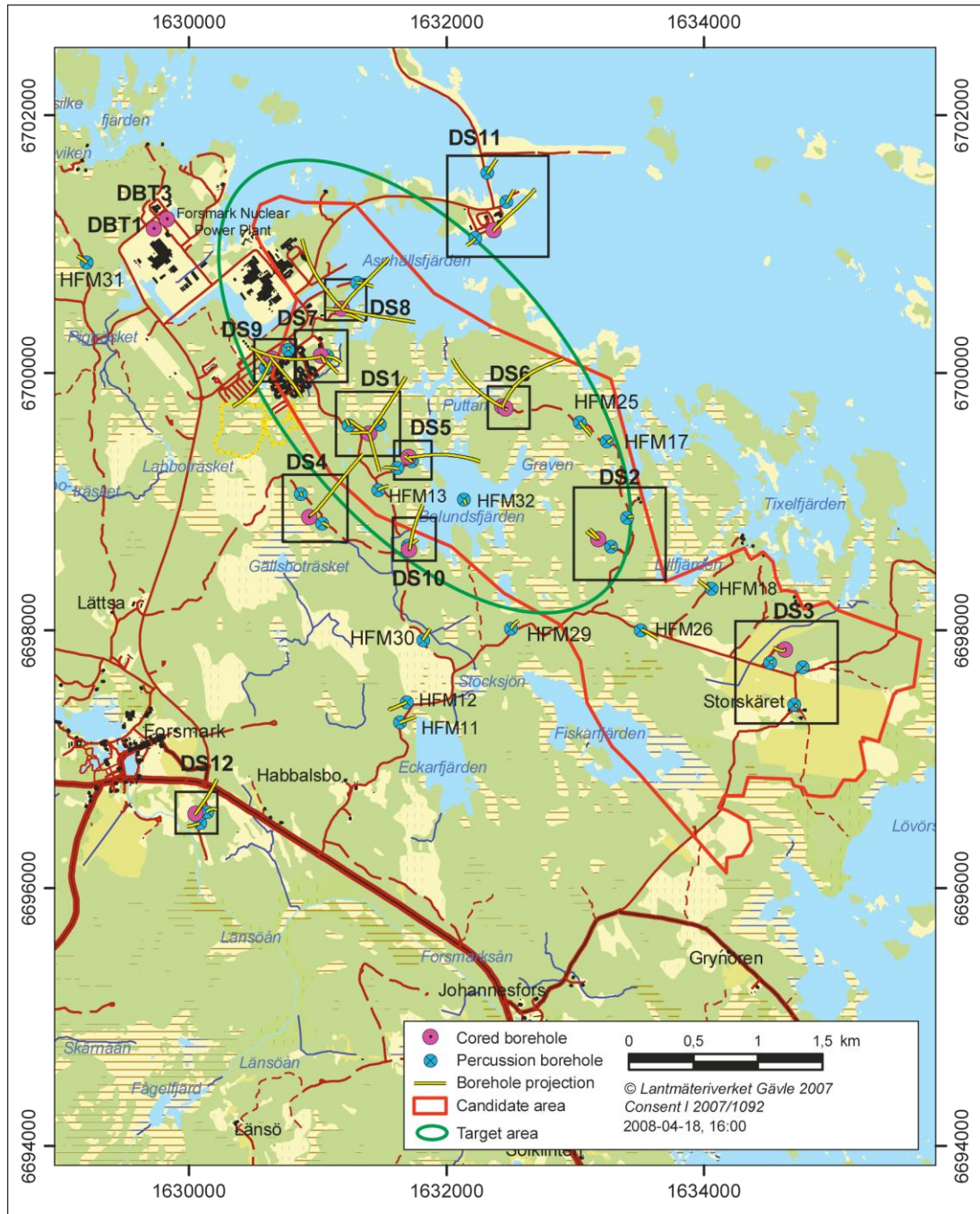


Figure 2.2: Location of relevant drill sites with respect to the Forsmark candidate area. Drill sites of boreholes DBT1 and DBT3 are located outside the candidate area in the northwest corner of the map (redrawn from Figure 4-5, SKB TR-11-01).

Overcoring stress measurements in borehole KFM01B

Sjöberg (SKB P-04-83, 2004) presents overcoring stress measurements from two intervals in borehole KFM01B. The interval ranges of depth were 233 m-236 m (level 1) and 399 m-455 m (level 2). Tests at the deeper level yielded anomalous low stresses. The basic conclusion is that horizontal stresses are “high”, as indicated by occurrence of core diskings and the obtained maximum horizontal stress magnitudes of around 40 MPa for both depth intervals. The author does not give magnitudes for the intermediate principal stress that should in theory have the same confidence level as the maximum principal stress. During the measurements there were massive difficulties leading to resulting vertical stresses that strongly deviate from the theoretical lithostatic stress. Extensive core diskings, especially in the deeper interval, and probably microcracking due to high tensile stresses that developed in axial direction during overcoring, as evident from the transient strain analysis presented by Sjöberg (2004), lead to overestimation of the vertical stress. No stress gradients are derived from the measurements, as they would imply decrease of stresses with depth which is unlikely to be the case. Locally this effect is interpreted to be caused by increase in fracture density from level 1 to level 2. A recalculation of the magnitudes (Lindfors et al., 2005, SKB P-05-66), where the vertical stress was forced to fit the theoretical overburden, yielded slightly lower magnitudes and positive gradients for the maximum horizontal stress and the vertical stress.

Indirect methods were employed to estimate likely ranges of horizontal stress. Indicators were the occurrence of core-disking and spalling.

Overcoring stress measurements in borehole KFM07B

Overcoring measurements in KFM07B presented by Lindfors (2007, SKB P-06-93) were planned at six different depth intervals. Attempts were only made in levels 1 to 3. The only measurements that are considered successful were those at level 1 between 67 m and 73 m depth. Due to debonding of the strain gauges from the pilot hole wall during the overcoring process, the obtained strains and hence also the calculated stresses were unrealistically low (cf. Figure 2.1). Apparently the reasons for debonding were difficulties in cleaning the relatively shallow dipping borehole (55°) from drilling debris. The results presented for level 1 are ambiguous with respect to the orientation of the maximum horizontal stress, which is a typical observation for the whole upper bedrock at Forsmark.

Overcoring stress measurements in borehole KFM07C

Lindfors et al. (2007, SKB P-07-130) conducted overcoring measurements at six depth intervals in KFM07C of which the measurements at first four levels were judged successful. At levels 5 and 6 no realistic results could be obtained due to extensive ring diskings and fractures occurring parallel to the borehole axis. Transient strain analysis shows that there is relatively high amount of unexplained strain. Tensile stresses of around 14 MPa were inferred, that are large enough to cause damage in the overcored samples. Inverse solutions for stress determination were attempted for the transient strain tests. No stable stress values were obtained for the pre-overcoring phase leading to the conclusion that it was not possible to determine the stresses with any reliability. The stress state could not be unambiguously determined for any of the measurements levels, as stated by the authors. Apparently there is a temperature effect on the observed strains, but it could not be quantified. The authors tried to minimise the influence by carefully selecting the strains used to calculate the stresses, however, the error of the results could not be assessed.

Overcoring stress measurements in borehole KFM02B

For the results of measurements in KFM02B presented by Lindfors et al. (2007, SKB P-07-205), a very similar conclusion to that for borehole KFM07C has been drawn. Although at 3 out of 4 levels measurements could successfully be obtained, after transient strain analyses and calculation of the inverse solution for the pre-overcoring phase, still, no stable stresses could be obtained and hence the resulting state of stress is not thought to be reliable.

Hydraulic stress measurements in boreholes KFM01A, KFM01B, KFM02A and KFM04A

The first hydraulic measurements were carried out by Klee and Rummel (2004, SKB P-04-311) in boreholes KFM01A, KFM01B, KFM02A and KFM04A. They conducted hydraulic fracturing tests and hydraulic injection tests on pre-existing fractures. For the latter, a pre-existing fracture with known orientation is hydraulically reopened and the applied pressures are monitored in order to estimate S_H once S_h is obtained with the hydraulic fracturing technique. Many attempts of HTPF showed distinct breakdown events, corresponding to initiation of new fractures, indicating that the pre-existing fractures have partly been healed.

From successful measurements (60 HF, 25 HTPF) the stress gradients are calculated assuming a linear stress-depth relationship. The vertical stress generally mirrors the calculated overburden. Stress gradients are derived for each borehole. The minimum horizontal stress is the intermediate principal stress, but becomes the smallest principal stress at 500m for boreholes KFM01A/B, thus marking a transition from reverse faulting to strike-slip faulting regime. For borehole KFM02A this transition is also observed in the solution, but takes place at larger depths. The authors conclude that tests at the Forsmark area indicate that a reverse faulting to strike-slip faulting regime is prevailing and the maximum horizontal stress is oriented NW-SE. Locally elevated stresses as inferred from overcoring measurements are not excluded. Some measurements were neglected that showed abnormally high (KFM01B, KFM04A) or low (KFM02A) resulting maximum horizontal stresses and were deviating from the linear trend. The authors therefore emphasise that the derived stress field represents the general state of stress at the Forsmark area, not taking into account local variations.

Hydraulic stress measurements in boreholes KFM07A, KFM07C, KFM08A, KFM09A and KFM09B

A second campaign of hydraulic testing was carried out by Ask et al. (2007, SKB P-07-206). HF and HTPF tests were performed in boreholes KFM07A, KFM07C, KFM08A, KFM09A and KFM09B. Additionally analysis of packer induced fractures provided quality control of the derived results. During the measurements, a common problem was the generation of sub-horizontal fractures, mostly located towards the end of the testing interval, thus probably packer-induced. This reduced the amount of unambiguous data that could be obtained. Especially at drill sites 8 and 9, no true hydraulic fractures could be obtained since in order to do so, the borehole needs to be parallel to a principal stress direction, which is not given at those drill sites. Of a total of 87 tests, only 45 provide unambiguous data, showing reliable normal stress and fracture geometry.

The collected data was evaluated using the inversion method (Cornet, 1993). Depending on the number of measurements, the number of model parameters that

are solved is varied. Usually a linear stress-depth relation is assumed and lateral stress gradients neglected. Rotation of horizontal stresses is accounted for in parameterization where enough measurement points are available, providing an unconstrained solution, as opposed to constrained solution where parameters are assumed to be known a priori. The best solution was obtained for drill site 7, combining HF data from a vertical (KFM07C) and HTPF data from an inclined borehole (KFM07A) and has been validated to fit the geometry of observed packer induced fractures. Therefore the solution is thought to best represent the state of stress at repository depth and is given for depths of 400 m and 500 m (cf. Table 2.1).

2.1.2. Comprehensive analyses

In addition to the reported measurements there have been comprehensive analyses of the available stress data at Forsmark. Those are Sjöberg et al. (2005, SKB R-05-35), who reviewed the stress measurements carried out in 2004 and earlier, and Martin (2007), where SKB's "most likely" stress model is derived. Additionally there has been a review and re-calculation of selected measurements in Ask (2007, SKB P-07-234).

The review by Sjöberg et al. (2005) concludes that the faulting regime corresponds to thrust faulting or possibly strike slip faulting. For the depth interval between 230m and 450m they obtain a single stress gradient for the vertical and minimum horizontal stress ($S_v=S_h=0.0265z$) and upper and lower limit stress gradients for the maximum horizontal stress. In contrast to preceding studies, core disking was used to establish an upper bound on the maximum horizontal stress in areas with no observed core disking. They observe that the scatter in results obtained by overcoring measurements is larger than for hydraulic tests and consider the possibility that this is related to the size of the testing volume, which is significantly smaller for the overcoring method compared to hydraulic testing. Therefore, this method is more sensitive to local rock heterogeneities. The major limiting factor in overcoring measurements is the occurrence of core disking, making the measurements less reliable beyond a certain depth. Also, without ring disking being observed, the tensile strain in axial direction of the cored sample leads to microcracking, causing anomalies in the measured strain. This effect is likely pronounced due to the relatively small 76mm borehole diameter for the Borre probe used for the measurements. The advantage however is that the method provides a fully, three-dimensional stress tensor.

Sjöberg et al. (2005) compare hydraulic and overcoring methods on the basis of measurements in boreholes DBT1 and KFM01B where both methods have been applied. HF measurements in DBT1 were presented by Stephansson and Ångman (1986) and yield stress magnitudes that are generally smaller compared to overcoring. Vertical stress magnitudes are closer to the theoretical vertical stress calculated from the overburden. The minimum horizontal stresses are lower, too, and the maximum horizontal stresses are significantly lower. It is recommended to regard the maximum horizontal stress obtained from hydraulic methods as a lower limit.

The same report by Sjöberg et al. (2005) provides a review of stress data from Finnsjön, at 15 km distance from the Forsmark area, where stress measurements have been performed in 1987 and are presented by Bjarnason and Stephansson (1988). The minimum horizontal stress approximately equals the theoretical vertical stress due to overburden pressure. The maximum horizontal stress is 1.5 times the

vertical stress, but cannot be reliably estimated with hydraulic fracturing measurements only.

Martin (2007, SKB R-07-26) carried out a comprehensive analysis of stress measurements at the Forsmark site that culminates in SKB's "most likely" stress model that divides the stress gradients in three depth intervals. In order to establish depth ranges for constant gradients, the data is analysed in terms of mean stress $M = (S_1 + S_2 + S_3) / 3$, and four intervals of constant mean stress are identified (Figure 2.3, 0 to 150 m, 150 to 300 m, 300 to 400 m and 400 to 500 m). For those depth ranges, the horizontal stress magnitudes are calculated using the mean stress and the stress ratio S_1/S_2 , which is suggested to lie around 1.7 from the overcoring data. Subsequently, stress gradients for three depth ranges 0 to 150 m, 150 to 400 m and 400 to 600 m are established (cf. Figure 2.1). It is not stated how they are established, nor why the change in mean stress at 300 m is neglected. The increase in mean stress is speculated to represent improvements in rock mass quality, i.e. decrease of fracture density.

It is not clear from the report which overcoring measurements were judged valid and employed for establishment of the presented stress gradients. In the conclusions by Martin (2007), it is stated that 72 overcoring measurements have been used, which are several than reported in Table A-1 (Martin, 2007).

Martin (2007) also performed transient strain analysis and revisited the unexplained strains to find that they are likely thermally induced. The extent of the effect is however not quantified yet which theoretically renders all overcoring measurements as unreliable. The stress ratios are however thought to not be influenced much, which is the reason why Martin (2007) used those stress ratios in order to estimate the state of stress at the Forsmark site.

2.2. Motivation of the Consultants' assessment on the understanding of the stress field

As emphasized in the introduction to the assessment of rock stress, the understanding of the stress field is crucial for any further geomechanical analysis. Therefore, the authors revisited the arguments by SKB that yielded in the proposed stress model. The following issues were found to be worth consideration.

The changes in stress gradients with depth show some inconsistency for S_H and S_h :

- Whereas the first change in S_H slope is believed to be due to a change in fracture densities in the different domains, the second change in slope at about -400m is not supported by the presented data and it lacks geological validity.
- The change in slope is only plotted for the maximum horizontal stress, but the change should most likely be visible also in the minimum horizontal stress gradient. This is not the case.

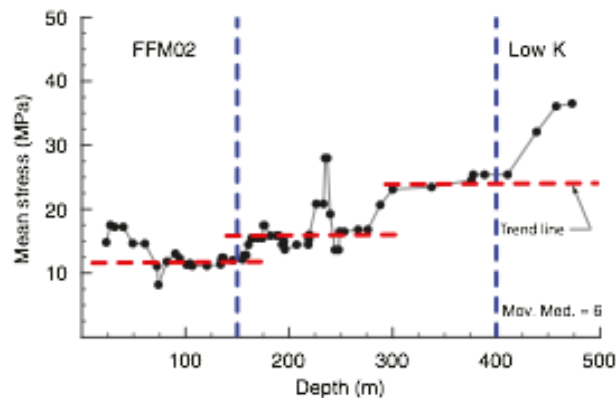


Figure 2.3: Intervals of constant mean stress as obtained by Martin (2007; from R-07-26, p.62, Figure 6-5).

- It is possible to plot a linear regression of the maximum horizontal stress in the interval 150 m to 500 m; the resulting deviation from the data would be about the same as for the minimum horizontal stress.

The argument that the hydraulic data contradicts the overcoring measurements is believed not to be relevant for the following reasons:

- Some of the data points from overcoring are considered to be of low confidence. These are in particular the very high stress magnitudes measured in DBT1 at about 450 m to 500 m. Therefore, there is only one overcoring measurement below 400 m, i.e. from KFM01B. This data point suggests $S_H \approx 40$ MPa and $S_h \approx 10$ MPa. The minimum horizontal stress is very similar to the hydraulic data at that depth and very close to the vertical stress, too, and therefore the argument that the hydraulic data contradicts the overcoring measurements is weak. Interestingly, S_V and S_h are very similar at 500 m, giving evidence of a transitional stress regime at that depth.
- The boreholes DBT1 and DBT3 were drilled during the construction of the third reactor of the power-plant during the period 1977 to 1979 (SKB R-05-35) and are located outside the target area of the repository (Figure 2.2). Furthermore, the measurements were performed with the precursor of today's Borre probe. The location of both boreholes is outside the candidate area in a different rock domain; hence it is highly questionable if the data are valid and should be used for the modelling of the stress field.

The choice of data points that lead to the current “most likely” stress model by SKB appears to follow biased arguments:

- The measurements that are considered valid in SKB's most likely model are overcoring measurements only (Table A-1, SKB R-07-26). The majority of those measurements were performed in boreholes DBT1 and DBT3, outside the target area with prototype equipment.
- It is unclear which overcoring measurements were finally used for the SKB's most likely stress model. The data shown in Appendix A in Martin (2007) does not coincide with the data depicted in Figure 7-18 of the Site Descriptive Model Report (SKB TR-08-05, Figure 2.1) nor with the precursor of this figure which is Figure 7-3 in Martin (2007). The figure is

therefore somewhat misleading since one would assume that the shown data provides the basis for the depicted stress gradients. Also it is not clear why some data points classified as unreliable by SKB are presented in Figure 2.1 and others are not.

Considering the aforementioned discussion points, the database for the stress modelling reduces significantly. In consequence only the hydraulic measurements and selected measurements from KFM07C (confined to 100 m-250 m depth) should, in the authors' opinion, be considered. The remaining data suggests a transitional stress regime at repository depth with $S_H > S_h = S_v$. Therefore, the stress field model is further scrutinized in the following sections.

2.3. Assessment of the stress modelling

The two existing stress models for Forsmark (Ask et al., 2007, Martin 2007) differ significantly from each other in magnitudes of the principal stresses, and even suggest different faulting regimes. The stresses inferred from the overcoring data are systematically higher than the ones from hydraulic fracturing tests.

In the argumentation why the hydraulic data should be omitted, SKB stated that the results do indicate a strike slip regime, contradicting the general trend in the Fennoscandian shield (reference to Stephansson et al., 1991). With respect to that reference it has to be noted that Stephansson et al. (1991) suggest like Ask et al. (2007) a transition at depth from thrust faulting to strike-slip faulting, with the difference of proposing a larger depth where the vertical stress equals the minimum horizontal stress (about 800m). The model suggested by Martin (2007) shows diverging trends of S_h and S_v . Also the horizontal stresses derived in Stephansson et al. (1991) are closer to the stress field presented by Ask et al. (2007) than to SKB's "most likely" stress model for the repository depth. This could be related to the identical principle of measurement (hydraulic) being employed. The target area is in a compartment surrounded by large fault zones and additional smaller faults, hence local variation of stresses at the Forsmark site cannot be excluded.

The approach of establishing stress gradients for SKB's "most likely" model appears unique. Considering not only isolated measurements, trends in the mean stress are established and used to define compartments for which stress gradients are derived. The advantage of this method is that it allows for stress gradients to change with depth instead of assuming a constant linear stress-depth relationship and thus accounting for possible changes in geological conditions. At the same time, changes of stress gradients are forced by this method and will likely be introduced also where they do not reflect a change of the geology but scatter in the dataset.

2.3.1. Stress polygon analysis

To further analyse the situation, a stress polygon analysis for the reservoir depth is performed (Figure 2.4).

Stress magnitudes at depth are limited by the strength of the rock mass. Planar discontinuities are usually widely distributed in different orientations in the crust and they show reduced frictional strength. The magnitudes of principal stresses and the differential stresses are therefore limited, as they cannot exceed the frictional strength of the discontinuities.

Assuming that preexisting shearing planes with friction coefficient μ exist at any orientation relative to the principal stresses, one can calculate the stable stress field configurations. As given in Jaeger et al. (2007), the ratio of principal effective stresses for the frictional limit is given as:

$$(\sigma_1 - P_p) / (\sigma_3 - P_p) = ((\mu^2 + 1)^{1/2} + \mu)^2 \quad \text{Eq. (2.1)}$$

where σ_1 and σ_3 are the maximum principal stress and minimum principal stress, respectively, and P_p is the pore pressure. One can thus give boundaries for a given depth, friction coefficient and pore pressure for the different stress regimes.

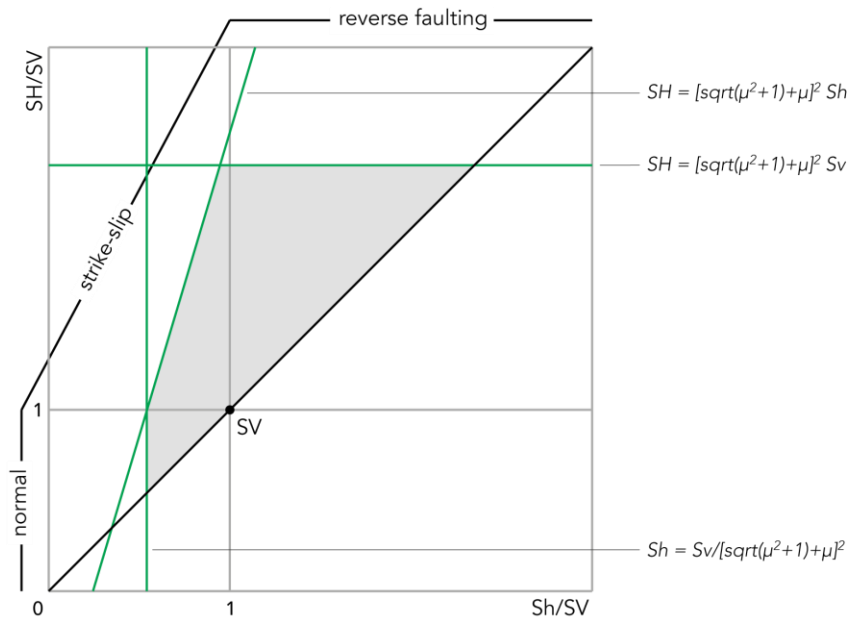


Figure 2.3: Possible states of stress at any crustal depth, determined after the concept of limiting stress ratios (after Peška and Zoback, 1995). Green lines: frictional limits for the respective stress regimes.

In a normal faulting regime the criterion defines the lower bound of S_h . For any lower magnitudes a critically oriented fault would slip. For strike slip faulting, the largest possible magnitude of S_H depends on the magnitude of minimum horizontal stress S_h as the friction coefficient defines an upper bound for the ratio S_H/S_h . For the reverse faulting regime one obtains an upper bound of the maximum horizontal stress depending on the vertical stress.

For assessment of the suggested in situ stress fields, the authors consider two cases of frictional strength. As friction angle for fractures, the value for fracture domain FFM01 of 35° ($\mu = 0.7$) was taken, which is relevant for the target area at depth (SKB R-07-31, p.66, Table 4-14). In order to test the reactivation potential of existing faults, the residual frictional strength was used, which additionally represents the more conservative approach since they are slightly lower than the peak values.

Additionally, a friction angle of 40° ($\mu = 0.84$) was considered according to Byerlee (1978) for intact rock, which is much lower and hence more conservative than the

reported 60° for the intact rock at Forsmark. By also considering failure of intact rock, one can conveniently exclude stress fields that exceed the frictional strength of the intact rock and test if the suggested stress fields lie within that range.

The vertical stress S_V at the lower limit of repository depth of 500 m is 13.3 MPa, calculated with mean density of 2700 kg/m^3 (SKB TR-10-52, p.293, Table 6-50). Pore pressure at that depth is assumed to be hydrostatic ($P_p = 5 \text{ MPa}$).

The resulting stress polygon plots are given in Figures 2.4 and 2.5.

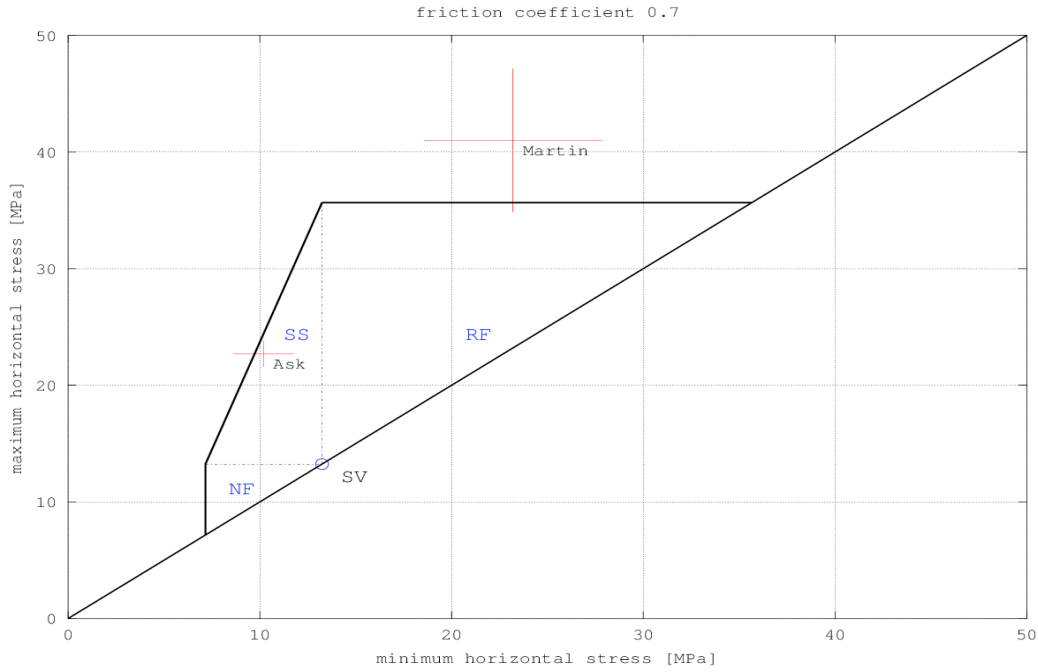


Figure 2.4: Stable stress fields regarding potential fault reactivation with a frictional coefficient of $\mu = 0.7$ at 500m depth. The stress models incl. their uncertainty (red cross) by SKB “most likely” (Martin, 2007) and Ask et al. (2007) are shown in the stress space.

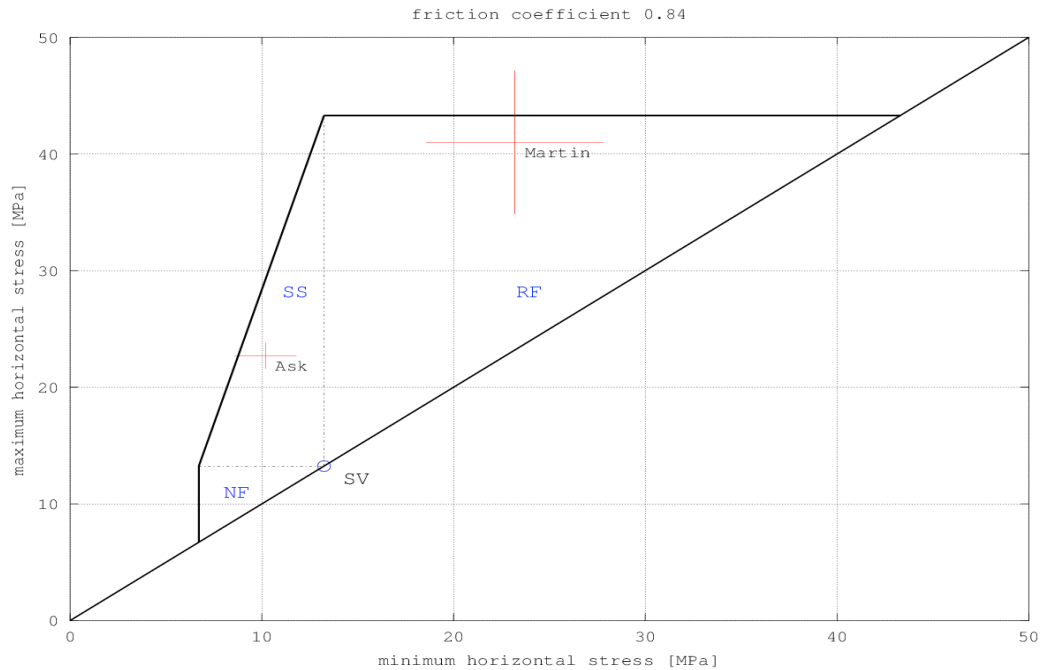


Figure 2.5: Stable stress fields regarding failure of intact rock with a frictional coefficient of $\mu=0.84$ at 500m depth. The stress models incl. their uncertainty (red cross) by SKB's "most likely" (Martin, 2007) and Ask et al. (2007) are shown in the stress space.

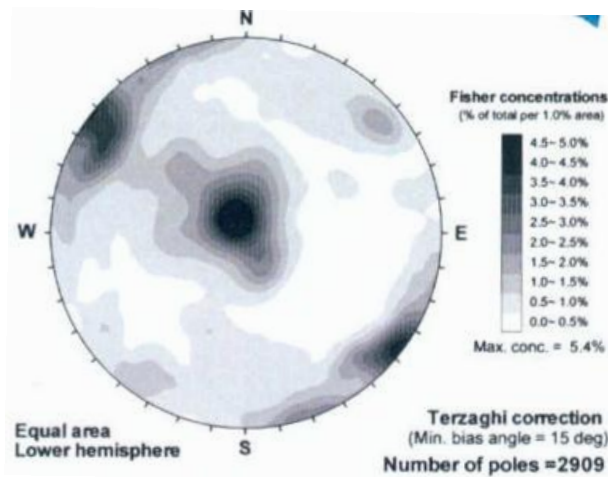


Figure 2.6: Equal area projection of poles to fracture planes inside the gently dipping deformation zones (from SKB TR-08-05, p.147, Figure 5-30).

2.3.2. Discussion of the validity of the existing stress models

The stress polygon in Figure 2.4 shows that SKB's "most likely" stress field lies mostly outside the range of allowable horizontal stresses (only touching the allowable range of stresses), if one considers the frictional strengths of existing discontinuities. This implies failure on any fracture that is preferably oriented

relative to principal stresses, i.e. where the ratio of shear stress to effective normal stresses acting on the fault is at its maximum. In this case those are planes that exhibit shallow dip in the direction of S_H .

SKB's stress model at Forsmark would exhibit instability under these assumptions. Gently dipping fracture zones are reported for the target volume, showing varying azimuth of dip direction (SKB TR-08-05; Figure 2.6). Especially fracture zones ZFMF1 and ZFMF2 intersecting repository depth exhibit fracture planes that would be prone to slip. Thus the high stress state would be unlikely to prevail although the stresses are supported by the intact rock model as evident from Figure 2.5. If therefore the stress model by Martin (2007) might be applicable to very sparsely fractured rock volumes may be discussed as fracture extension is not covered by the slip tendency approach.

The stress field by Ask et al. (2007) lies in the stable range of stresses and hence is possible as conclusion from this analysis. Supportive is also that the model is close to the margin of the stability area, which is an assumption of the approach.

In conclusion it may be stated that the results from fault reactivation analysis suggest that the stress field in accordance with a strike slip regime seems to be more likely.

It should be noted that the above considerations are valid if the assumptions about friction angle and cohesion are correct. There are reports of significant healing of fractures to an extent where they overcome the intact rock strength. This is evident from HTPF measurements at Forsmark where distinct breakdown event have been observed. If this is true for the discontinuities considered here, then the assumed coefficient of internal friction is larger and the ranges of possible stresses increase. However, the friction coefficients as reported by SKB was used.

2.3.3. Discussion of an alternative stress model

In the light of the above considerations an alternative stress model is suggested (Figure 2.7).

Vertical stress

The majority of the content of reviewed reports agrees about the fact that the vertical stress represents a principal stress which equals the theoretical stress calculated from the overburden weight. Significant deviations and negative magnitudes as yielded by some overcoring measurements are believed to indicate flawed measurements.

Accordingly the authors propose a vertical stress gradient that is lithostatic. A mean rock mass density of 2.700 kg/m^3 (SKB TR-10-52) yields $S_v = 0.0265 \cdot z$, where z denotes the depth in meters.

Minimum horizontal stress

The stress data that is considered valid below 300 m is the minimum horizontal stress as estimated from the hydraulic data only.

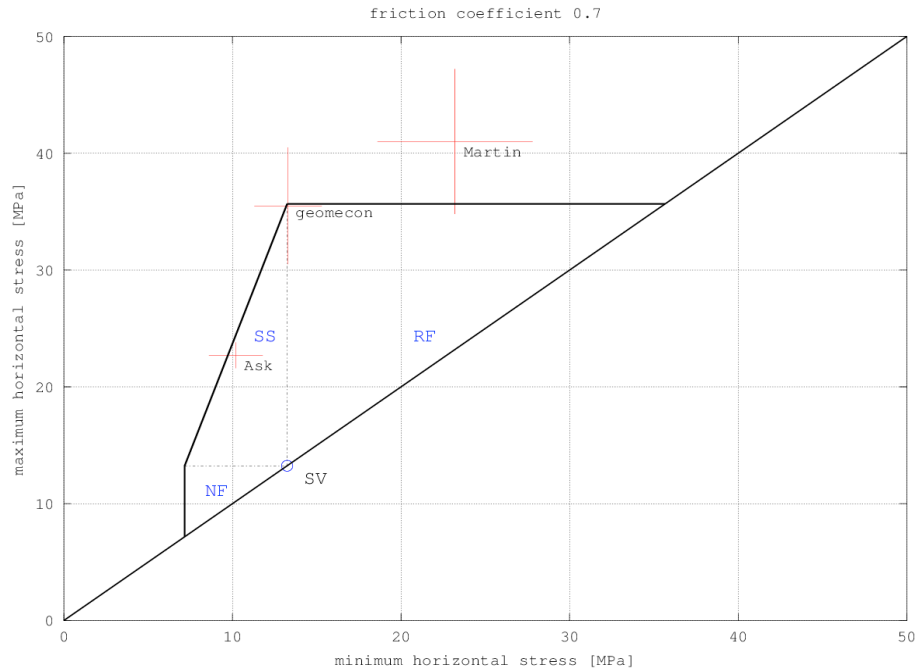


Figure 2.7: Stress polygon for allowable horizontal in situ stresses at 500m depth and with $\mu=0.7$ with the Geomecon stress model in the context of SKB's (Martin, 2007) and Ask et al.'s (2007) stress models.

Hydraulic measurements by Ask et al. (2007) indicate a reverse faulting regime at shallow depth, with convergence of S_h and S_v towards greater depth. Although the absolute stress magnitudes vary between the boreholes, the qualitative trend of converging S_h and S_v is visible in all boreholes. Inversion calculations on an earlier HF measurement campaign in boreholes KFM01A and KFM01B support this stress model, predicting a transition $S_v = S_h$ at repository depth (Klee and Rummel 2004). Regarding those lines of evidence it is likely that at 500m depth, the stress field is supporting both reverse and strike slip faulting. Therefore, the geomechanical stress model derived here suggests $S_h = S_v = 0.0265 \cdot z$ for a depth range constrained to the interval 400 m-600 m.

Maximum horizontal stress

The maximum horizontal stress is assumed to be a principal stress for sake of simplicity. It shows slight inclination from the horizontal for most measurements, generally dipping 5° to the south. At repository depth it should lie in the range of $23 \text{ MPa} \leq S_H \leq 35.5 \text{ MPa}$, bounded by the data from hydraulic tests (Ask et al. 2007, Klee and Rummel 2004) and the maximum allowed magnitude according to fault reactivation analysis (Figure 2.4). Following Jaeger et al. (2010), the authors assume that the crust is in frictional equilibrium and consider the maximum allowed stress of $S_H = 35.5 \text{ MPa}$. S_H from hydraulic measurements is suggested to be regarded as a lower limit (Sjöberg et al., 2004) and S_H derived from overcoring is suggested to be taken as upper limit (Martin 2007), at least for SKB's "most likely" model. Both apply to the suggested magnitude.

Orientation of the maximum horizontal stress

The direction of the maximum horizontal stress in SKB's "most likely" stress model is $145 \pm 15^\circ$ (SKB TR-08-05, Table 7-7); this is derived from the overcoring measurements only (Figure 2.1). Borehole breakouts, which can be assumed quite reliable indicators for stress orientation in unaltered and sparsely fractured rocks such as granites, suggest an orientation of S_H of 136° , while the hydraulic methods suggest $124 \pm 6^\circ$ (SKB R07-31, Table 6-2). The hydraulic indicated orientations lay outside the suggested variability of the overcoring data, just touching at 130° . Orientations interpreted from hydraulic measurements may be slightly biased if the borehole is not parallel to the least horizontal stress.

Taking into account all reported data the stress orientation could be interpreted like $139 \pm 21^\circ$, spanning from 118° to 160° . The mean direction of 139° is quite consistent with the breakout data.

However, as reported by several authors the measured azimuth of the maximum compression fits the expectations from analysis of far field stresses caused by plate motion and the regional pattern (Figure 2.8). The reported uncertainties for the different stress models appear to be quite optimistic, but have not been reviewed in great detail.

A variation of the stress tensor orientation by more than 40° , as suggested by the reported data, makes any analysis of spalling, fracture activation or similar quite complex, as the orientation of features within the stress field is strongly influencing rock failure.

Variability and uncertainty of the Geomecon's model

The Geomecon's model (also "gmc" in this report) is a re-interpretation of existing data and the uncertainty of the individual measurement is reflected by using or omitting the data only.

As can be seen from Figure 2.7 the Geomecon's model lies between Martin's (2007) and Ask et al.'s (2007) model. The lower end of the Geomecon's model variability extends the Ask model to higher stresses, but does not overlap with SKB's model. In terms of S_H the mean S_H of the Geomecon's lies within the variability of SKB's model, and vice versa, whereas the proposed range of Ask et al.'s S_H values lies well outside the Geomecon's model range.

The influence of the friction coefficient on the analysis (c.f. Figures 2.4 and 2.5) has been reflected in the Geomecon's model by allowing the S_H variability to span outside the stability polygon.

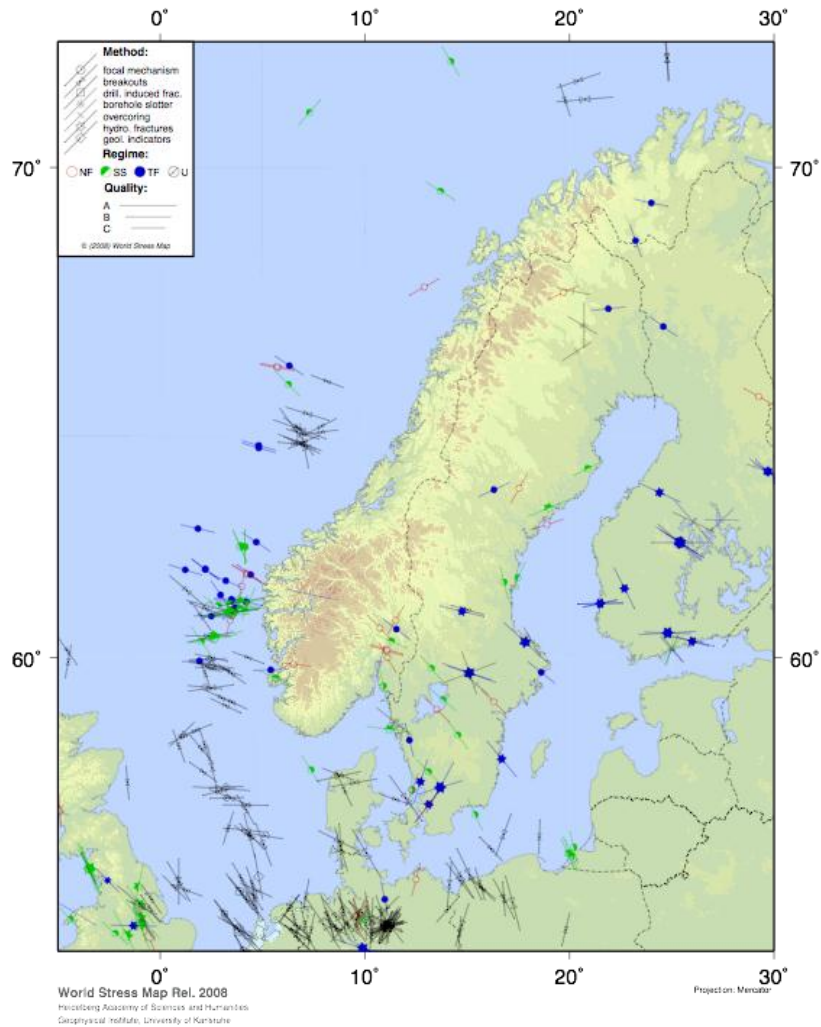


Figure 2.8: Stress data from the World Stress Map Project for Scandinavia (Heidbach et al., 2008).

Summary

The majority of stress models suggest a trend from thrust faulting at shallow depth to strike slip faulting at depth, with the transition being within the upper 1,000m of the Earth's crust. Large scale models (Stephansson, 1991) and models from close-by sites (Finnsjön, Central Sweden) support this concept.

The newly proposed model derived in this study therefore is in good agreement with the previous assessments of the stress field at Forsmark (c.f. Figure 2.9). Klee and Rummel (2004) as well as Sjöberg et al. (2005) also suggest $S_v = S_h$ in their analysis of the stress field at Forsmark. The analysis of Lindfors et al. (2005) of the overcoring data from borehole KFM01B results in similar values to the stress model derived above for the second measurement level (down to 455 m depth), although those measurements should be regarded with some skepticism, as discussed in

section 2.1.1. The maximum horizontal stress in Lindfors et al. (2005) is a few MPa larger compared to the proposed model, and lies around 40 MPa.

Data from the Olkiluoto site in Finland that has been revised by Sjöberg et al. (2005) show slightly lower values for S_H at repository depth (SKB R-05-35, Appendix J).

2.4. The Consultants' assessment on the stress models

The stress model by SKB (called “most likely”) used for most the analyses, appears unlikely from a geomechanical point of view. Under the conditions of the “most likely” stress model failure of the rock mass would have to be expected, which is not the case. Further, the data used for the modeling was selected without a reproducible rational.

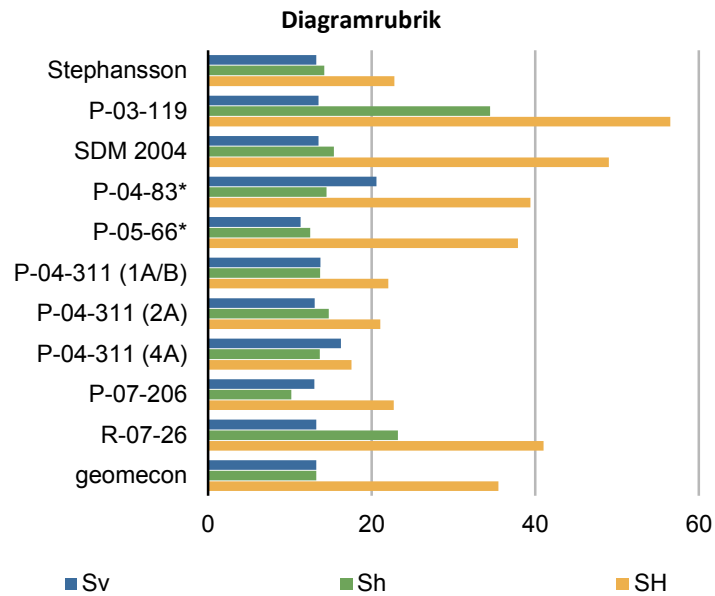


Figure 2.9: Summary of available stress field estimations for repository depth of 500 m. With exception of Stephansson (1991), they have been done for the Forsmark tectonic lens. *established for the 400m to 455m depth interval.

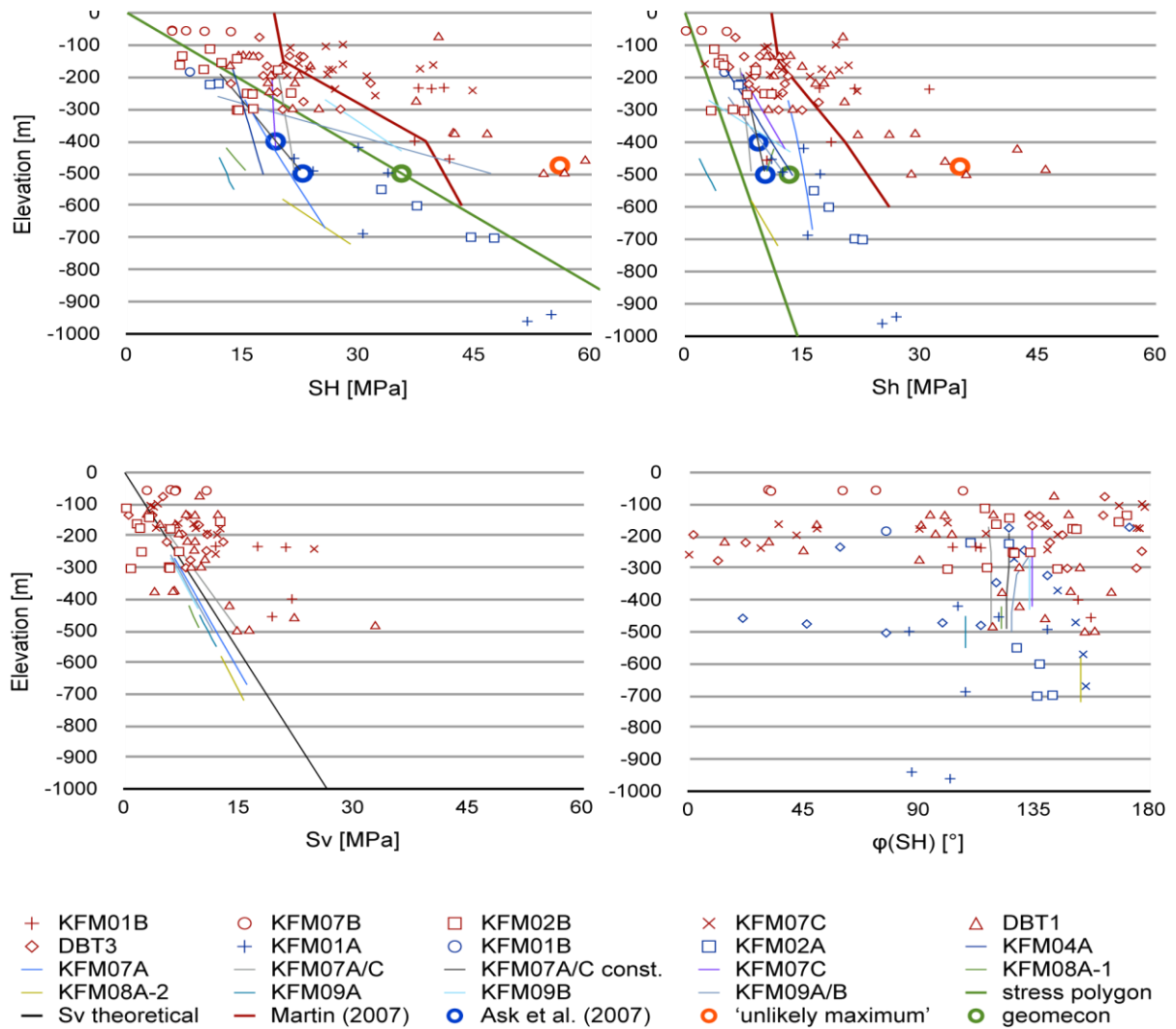


Figure 2.10: All data points derived from stress measurements for the maximum horizontal stress (S_H), the minimum horizontal stress (S_h), the vertical stress (S_v) and for the orientation of the maximum horizontal stress ($\phi(S_H)$). HF/HTPF tests that yield stress gradients from inversion analysis are shown as straight lines. For constrained solutions with fixed azimuth of S_H the orientation is not shown in the diagram. All data points shown are listed in Table A.1. Errors and confidence intervals are not shown; most of the data is associated with large uncertainties (see text).

However, the number of reliable data points at repository depth is insufficient to draw any final conclusions; this is also true, if all data that was not ranked as low confidence were used (Figure 2.10).

Although it is stated by SKB, that no additional stress measurements will be conducted from surface boreholes and the issue about the stress field has to be solved by measurements during construction (SKB TR-08-05), it would be beneficial to perform additional stress measurements at the depth interval of interest for the repository location. The stress field assumptions have major impact on all analyses of repository integrity and long-term safety. If additional stress

measurements have to be performed from the surface, a proper judgment of the risks, like introducing potential fluid pathways, is needed.

2.5. Stress models for further analysis

For further analysis of spalling in the context of this assessment, the authors will use an additional model called Geomecon's stress model in addition to the existing models by SKB. The orientation of S_H is assumed to be 145° as suggested by SKB.

The temporal variations of the stress field are accounted for by considering possible scenarios affecting the repository like effects of temperature due to heat generation of the spent fuel and increased overburden load during a glaciation cycle and related increase of pore pressure.

Likely spatial variations are presented as they are suggested by the stress measurements results (Table 2.2).

Table 2.2: Stress magnitudes at repository level for the three models considered in further analysis.

S_H [MPa]	S_n [MPa]	S_v [MPa]	PP [MPa]	Reference
41.0 ± 6.2	23.2 ± 4.6	13.3 ± 0.3	5	Martin (2007, SKB R-07-26)
22.7 ± 1.1	10.2 ± 1.6	13.3	5	Ask et al. (2007, SKB P-07-206)
56 ± 6	35 ± 15	13.3 ± 0.3	5	SKB's "unlikely maximum"
35.5 ± 5	13.3 ± 2	13.3	5	Geomecon (gmc)

3. Analytical analysis of spalling

The potential for spalling was analysed by SKB by means of various approaches. They used both analytical approaches as well as numerical simulations. In this section we, analyse the potential for spalling for selected stress field scenarios and related evolution scenarios due to thermal loading and glaciation. The stress evolution during thermal and glaciation phases are taken from SKB's analyses.

The scoping calculations in this assessment are purely analytical. Therefore, the local stress state at the excavation wall due to stress redistribution in the presence of an excavation is calculated analytically by means of the Kirsch-solution (c.f. Jaeger et al 2007). The resulting tangential stress is compared to common rock failure criteria. Whereas SKB confined their analysis to compressive failure, in extension to SKB's reported analysis, the tensile failure potential is also analysed by the authors.

The results in principle confirm SKB's judgement that spalling cannot be ruled out at certain stages during the history of the repository, both for deposition tunnels and holes.

3.1. SKB's understanding of the potential of spalling

Stress induced spalling is expected by SKB to be one of the major modes of instability of underground openings, as inferred from comparison with similar constructions in Scandinavian rocks. This is especially the case as the frequency of fractures is low at repository depth and the ability for wedge failure will be low (SKB R-08-116).

3.1.1. Spalling strength

According to SKB, spalling occurs when the tangential stress at the deposition hole wall exceeds the crack initiation stress (CIS) under unconfined loading as exhibited in laboratory testing. These may be given either directly as a parameter or as ratios of unconfined compressive strength UCS.

The reported values of UCS, CIS and CIS/UCS vary throughout the different reports. In SR Site (SKB TR-11-01) no specific value but reference to several reports are given, where additional references to additional reports or cross-reference to already mentioned reports are given. In the following the different values and the ratio found in the references are summarised.

The Site Descriptive Model for Forsmark (SKB TR-08-05) provides a mean uniaxial compressive strength of 226 MPa and a mean crack initiation stress of 116 MPa (SKB TR-08-05, Table 7-3). The reported ratio CIS/UCS is 0.51. Martin (2005) gives a mean uniaxial compressive strength of 225 MPa and a crack initiation stress of 119 MPa (SKB R-05-71, Fig. 4-3), which corresponds to CIS/UCS of 0.52. In SKB (R-05-18, p. 512) a CIS/UCS of about 0.53 is given.

Hökmark et al. (2010, SKB TR-10-23, p.30, p. 149, p. 275) assume that the spalling strength is in the range of 0.52-0.62 of the uniaxial compressive strength of intact rock. On page 164 of SKB (TR-10-23) the authors refer to a spalling strength of 0.57, which corresponds to the value predicted by Martin (2005) for crystalline

rocks, based on the Äspö Pillar Experiment. Eriksson et al. (2009, SKB R-08-115, Table 4-4) mention a mean crack initiation ratio of 0.53 based on SKB R-08-83. However, a crack initiation ratio of 0.53 could not be found in the referenced report. SKB (R-08-116, p.121) mention a CIS/UCS range of 0.41 to 0.64 with a mean CIS/UCS ratio of 0.53. The ratios are based on 116 not further specified laboratory measurements. Finally Martin (2005, Table A-1) also mentions an in situ ratio of 0.65.

In general it can be summarized that the criterion of SKB to define spalling might be in the range 0.51 to 0.65.

However, the range of individual strength values is not represented by the given ratios. The CIS/UCS ratio only represents the average of both parameters. The individual ratios of CIS/UCS range from 0.41 to 0.64 (SKB R-08-116). The lowest measured crack initiation strength for the dominant rock type (101057) is 60 MPa (SKB TR-08-05, p.218).

The 57 laboratory uniaxial compression experiments stated by Martin (SKB R-05-71) are used to exemplarily and schematically visualize the variability of the data (see Figure 3.1).

In the Äspö Pillar Stability Experiment (APSE, Andersson, 2007) the rock failure process in response to drilling induced and thermally induced stresses was examined and the spalling strength was generally found to be higher, around 0.59 of the mean UCS. Also, the large scale experiment revealed that the propagation of yielding is very sensitive to changes in tangential stress but does not propagate with time when tangential stress is held constant. Another observation was that spalling potentially can be prevented by application of a small support pressure to the wall of the hole.

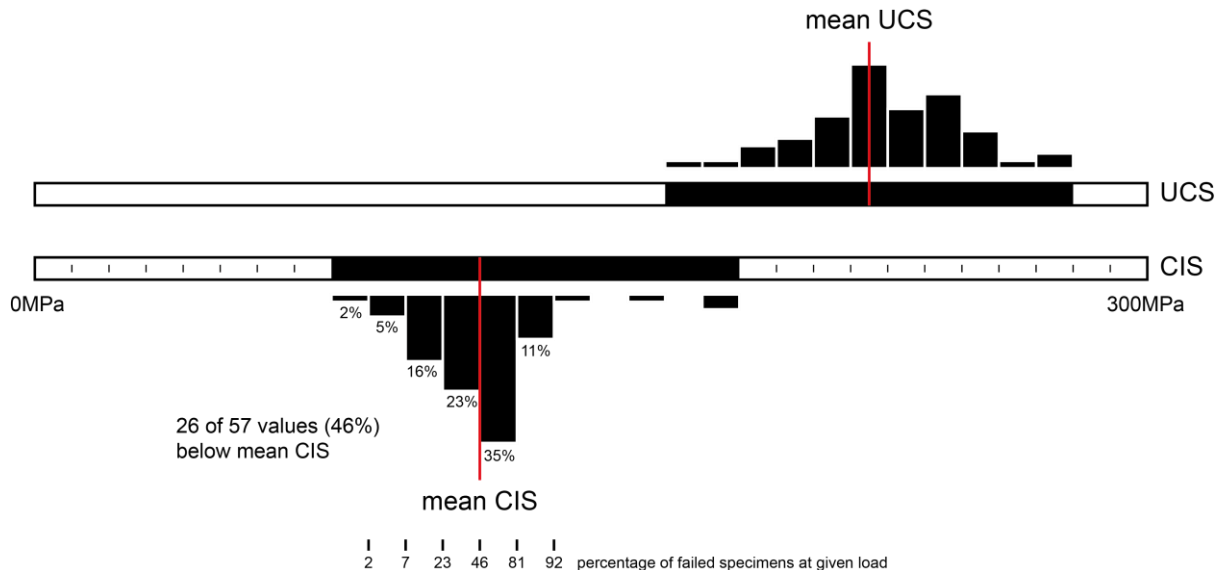


Figure 3.1: Graphical representation of the variability and range of unconfined compressive strength UCS and crack initiation stress CIS with their respective mean values as given by Martin (2005, SKB R-05-71). The data set contains 57 experiments. The mean UCS is 225 MPa and the mean CIS is 119 MPa, i.e. CIS/UCS = 0.52. About 46% of the experiments do not fall within the stated spalling criterion; i.e. samples fail at stress lower than the criterion.

It becomes clear that using the average ratio of CIS/UCS to determine the spalling may suggest more stable conditions than can be expected. The defined spalling criterion ignores the lower part of the distribution, i.e. about 46%, of the CIS range.

A further study on spalling prevention by means of counterforce suggests that confining pressures of the borehole, in this case applied by dry light expanded clay pellets, can reduce spalling in a deposition hole (SKB TR-10-37). However, as the results indicate that the scale for this experiment was too small to be representative, the results have to be treated with care. It is suggested to carry out full scale tests. Further, in the application during emplacement at the repository, the gap between the bentonite and excavation wall might not be fully filled in all cases.

3.1.2. Spalling occurrence

The risk of spalling generally increases with depth simply because the absolute stress magnitudes increase with increasing overburden. The depth where spalling becomes a critical issue depends on the site's specific stress gradients.

In general, at the repository depth at Forsmark, spalling is not considered to be an issue for the vertical deposition holes before emplacement of canisters. The same is valid for the deposition tunnels if they are oriented sub-parallel to the direction of the maximum horizontal stress S_H . For deposition tunnels oriented perpendicular to S_H , the risk of spalling will increase significantly below a depth of 450m (SKB R-05-71).

Assuming an average spalling strength of 55% of mean UCS, Fälth and Hökmark (SKB R-06-89) concluded that it is unlikely that spalling will occur in Forsmark area during the operational phase, but will be induced at a later stage due to the thermal loading.

A two-dimensional analysis of stress redistribution with the assumption of SKB's "most-likely" stress field resulted in maximum tangential stress of 75-102 MPa, which is below the reported spalling strength of 114 MPa, but well into the range of reported CIS (see Figure 3.1). A three dimensional stress analysis of the tangential stress on the deposition hole walls after excavation of the deposition tunnels for different orientations of the stress field gave stable conditions, i.e. no spalling for orientations of the deposition tunnels within 30° with respect to the S_H direction (SKB R-08-116).

It has been shown that the fraction of deposition holes that exceed an acceptable 5 cm-limit of spalling depth is approximately 100-200 out of 6,000 in total for the "most-likely" stress field (SKB R-08-116). In this analysis SKB uses the probabilistic methodology outlined in Martin and Christiansson (2009), which is based on the 2D plane strain Kirsch solution for the stresses.

During thermal heating as well as future glaciations spalling is expected to develop. This is outlined in SKB's THM report (SKB TR-10-23) and further discussed in chapter 4.1. However, whereas the thermal phase appears to be quite well constrained, the glaciation period is realized in about a dozen scenarios, indicating the uncertainty of the model.

3.2. Motivation of the Consultants' assessment

The information on stress fields, stress field alterations, strength criteria, absolute strength etc. vary throughout the reports and this makes it very complex to follow the spalling studies by SKB.

In particular the main body of discussion by SKB suggests that, if the tangential stress on any excavation wall is below 53% of UCS, no spalling will occur. However, the 0.53 times UCS criterion is a combination of an averaged UCS and an averaged crack initiation strength CIS, making it impossible to assess the margins (probability) to failure directly (refer to Figure 3.1). In addition, spalling strengths, i.e. crack initiation strengths, as low as 60 MPa have been measured in laboratory experiments, which makes it worth to discuss the spalling potential based on this strength criterion.

Recently published data (Ghazvinian et al., 2012) suggest that SKB's analyses might overestimate the CIS by as much as 20%.

Further, as the applied stress field model is subject of discussion, it is hardly possible to judge on the probability of failure and the implications of variations of the assumed stress or strength models for the Forsmark area.

Therefore, the authors have developed a method that combines the acting stress field information with the tangential stress magnitude under given conditions. With this methodology it is easy to judge if spalling is to be expected and how that is affected by a change of stress affects. Furthermore, in addition to the thermal phase, they analysed a variety of glaciation scenarios to account for the uncertainties in predicting the stress evolution.

The spalling criterion itself, the authors assume appropriate in the light of the available data base. The approach to determine the spalling potential by comparing the acting stress state at the wall of an excavation and a compressive strength is state of the art in engineering practice (e.g. Zoback et al., 1985).

3.3. Calculation of spalling potential

The analysis of spalling confines itself to analytical scoping calculations of the influence of in situ stress at certain stages during the stress evolution of a repository. The analyses hold for circular openings in a homogeneous medium only. Any influence of stress redistributions due to other excavations are not considered, i.e. the influence of a deposition tunnel on the deposition hole or vice versa is not considered. Therefore, the following analyses will not correctly estimate the risk of spalling for the uppermost section of the deposition holes where the stress redistribution of the deposition tunnels alter the local stress field and give stress concentrations.

3.3.1. Methodology

Diagram are created (schematically in Figure 3.2) spanning the S_1 vs. S_3 space for a given orientation of the excavation. The condition $S_1 = S_3$ is the lower bound, as conditions below this line cannot be fulfilled by definition of principal stress. The tangential stress acting on the circular excavations is plotted as color-coded isolines

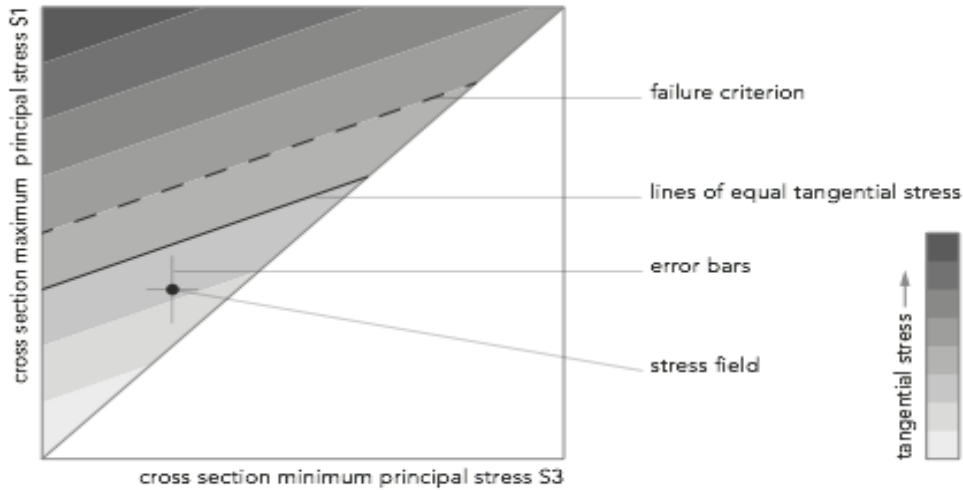


Figure 3.2: Example of spalling analysis. The diagram shows the maximum tangential stresses around circular openings depending on the principal stresses. Failure criteria correspond to contour lines of equal tangential stress. Stress conditions can easily be shown and evaluated with their tangential stress relative to spalling criteria in order to evaluate the spalling potential.

into the S_1 vs. S_3 plane. Any spalling criterion can be plotted into the diagram as a dashed contour line also. Into this diagram the in situ stress estimate at examination level (-500m) is plotted together with error bars corresponding to the error in the stress field estimates.

For estimation of spalling around deposition holes and tunnels the tangential stress extreme values may be calculated based on linear elastic material behavior by (see e.g. Zoback et al., 2007, p.174):

$$\sigma_{\theta\theta\max} = 3S_a - S_b - 2P_p - \Delta P \quad \text{Eq. (3.1)}$$

$$\sigma_{\theta\theta\min} = 3S_b - S_a - 2P_p - \Delta P \quad \text{Eq. (3.2)}$$

where S_a is the maximum principal stress in the plane of the circular opening, S_b is the minimum principal stress and ΔP is the difference between the counter pressure acting on the deposition wall and the pore pressure P_p .

For vertical deposition holes, S_a and S_b correspond to the maximum S_H and minimum S_h horizontal stress, respectively; for deposition tunnels the input stresses to the analysis depend on the orientation of the tunnel axis and the relative magnitudes of the stresses.

Also simple analytical operations to reflect changes in stresses may be performed in the diagrams. Changes in the stress tensor can be performed by drawing its path.

3.3.2. Employed failure criteria

Compressive failure

The spalling criteria applied to the data are

- maximum tangential stress $> 0.53 \text{ UCS} = 0.53 \cdot 225 \text{ MPa} = 119 \text{ MPa}$. This is taken as representative for SKB's criterion for spalling. However, to reflect the various experimental values one would have to draw a set of lines. Refer to the respective section on spalling strength in the presentation of SKB's understanding of spalling.
- in case swelling pressures are considered, the Mohr-Coulomb failure criterion in the form of $S1 = S3((\mu^2 + 1)^{0.5} + \mu)^2 + \text{CIS}$ with a CIS (crack initiation stress) of 100 MPa and $\mu = 0.84$ is used. If no swelling pressure occurs, it reduces to
- maximum tangential stress $> 100 \text{ MPa}$. This average crack initiation stress was determined by acoustic emission activity analysis in studies at CANMED and Posiva and is lower than the data reported by SKB (Ghazvinian et al., 2012).
- maximum tangential stress $> 60 \text{ MPa}$. The crack initiation stress is stated for FFM01 in RFM029 (SKB TR-08-05, Table 7-3, p218) to range from 60 to 187 MPa. The lower value is taken as conservative failure criterion. CANMED and Posiva report lowest values of about 75 MPa for CIS (Ghazvinian et al., 2012), hence the 60 MPa threshold may be viewed as the absolute minimum.
- maximum tangential stress $> 157 \text{ MPa}$; UCS is stated for FFM01 in RFM029 (SKB TR-08-05, Table 7-3, p218) to range from 157 to 289 MPa. The lower value is taken as conservative reference criterion.
- as an alternative spalling indicator, the von Mises criterion was used. The originally three dimensional criterion was chosen, as it is easy to apply and the input can be tuned to the values of UCS as reported by SKB. The criterion is $C^2 = (S1 - S2)^2 + (S1 - S3)^2 + (S2 - S3)^2$; C may be determined by assuming the CIS data¹, i.e. $C = \sqrt{2} \text{ CIS}$.

These criteria are plotted as dashed lines into the spalling potential diagrams. Whereas SKB promotes the 0.53 UCS criterion with the respective deviations, the authors add to the analysis recent published data on the CIS, the lowest reported unconfined crack initiation stress (SKB TR-08-05), and the lowest reported unconfined compression strength. As an alternative model for failure, the authors applied the von Mises criterion and a Mohr-Coulomb criterion, which is adjusted to fit the new CIS criterion by Ghazvinian et al (2012).

¹ In unconfined conditions $\text{UCS}^2 = C^2 = S1^2 + S1^2 = 2(S1)^2$.

Ghazvinian et al. (2012) show a comparison of several data sets on the Småland granodiorite to determined CIS and UCS. The studies were performed at the laboratories of SKB, CANMED and Posiva. SKB reports CIS as determined by strain measurements on unconfined compression tests larger than 100 MPa with a large span of UCS ($\Delta\text{UCS} = 110 \text{ MPa}$), whereas both Posiva and CANMED measured CIS as low as 75 MPa by means of acoustic emission recording and smaller ranges for UCS ($\Delta\text{UCS} = 50 \text{ MPa}$ and $\Delta\text{UCS} = 30 \text{ MPa}$ respectively).

With the application of the lowest reported crack initiation level, the authors introduce a criterion, which applies the lower limit of the SKB spalling criterion to increase the robustness for the occurrence of spalling, i.e. if the stress data plots below the limit, spalling due to SKB's criterion is unlikely. In return, if the stress data plots above the line, at certain locations spalling of deposition holes is possible.

The rationale for including the lowest reported UCS to the analysis is to have a measure for the severeness of the spalling. If the data point plots above that limit, excessive spalling is likely.

The spalling criterion proposed by SKB has been shown to be valid both in Canada and Forsmark for granitic rocks, and is also frequently used in borehole stability analyses in deep wellbore drilling in various lithologies; hence it is not further questioned here.

By using additional criteria that are not based on the assumption that spalling occurs if the tangential stress on the excavation wall exceeds a compressive loading level. Assuming any wall support like swelling that is propagated further into a biaxial loading criterion like Mohr-Coulomb would make the analysis less conservative as spalling would be reduced. Further, there is evidence from SKB judgment that the bentonite swelling may be active at very late stages after repository closure.

Tensile failure

The tensile strength criterion is calculated for the sake of completeness of analysis to also be able to give an indication about the tensile fracturing potential

- minimum tangential stress < tensile strength = 10 MPa (SKB TR-08-05).

3.3.3. Stress evolution model

In the analytical calculation of the spalling potential, the stresses are altered due to the thermal heating and the subsequent glacial loading. For the scoping calculations in this assessment, the authors consider some cases as outlined in Table 3.1. In principle any change of in situ stress, i.e. S_H , S_h and S_V , can be directly derived from the diagrams without further calculation. Only the hydraulic pressures change the strength envelopes plotted.

The in situ stress data used for the analysis are given in Table 3.1. These stress fields serve as starting points for the analyses (cf. Table 3.2 model scenario #1).

Table 3.1: Stress magnitudes at repository level for the three models considered in further analysis.

S_H	S_h	S_V	P_P	Reference
[MPa]	[MPa]	[MPa]	[MPa]	
41.0 ± 6.2	23.2 ± 4.6	13.3 ± 0.3	5	SKB's "most likely" Martin (2007, SKB R-07-26)
56 ± 6	35 ± 15	13.3 ± 0.3	5	SKB unlikely maximum (SKB R-08-116)
22.7 ± 1.1	10.2 ± 1.6	13.3	5	Ask et al. 2007 (SKB P-07-206)
35.5 ± 5.0	13.3 ± 2.0	13.3	5	Geomecon (see also Chapter 2 in this report)

Table 3.2: Stress evolution scenarios as considered in further analysis. The stresses for the initial starter model are given in the respective table. The data for scenarios #6 to #11 and #14 and #15 were taken from Lund et al. (2009, SKB TR-09-15, figure 7-17).

Scenario	#1	#2	#3	#4	#5
	starting point	thermal phase	ice cover without hydraulic connection and no swelling pressure	ice cover with hydraulic connection and without swelling pressure	ice cover without hydraulic connection and with swelling pressure
	[MPa]	[MPa]	[MPa]	[MPa]	[MPa]
S _H	see stress models	+27	+30	+30	+30
S _h		+23	+30	+30	+30
S _V		+3	+30	+30	+30
P _P	5	+0	+0	+30	+0
P _S	0	+0	+0	+0	+5
Scenario	#6	#7	#8	#9	#10
	Lund M1	Lund M2	Lund MT8	Lund M3	Lund MT10
	[MPa]	[MPa]	[MPa]	[MPa]	[MPa]
S _H	+53	+38	+22	+20	+20
S _h	+38	+28	+20	+18	+19
S _V	+25	+26	+26	+28	+27
P _P	+5	+5	+5	+5	+5
P _S	+0	+0	+0	+0	+0
Scenario	#11	#12	#13	#14	#15
	Lund MT12	ice retreat #1	ice retreat #2	Lund MT9	Lund MT7
	[MPa]	[MPa]	[MPa]	[MPa]	[MPa]
S _H	+27	+0	+0	+29	+22
S _h	+25	+0	+0	+27	+21
S _V	+26	+0	+0	+28	+27
P _P	+5	+30	+30	+5	+5
P _S	+0	+0	+5	+0	+0

The thermal evolution of the repository was simulated by Hökmark et al. (2010, SKB TR-10-23). In their analyses the maximum temperature increase at the deposition hole wall was $\Delta T = 48\text{K}$. This resulted in an increase of the in situ stress components S_H , S_h and S_V of about +27 MPa, +23 MPa and +3 MPa (SKB TR-10-23, Figure. 6-6) (cf. model scenario #2).

The maximum glaciation induced stress increase according to SKB is almost hydrostatic +30 MPa (SKB TR-10-23, Figure 4-12) (cf. model scenario #3). The changes in differential stress is about 5 MPa for the base model, which is ignored here as it lies within the initial stress error.

Assuming there is a hydraulic connection with the repository, the fluid pressure during glaciation would increase by roughly 30 MPa (cf. model scenario #4). The effect of a saturated bentonite swelling pressure is modelled in scenario #5 without accounting for influence of the radial stress on the rock strength model.

However, in addition to the ice sheet model above, Lund et al. (2009; SKB TR-09-15) modelled a variety of different stress responses due to the ice sheet cover depending on the crustal thickness and other factors. This clearly shows the uncertainty in the stress evolution scenario. To at least cover the variety of maximum changes in stress state that were simulated for Forsmark area, additional analyses are performed (cf. model scenarios #6 to #11 and #14 and #15).

Scenarios #12 and #13 represent models in which the ice cover is retreated, but the increased fluid pressure is trapped within the repository. Although quite academic as reduction of the pressure head from surface along with a reduction of S_V will reduce the pore pressure at depth over the deglaciation times, this scenario is shown to have the potential for tensile fracturing.

3.3.4. Results of the analytical spalling analysis

The results from the analyses presented in the previous section are outlined below.

In general the scoping calculations clearly show that in case of SKB's "most likely" stress field model, spalling will occur under certain conditions already at the excavation stage of the deposition holes, if the strength of the rock is locally lower than the average spalling value. During the thermal and glaciation phase extensive spalling is to be expected with the assumed model for spalling.

Deposition holes - spalling potential during excavation

For the stress conditions at excavation (Figure 3.3) the stress models by Martin (2007) and Geomecon plot below the spalling criterion defined by SKB, i.e. $0.53 \cdot \text{UCS}$, the CIS criterion according to the levels reported by Ghazvinian et al. (2012) and the von Mises criterion. However, both stress field models plot above the lowest reported crack initiation stress; hence spalling might be experienced at low rock strength conditions.

The Geomecon model plots in terms of tangential stress about 10 MPa below the CIS criterion and 30 MPa below the $0.53 \cdot \text{UCS}$ criterion. More specifically the tangential stress at the deposition wall is about 88 MPa, whereas the lowest reported CIS is 85 MPa (Martin 2005), in contrast to 60 MPa in SKB TR-08-05 and SKB R-07-31. This means that spalling will be exhibited during excavation on a fraction of the deposition holes. Based on the data by Martin (2005) this suggests that about

1/57, i.e. 2% of the specimens would have failed under the Geomecon stress model conditions, which may be interpreted that 2% of the deposition holes (120 out of 6000) would spall².

The maximum depth of spalling according to Diedrich (2007) can be estimated by:

$$r/R = 0.5 (TS/SC + 1) \quad \text{Eq. (3.3)}$$

where r - R is the depth of spalling, R is the excavation diameter, TS is the maximum tangential stress, and SC is the spalling criterion. Hence, in our case r/R is $0.5 \times (88/85+1) = 1.02$. So the maximum depth of spalling for the deposition holes would be about 3-4 cm.

Similarly SKB's stress model (Martin 2007) plots about 25 MPa below the 0.53 UCS spalling criterion; following the same rational as above this corresponds to 5% of spalled deposition holes (300 out of 6000). The maximum tangential stress at the deposition hole wall is 95 MPa, i.e. 10 MPa above the smallest CIS reported by Martin (2005). This would lead to a maximum spalling depth of about 11 cm ($r/R = 1.06$). Out of the 300 deposition holes that experience spalling, about 120 would exhibit a spalling depth deeper than 5cm.

At conditions defined by the stress model by Ask et al. (2007) no spalling would be exhibited with the assumed spalling models during the excavation phase, even with assuming the lowest measured CIS. SKB's "unlikely maximum" stress model exceeds the 0.53·UCS criterion by 10 MPa, hence would exhibit spalling in 41/57, i.e. 81%, based on the data reported by Martin (2005).

² However, if the full strength data were available, the percentages could be different.

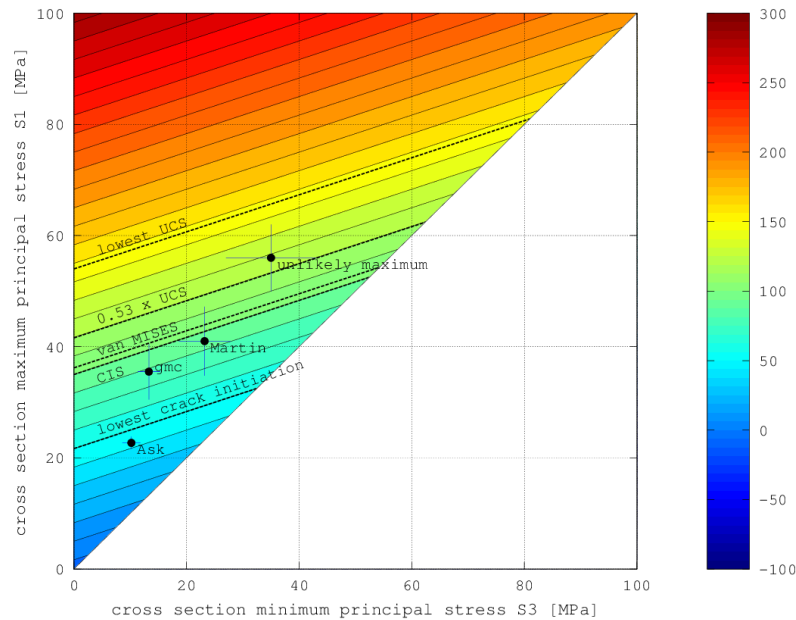


Figure 3.3: Spalling potential diagram for deposition holes for the excavation phase (model scenario #1). The colour code depicts tangential stress in [MPa], the colour code shows 10 MPa classes. See text for discussion.

Deposition holes - spalling potential during thermal phase

During the thermal phase, due to the increase in horizontal stresses, the tangential stresses at the deposition holes are increased by about 50 MPa (Figure 3.4). The stress field models by Martin and Geomecon plot above 0.53 UCS, indicating severe spalling. SKB’s “unlikely maximum” model even plots above the lowest reported UCS, hence indicating massive spalling. In response to the model by Ask et al. (2007) the tangential stresses stay below the 0.53 UCS threshold, but above the lowest crack initiation strength.

Geomecon’s stress model plots 25 MPa and SKB’s “most likely” stress model about 30 MPa above the 0.53 UCS criterion. This means that about 90% of the deposition holes, would be exhibiting spalling (c.f. Figure 3.1).

The maximum spalling depth is expected to be like 60 cm (see Diedrich 2007). More than 80% of the deposition holes would be subjected to spalling larger 5 cm.

A swelling pressure would deliver about 5 MPa of support pressure, this might lead to a reduction of spalling. Diedrich (2007) stated that a swelling pressure would increase the spalling criterion by an amount equivalent to the swelling pressure itself ($SC = 0.5 UCS + Sw$; where Sw is the swelling pressure), hence the mean CIS would be increased by about 5 MPa. This reduces the number of failed deposition holes by a few percent, but still the majority of deposition hole walls would be subject to failure during the thermal phase.

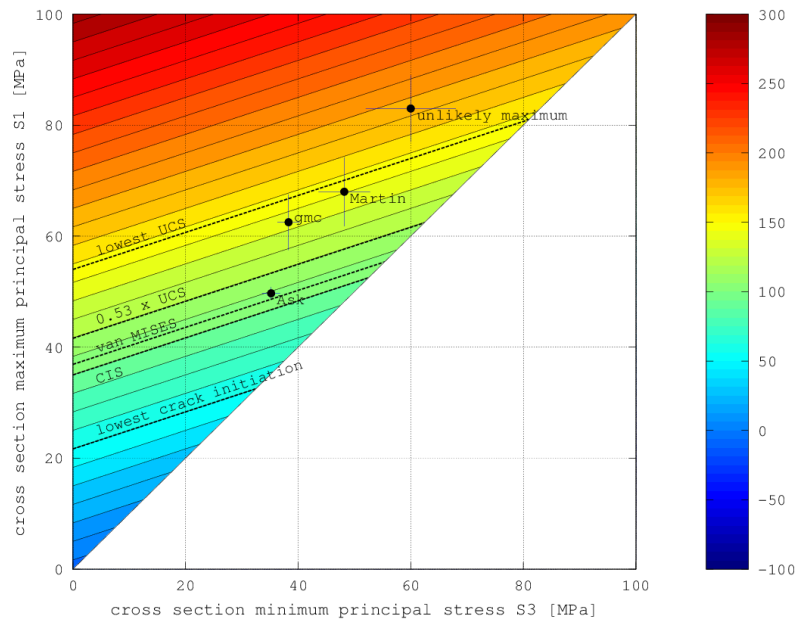


Figure 3.4: Spalling potential diagram for deposition holes at thermal phase (model scenario #2). The colour code depicts tangential stress in [MPa]. See text for discussion.

Assuming that the thermally introduced stresses are relieved at start of glaciation, the principal stresses due to the ice cover increase isotropically. In case permafrost prevents any hydraulic pressure communication with repository level (Figure 3.5), the tangential stress increase at the deposition hole walls is about the same as during the thermal phase. Adding a hydraulic connection during glaciation (Figure 3.6) or a swelling pressure from the saturated bentonite together with hydraulic connection (Figure 3.7) reduces the tangential stress response such that with the Martin (2007) and Geomecon proposed stress fields the points fall on the 0.53 UCS criterion, whereas the Ask et al. (2007) model predicts more stable conditions.

The results from analysis of the other model scenarios for glaciation can be found in Figures A2.2 - A2.10 in Appendix 2; Table 3.3 summarizes the outcome together with the analysis for the deposition holes in the first five scenarios.

Deposition holes - tensile failure potential

In most of the scenarios the minimum stress is compressive, hence no tensile failure is to be expected at the deposition holes (Table 3.3 and see Appendix 2, Figures A2.26 - A2.40, for the respective tensile failure potential plots).

However, there are certain scenarios which need to be considered due to the risk of tensile failure. Firstly with the Geomecon's stress model during the excavation phase the tangential stress might become tensile (negative) at the deposition hole wall, hence the transmissivity of existing fractures might be increased as they are opened.

Secondly, if after a glaciation with increased fluid pressure at repository level (+30 MPa), the ice cover is removed but the fluid is trapped for some period due to permafrost, local hydraulic fracturing may appear as it can be seen in Figure 3.8. The implications of such tensile fracturing need to be examined, as the trapped pore pressure is potentially higher than some of the in situ stresses. However, if there is a hydraulic contact between the top of the ice to the repository during the complete time of ice melting it is unlikely that such high pressure can remain till the ice is gone. This scenario is rather academic but shows that the issue needs some extra treatment. In this case, stress models with low stress magnitudes are less conservative.

Deposition tunnels - spalling potential

The authors have confined the analysis of spalling in the deposition tunnels of circular shape to the case that the tunnel axis is parallel with S_H . An orientation perpendicular to S_H could result in more pronounced spalling depending on the initial stress field regime.

The potential for spalling in the deposition tunnels is in general smaller than for the deposition holes (Table 3.4).

In the analyses with stress fields by Ask et al. (2007) and Geomecon show no case where the tangential stress exceeds SKB's 0.53 UCS criterion for the deposition tunnels. With the SKB's "most likely" stress model it plots above the 0.53 UCS criterion during the thermal phase and during one of the glaciation scenarios by Lund (SKB TR-09-15).

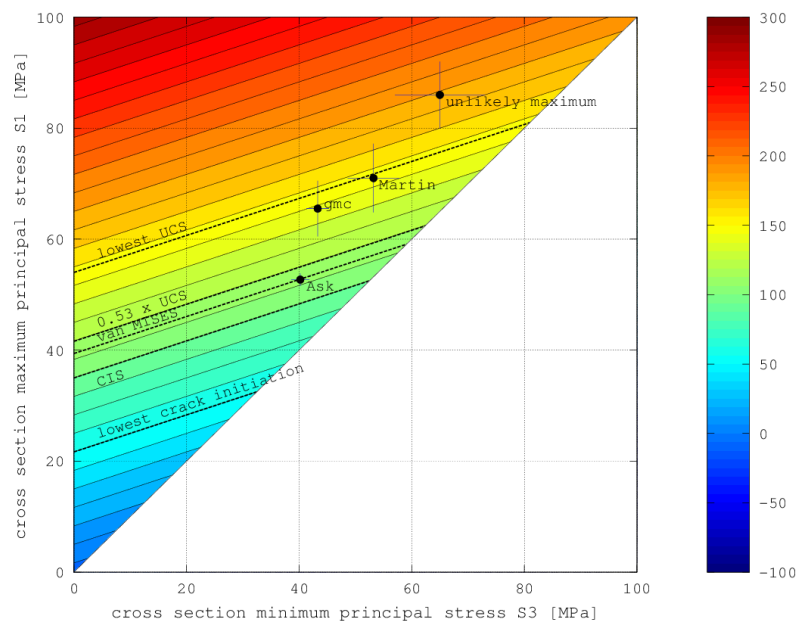


Figure 3.5: Spalling potential diagram for deposition holes during glaciation with no hydraulic connection and no bentonite swelling (model scenario #3). The colour code depicts tangential stress in [MPa]. See text for discussion.

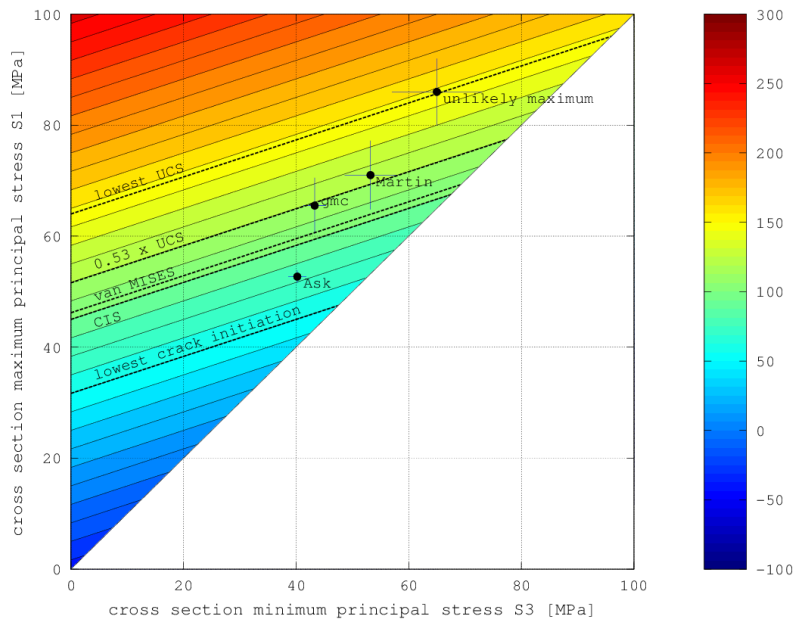


Figure 3.6: Spalling potential diagram for deposition holes during glaciation with hydraulic connection and no bentonite swelling (model scenario #4). The colour code depicts tangential stress in [MPa]. See text for discussion.

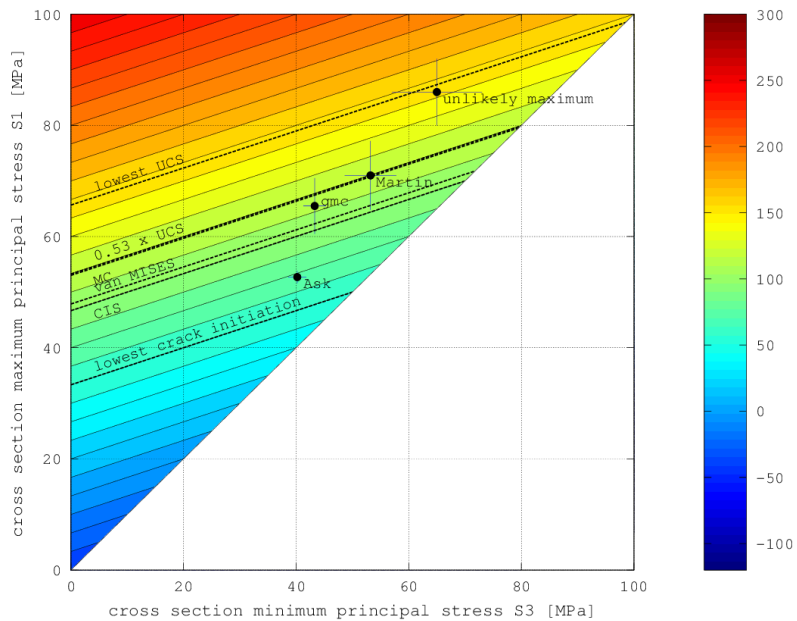


Figure 3.7: Spalling potential diagram for deposition holes during glaciation with hydraulic connection and bentonite swelling (model scenario #5). The colour code depicts tangential stress in [MPa]. See text for discussion.

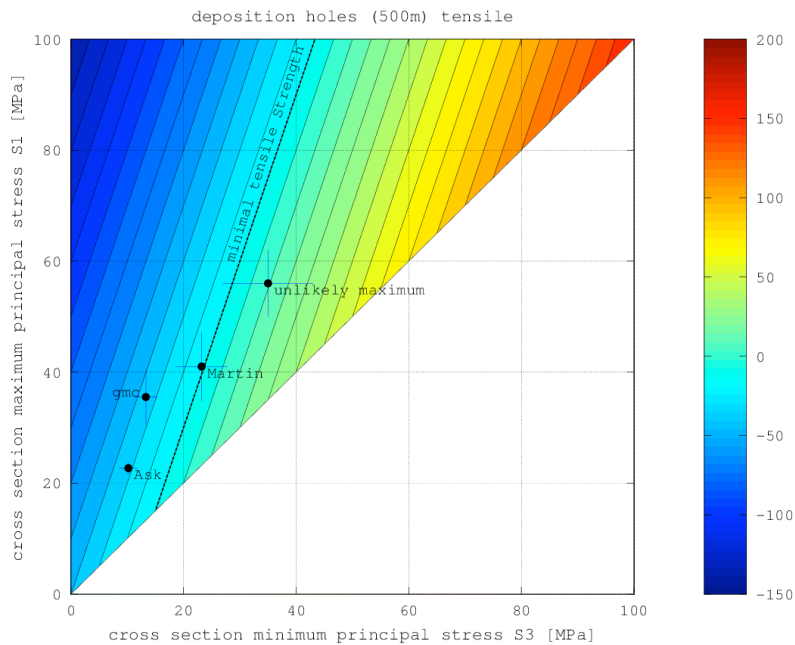


Figure 3.8: Tensile failure potential diagram for deposition holes during glaciation with trapped high fluid pressure but without ice sheet cover (model scenario #13). The colour code depicts tangential stress in [MPa]. See text for discussion.

However, as already seen in the analysis of the deposition holes, spalling is to be expected well below SKB's proposed spalling criterion. Spalling failure in the tunnels is expected during the thermal phase, but not during the excavation phase.

The spalling potential plots for different scenarios are given in Appendix 2, Figures A2.11 - A2.25.

Deposition tunnels - tensile failure potential

The results from the analyses of the potential for tensile failure of the tunnels are summarised in Table 3.4. Excluding the ice cover retreat scenarios and except for two cases (#12 and #13) no tensile failure is to be expected (see Appendix 2, Figures A2.41 - 2.55). With SKB's unlikely maximum stress field scenario some tensile failure might be achieved in the deposition tunnel during the thermal phase (Figure 3.9).

If tensile failure occurs, it has the potential to create thoroughgoing separation along the tunnel axis in the walls by lining up of existing and creation of new fractures leading to fluid pathways that reach several cm into the rock. However, even some tensile stress at the deposition tunnel walls might increase transmissivity of existing fractures.

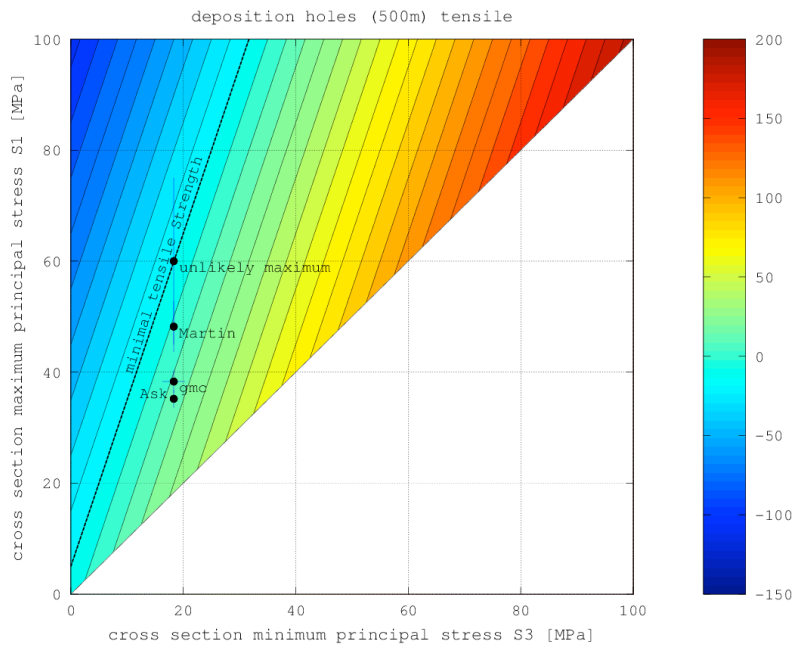


Figure 3.9: Tensile failure potential diagram for deposition tunnels (model scenario #2). The colour code depicts tangential stress in [MPa]. See text for discussion.

3.4. Summary of the analytical analysis of spalling

Tables 3.3 and 3.4 summarize the calculation results for the deposition holes and deposition tunnels, respectively. The ranking scheme for risk of spalling is given in Figure 3.10. In case of tensile failure, the ranking is simply stating if tensile failure might occur “-” or if it is unlikely “+” given a tensile strength of 10 MPa.

The analyses uses for the compressive failure, i.e. spalling, a ranking scheme with four classes (Figure 3.10) and is solely based on the $0.53 \text{ UCS} = 119 \text{ MPa}$ criterion by SKB:

- if the tangential stress is below the lowest reported level for crack initiation, i.e. 60 MPa, the ranking scheme indicates “+”; at this level spalling is not to be expected if the rock properties are correctly reflected by the conducted laboratory campaigns.
- if the tangential stress is below 0.53UCS (ranked “-”) spalling will occur, but becomes less likely with decrease in acting tangential stress. As many as 40% of the deposition holes may be influence by spalling.
- if the tangential stress is above the 0.53 UCS level, it is ranked with “- -” indicating that spalling will be affecting more than 40% of the deposition holes.
- if the tangential stress is above the highest reported UCS, the ranking indicates “- - -” which means severe spalling is to be expected that may reach several decimeters into the formation.

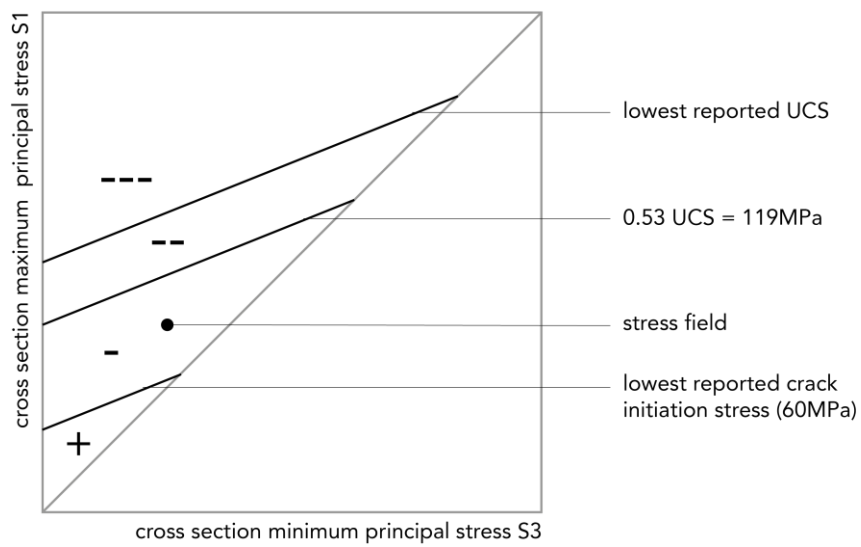


Figure 3.10: Ranking for the summary of spalling potential. If the stress model falls below 0.53 UCS it is ranked as “-”, if above “—”. If it is even above the lowest reported UCS level, it is ranked as “---”, if it falls below the lowest reported crack initiation strength it is labelled “+”.

Table 3.3: Summary of the analytical spalling analyses for deposition holes. com.: compressive, ten.: tensile. The first row of each scenario indicates the maximum and minimum tangential stress (in [MPa]). The maximum spalling depth is based on Diedrich (2007) and the assumption of a least CIS of 85 MPa as reported by Martin (2005). The ranking is according to Figure 3.10 and related explanations.

		Initial stress data					41,0	23,2	35,5	13,3	22,7	10,2	56,0	35,0
		Stress change [MPa]					SKB "most likely"		Geomecon		Ask		SKB unlikely	
Scenario		S _H	S _n	S _V	P _P	P _S	com.	ten.	com.	ten.	com.	ten.	com.	ten.
#1	initial stress	0	0	0	5	0	94,8	23,6	88,2	-0,6	52,9	2,9	128,0	44,0
	max spalling depth [m]	0,05		0,02		-0,17		0,23						
	ranking	-	+	-	+	+	+	-	-	+	+	-	-	+
#2	thermal	27	25	5	5	0	150,8	79,6	144,2	55,4	108,9	58,9	184,0	100,0
	max spalling depth [m]	0,36		0,32		0,13		0,54						
	ranking	--	+	--	+	-	+	-	+	-	+	---	+	+
#3	glacial	30	30	30	5	0	154,8	83,6	148,2	59,4	112,9	62,9	188,0	104,0
	max spalling depth [m]	0,38		0,34		0,15		0,56						
	ranking	--	+	--	+	-	+	-	+	-	+	---	+	+
#4	glacial	30	30	30	35	0	124,8	53,6	118,2	29,4	82,9	32,9	158,0	74,0
	max spalling depth [m]	0,22		0,18		-0,01		0,40						
	ranking	--	+	-	+	-	+	-	+	-	+	--	+	+
#5	glacial	30	30	30	35	5	119,8	48,6	113,2	24,4	77,9	27,9	153,0	69,0
	max spalling depth [m]	0,19		0,15		-0,04		0,37						
	ranking	-	+	-	+	-	+	-	+	-	+	--	+	+
#6	glacial (M1)	53	38	25	5	0	215,8	144,6	209,2	120,4	173,9	123,9	249,0	165,0
	max spalling depth [m]	0,71		0,68		0,48		0,89						
	ranking	---	+	---	+	---	+	---	+	---	+	---	+	+
#7	glacial (M2)	38	28	26	5	0	180,8	109,6	174,2	85,4	138,9	88,9	214,0	130,0
	max spalling depth [m]	0,52		0,49		0,29		0,70						
	ranking	---	+	---	+	--	+	--	+	--	+	---	+	+
#8	glacial (MT8)	22	20	26	5	0	140,8	69,6	134,2	45,4	98,9	48,9	174,0	90,0
	max spalling depth [m]	0,30		0,27		0,08		0,48						
	ranking	--	+	--	+	-	+	-	+	-	+	---	+	+

Table 3.3: Cont.

		Initial stress data					41,0	23,2	35,5	13,3	22,7	10,2	56,0	35,0
		Stress change [MPa]					SKB "most likely"		Geomecon		Ask		SKB unlikely	
Scenario		S _H	S _h	S _V	P _P	P _S	com.	ten.	com.	ten.	com.	ten.	com.	ten.
#9	glacial (M3)	20	18	28	5	0	136,8	65,6	130,2	41,4	94,9	44,9	170,0	86,0
	max spalling depth [m]	0,28		0,25		0,05		0,46						
	ranking	--	+	--	+	-	+	---	+					
#10	glacial (MT10)	20	19	27	5	0	135,8	64,6	129,2	40,4	93,9	43,9	169,0	85,0
	max spalling depth [m]	0,28		0,24		0,05		0,46						
	ranking	--	+	--	+	-	+	---	+					
#11	glacial (MT12)	27	25	26	5	0	150,8	79,6	144,2	55,4	108,9	58,9	184,0	100,0
	max spalling depth [m]	0,36		0,32		0,13		0,54						
	ranking	--	+	--	+	-	+	---	+					
#12	ice retreat	0	0	0	30	0	69,8	-1,4	63,2	-25,6	27,9	-22,1	103,0	19,0
	max spalling depth [m]	-0,08		-0,12		-0,31		0,10						
	ranking	-	-	-	-	+	-	---	+					
#13	ice retreat	0	0	0	30	5	64,8	-6,4	58,2	-30,6	22,9	-27,1	98,0	14,0
	max spalling depth [m]	-0,11		-0,15		-0,34		0,07						
	ranking	-	-	+	-	+	-	---	+					
#14	glacial (MT9)	29	27	28	5	0	154,8	83,6	148,2	59,4	112,9	62,9	188,0	104,0
	max spalling depth [m]	0,38		0,34		0,15		0,56						
	ranking	--	+	--	+	-	+	---	+					
#15	glacial (MT7)	22	21	27	5	0	139,8	68,6	133,2	44,4	97,9	47,9	173,0	89,0
	max spalling depth [m]	0,30		0,26		0,07		0,48						
	ranking	--	+	--	+	-	+	---	+					

Table 3.4: Summary of the analytical spalling analyses for deposition tunnels. com.: compressive, ten.: tensile. The first row of each modeling step indicates the maximum and minimum tangential stress (in [MPa]). The maximum spalling depth is based on Diedrich (2007) and the assumption of a least CIS of 85 MPa as reported by Martin (2005). The ranking is according to Figure 3.10 and related explanations.

		Initial stress data					13,3	23,2	13,3	13,3	13,3	10,2	13,3	35,0	
		Stress change [MPa]					Martin		Geomecon		Ask		SKB unlikely		
Scenario		S _H	S _h	S _V	P _P	P _S	com.	ten.	com.	ten.	com.	ten.	com.	ten.	
#1	initial stress	0	0	0	5	0	51,3	11,7	21,6	21,6	24,7	12,3	86,7	-0,1	
	max spalling depth [m]					-0,18		-0,34		-0,33		0,01			
	ranking					+		+		+		-		+	
#2	thermal	27	25	5	5	0	121,3	1,7	91,6	11,6	82,3	14,7	156,7	-10,1	
	max spalling depth [m]					0,20		0,04		-0,01		0,39			
	ranking					-		+		-		+		-	
#3	glacial	30	30	30	5	0	111,3	71,7	81,6	81,6	84,7	72,3	146,7	59,9	
	max spalling depth [m]					0,14		-0,02		-0,00		0,34			
	ranking					-		+		-		+		--	
#4	glacial	30	30	30	35	0	81,3	41,7	51,6	51,6	54,7	42,3	116,7	29,9	
	max spalling depth [m]					-0,02		-0,18		-0,16		0,17			
	ranking					-		+		+		+		-	
#5	glacial	30	30	30	35	5	76,3	36,7	46,6	46,6	49,7	37,3	111,7	24,9	
	max spalling depth [m]					-0,05		-0,21		-0,19		0,15			
	ranking					-		+		+		+		-	
#6	glacial (M1)	53	38	25	5	0	140,3	48,7	110,6	58,6	101,3	61,7	175,7	36,9	
	max spalling depth [m]					0,30		0,14		0,09		0,49			
	ranking					-		+		-		+		-	
#7	glacial (M2)	38	28	26	5	0	109,3	61,7	79,6	71,6	74,7	70,3	144,7	49,9	
	max spalling depth [m]					0,13		-0,03		-0,06		0,32			
	ranking					-		+		-		+		--	
#8	glacial (MT8)	22	20	26	5	0	85,3	69,7	79,6	55,6	82,7	46,3	120,7	57,9	
	max spalling depth [m]					0,00		-0,03		-0,01		0,19			
	ranking					-		+		-		+		--	

Table 3.4: Cont.

		Initial stress data					13,3	23,2	13,3	13,3	13,3	10,2	13,3	35,0
		Stress change [MPa]					Martin		Geomecon		Ask		SKB unlikely	
Scenario		S _H	S _h	S _V	P _P	P _S	com.	ten.	com.	ten.	com.	ten.	com.	ten.
#9	glacial (M3)	20	18	28	5	0	77,7	77,3	87,6	47,6	90,7	38,3	112,7	65,9
	max spalling depth [m]					-0,04		0,01		0,03		0,15		
	ranking						-	+	-	+	-	+	--	+
#10	glacial (MT10)	20	19	27	5	0	81,3	73,7	83,6	51,6	86,7	42,3	116,7	61,9
	max spalling depth [m]					-0,02		-0,01		0,01		0,17		
	ranking						-	+	-	+	-	+	--	+
#11	glacial (MT12)	27	25	26	5	0	100,3	64,7	74,6	70,6	77,7	61,3	135,7	52,9
	max spalling depth [m]					0,08		-0,06		-0,04		0,28		
	ranking						-	+	-	+	-	+	--	+
#12	ice retreat	0	0	0	30	0	26,3	-13,3	-3,4	-3,4	-0,3	-12,7	61,7	-25,1
	max spalling depth [m]					-0,32		-0,48		-0,46		-0,13		
	ranking						+	-	+	+	+	-	-	-
#13	ice retreat	0	0	0	30	5	21,3	-18,3	-8,4	-8,4	-5,3	-17,7	56,7	-30,1
	max spalling depth [m]					-0,35		-0,51		-0,49		-0,15		
	ranking						+	-	+	-	+	-	+	-
#14	glacial (MT9)	29	27	28	5	0	104,3	68,7	78,6	74,6	81,7	65,3	139,7	56,9
	max spalling depth [m]					0,11		-0,03		-0,02		0,30		
	ranking						-	+	-	+	-	+	--	+
#15	glacial (MT7)	22	21	27	5	0	87,3	71,7	81,6	57,6	84,7	48,3	122,7	59,9
	max spalling depth [m]					0,01		-0,02		-0,00		0,21		
	ranking						-	+	-	+	-	+	--	+

For the deposition holes it becomes clear that after excavation already some spalling is evident for most assumed stress models. During the thermal phase pronounced spalling is to be expected for all stress models (limited if the stress model by Ask et al. (2007) is assumed), and this might influence more than 50% of the deposition holes. The spalling depth might be severe. If swelling pressure from the bentonite might be acting during the thermal phase, which is doubtful and will only be the case for limited number of holes, the spalling will be reduced in such holes.

During the different glaciation scenarios, spalling is to be expected under the assumption that the swelling pressure is not acting. However, as the thermal phase already introduces spalling, the glaciation phases have minor impact on additional spalling.

For deposition tunnels the analyses show in general a lower spalling potential than for the holes, but still pronounced spalling is to be expected during the thermal and glaciation phase.

For both the deposition holes and tunnels it becomes clear that spalling will be an issue. Further it is clear, that the spalling criterion presented by SKB gives the impression that spalling is not as severe as it may be expected by setting the critical value for spalling to 40% of the range of crack initiation stress.

For certain scenarios already during excavation tensile stresses act at the deposition hole walls, and hence existing fractures might be subject to increase of transmissivity. During some glaciation scenarios, where high fluid pressures might be trapped, tensile failure of the deposition holes and tunnels might be an issue, but of minor importance.

For the impact of the different stress models it appears that SKB's "most likely" stress model is "conservative" compared to the newly proposed Geomecon model or the Ask et al. (2007) model, at least in the sense that the generated spalling is more pronounced. However, for the analysis of the potential for tensile failure, which might be a more persistent issue along the tunnel axis when it comes to fluid transport, SKB's approach underestimated the potential.

3.5. The Consultants' assessment on analytical analysis of spalling

The tested criteria (CIS, 0.53 UCS and von Mises) make no great difference for the analysis of the spalling potential. All three criteria plot within about 20 MPa of tangential stress.

The span of crack initiation stress CIS reported by SKB is very broad, spanning about 100 MPa. This has a major impact on the assumed number of excavations experiencing spalling. In contrast, the recent data by Ghazvinian et al. (2012) and data cited therein show that probably the methodology by SKB overestimated the mean CIS and also overestimated the variability of CIS values. It should be considered to analyze additional rock samples to better understand the CIS, which might have major impact on the assumed number of deposition holes experiencing spalling.

The spalling criterion defined by SKB uses a mean CIS value to predict spalling. As the experimental data varies considerably, this way of presenting the spalling potential suggests far more stable conditions than the experimental data reflects. The mean value of the data that is available in individual strength values to the reviewers (which is about 50% of the stated number of data points only) is 60 MPa larger than the smallest value, which is a considerable amount at a mean value of 119 MPa.

A rough estimation of the excavations that may exhibit spalling yielded some hundred deposition holes during the excavation phase and about 90% during the thermal phase; at least when SKB's values for CIS and related variation thereof are used. This includes all deposition holes exhibiting spalling, which does not imply

that the spalling depths are of significant amounts. A further estimate of the deposition holes exhibiting more than a certain spalling depths has not been performed in this study, as this would be quite uncertain given the doubtful data base of UCS and CIS at current stage.

If the data by Ghazvinian et al. (2012) would have been used, which suggests a CIS of about 100 MPa while the lowest CIS is about 90 MPa, the picture would be considerably less favorable.

For certain stress models some tensile activation of existing fractures or creation of new tensile fractures could occur at deposition tunnels and holes. The tensile fractures have the potential to create tunnel parallel persistent fluid pathways in the wall. As the analysis on the tensile fracturing potential is quite stress model sensitive, the stress model needs to be verified before distinct analyses and related conclusions can be drawn on that issue.

4. Numerical simulation of spalling

As part of the authors' assessment, independent numerical simulations of spalling are to be performed. A stress evolution simulation based on input data from SKB is performed and the potential for spalling is analyzed by comparing the obtained stress paths with SKB's spalling criterion. SKB's spalling criterion assumes spalling if the tangential stress on the excavation walls exceeds 53% of the unconfined compressive strength.

The stress path evolution is reported and discussed such based on the numerical results, that any tangential stress based criterion can be easily discussed from the presented data.

4.1. SKB's presentation

A combined method of numerical tools (3DEC) and linear elastic analytical solutions has been used by SKB for the assessment of spalling (SKB TR-10-23). Thereby the spalling strength was assumed to be 52%-62% of the unconfined compressive strength UCS. This assumption is based on in situ experiments, e.g. ASPE project and CASP project, and direct laboratory measurements (SKB R-08-116, p.121, Figure C-3). Crack initiation pressures as low as 60 MPa (SKB TR-08-05, p.218, Table 7-3), or about 40% of the respective UCS were also measured but not considered by SKB in their analysis.

Six different stress fields at repository depth have been evaluated by SKB. The stress fields are taken from SKB (TR-10-52, p.298, Table 6-59) and include the "most likely" stress-depth relationship with error spans (Glamheden et al., 2007, Martin 2007) and the maximum proposed stress model ("unlikely maximum"). The minimum stress field (Ask et al., 2007) has been neglected. Five glacially-induced stress fields are superposed on to the chosen stress fields at times of maximum glaciation, ice retreat and fore-bulge. The glacially-induced stresses are taken from Lund et al., (2009, model M T9) and are assumed to be constant with depth.

The temperature development due to the spent nuclear fuel is simulated by canisters with an initial power of 1700W placed into each deposition hole. The heat decays by power-law (Hökmark et al., 2009, SKB R-09-04).

The risk for spalling was evaluated for the construction, thermal and glacial phase by small-scale models located at different positions in the repository (Hökmark et al., 2010, SKB TR-10-23, p.148, Fig. 9-1). The models show that spalling will be the exception during construction and operational phase, but is likely to take place for a large majority of deposition holes during the thermal phase. During excavation and operation spalling occurs under unfavorable orientation of the far field stresses in the upper part of the deposition holes, where stresses are maximized due to the overlaying deposition tunnel. During glaciation, Hökmark et al. (2010, THM report) assume that spalling is unlikely to occur since glacially-induced stresses are in the same order of magnitude as thermally-induced stresses, i.e. spalling already occurred during heating, and a significant swelling pressure of the bentonite backfill should suppress spalling.

Regarding the roof of deposition tunnels, spalling is expected to occur only exceptional in case the maximum horizontal stress aligns at large angles to the

tunnel or if the maximum stress takes the largest values within uncertainty given in the Site Descriptive Model (SKB TR-08-05).

4.2. Motivation of the Consultants' assessment

As long-term safety should be addressed in all analyses, it is important to understand the stress evolution during different loading scenarios on the repository. If spalling is introduced, it may create fluid pathways along the deposition holes and deposition tunnels. Through such pathways radionuclides may be transported to permeable fracture zones connected to the biosphere at future times.

Whereas the scoping analysis in the previous chapter was not capable of analysing the robustness of the assumptions of the stress field, the numerical simulation in this chapter was laid out such that the stress path's influence on spalling may be evaluated. In sensitivity analyses one can alter certain parameters, such as poroelastic response and deformation properties of fault zones, and study their influence on the spalling potential.

4.3. The Consultants' Assessment on the simulation of stress field evolution and spalling

In order to assess the occurrence of spalling a simplified model of the geological setting at Forsmark was set up and analyzed. The FEM package COMSOL Multiphysics (COMSOL AB, Stockholm, Sweden, www.comsol.se) was used to evaluate the spalling around tunnel and deposition holes in the proposed repository. COMSOL is well established in earth science related academia and industry. The software package is capable of coupling thermo-hydro-mechanical processes, which are expected to affect the repository. The simulations include the initial stress assumptions, but also the long term thermal evolution due to heating of the spent nuclear fuel canisters and response of the in situ stresses to a potential glacial cycle. The deposition tunnels and holes are not modelled directly, but the stresses from the simulations are applied to an analytical representation of the excavations.

4.3.1. Model description

The simplified model as was used for the simulations is described in the following. It defines the base case model for all further analyses in this study. Any deviation from the described base case scenario will be highlighted in the respective sections.

Model geometry

The geometry of the FEM model is based on the NW-SE section of the Forsmark site shown in Figure 4.1 and a series of top views of the candidate area given in the D2 layout report (SKB R-08-116, Figures 4-7 to 4-10). The model spans a volume of 4.4 km in length, 2.5 km in width and 1.1 km in depth (Figure 4.2). The longest axis is in direction NW-SE, sub-parallel to S_H . Four major domains have been distinguished in this model to account for different thermal, hydraulic and mechanical behavior. It is however only a simplified model to the in situ geological conditions in Forsmark as defined by SKB.

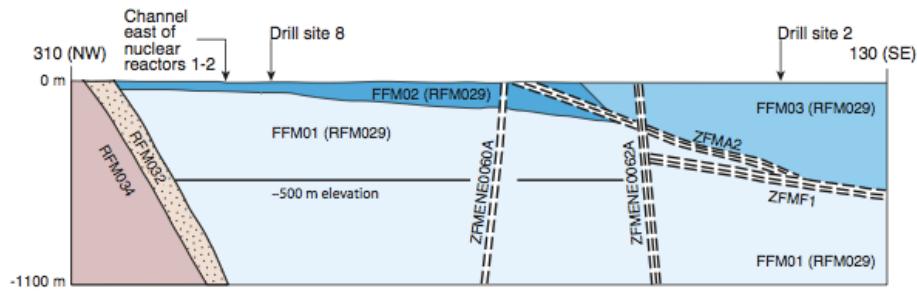


Figure 4.1: NW-SE profile showing the rock domains, fracture domains and the deformation zones at Forsmark (from SKB R-08-116, Figure 3-2).

The main rock volume is RFM029, which hosts the future repository. RFM029 is subdivided into two fracture domains, with FFM01 making up the majority of the model that is overlain by the shallow block FFM02, which becomes FFM03 South-East of the repository footprint and similar properties. RFM032 and RFM034 are included as wedge and inclined sheet respectively. The model domain also includes deformation zones ZFMENE0060A, ZFMENE0062A and ZFMA2 as planar elements.

Rock Domains

The model is divided into three major rock domains (Figure 4.2). The largest volume is taken up by rock domain RFM029, which is the dominant rock domain in the Forsmark tectonic lens and in the target volume. It is predominantly composed of medium grained granites and granodiorites that underwent amphibolite-facies metamorphism during the Svekofennian orogeny. Subordinate rock types include pegmatitic granite, fine- to medium grained metagranitoid and tonalite, and amphibolite which occur as isolated minor bodies, lenses and dyke-like sheets (Stephens et al., 2007, SKB R-07-45). Rock domain RFM045 which forms a rod-like shape in the target volume, adjacent to RFM029, and is basically composed of the same rock types. In contrast to RFM029 the dominant lithology differs in grain size (aplitic metagranite) and shows Na-K alteration (albitisation). The subordinate lithologies make up more of the total volume. RFM045 generally shows larger stiffness than RFM029 due to reduced content of K-Feldspar and larger Quartz contents (SKB TR-10-52) and therefore could be neglected in the model to maintain a simple geometry while ensuring a conservative approach. In RFM029, two fracture domains are distinguished, FFM01 and FFM02.

RFM032 and RFM034, constricted to the Forsmark tectonic lens, also exhibit amphibolite-facies granite. RFM032 is described as an inhomogeneous rock domain with felsic to intermediate metavolcanic rocks and abundant sheets of amphibolite. RFM034 differs mainly in the rocks fabric, showing higher grades of ductile deformation as it is situated in the hinge of a synform that is part of a large sheath fold structure inside the Forsmark tectonic lens (R-07-45). The fold axial plane is sub-vertical with a fold-axis moderately plunging towards the SE, such that the lithological contacts show varying strike towards the northwestern end of the candidate area. The model shows planar contacts with constant strike between RFM034, RFM032 and RFM029.

The properties assigned to the domains in the base model are given in Table 4.1 as reproduced from SKB (TR-08-05).

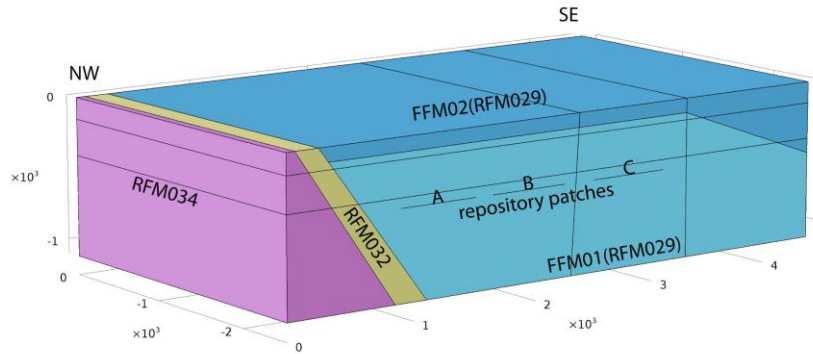


Figure 4.2. Geometry of the COMSOL FEM model with rock and fracture domains, and location of the repository patches. The parameters are described in the respective sections.

Fracture Domains

Rock domain RFM029 is divided into three fracture domains, FFM01, FFM02 and FFM03, to account for differences in geomechanical and hydraulic properties. FFM02 represents the shallow rock volume that extends up to a depth of 150 m and shows significantly higher fracture intensity compared to FFM01 due to surface stress release (SKB R-08-116). There are two conspicuous sets of fractures, one shows gently dipping to sub-horizontal planes, the other shows steeply dipping to sub-vertical planes. They are open and hydraulically interconnected. This zone is increasing in depth towards SE (Figure 4.2), including those parts of fracture domain FFM03 that belong to RFM029. Figure 4.2 shows also the position of the repository panels (also called “patches” in this report).

FFM01 is situated below the stress-released fractured rock. The same two fracture populations as in FFM02 are present but fractures are less abundant. In the model FFM06 has been integrated into FFM01 in RFM029. It corresponds to rock domain RFM045 and as this domain has been assigned the same properties as RFM029, the authors consequently incorporated FFM06 in FFM01.

Deformation Zones

The two steeply dipping deformation zones, ZFMENE0060A and ZFMENE0062A, and deformation zone ZFM02A are modelled as thin elastic layers (Figure 4.3). The elastic properties assigned to those layers are summarised in Table 4.2 and correspond for the base model to the mean values of properties for fractures in FFM01 that are given in SKB (TR-10-23, Table 4-3).

The thin elastic layers meet the following conditions:

$$S \cdot n = k_A \cdot u \quad \text{Eq. (4.1)}$$

Table 4.1: Rock Mechanics properties assigned to the rock domains in the base model.

	FFM01 (RFM029)	FFM02 (RFM029)	RFM032	RFM034
Young's modulus, E [GPa]	70	70	70	70
Poisson's ratio, ν [-]	0.24	0.24	0.24	0.24
Generic density, ρ [kg/m ³]	2.700	2.700	2.700	2.700
Heat capacity, C [MJ/m ³ K]	2.06	2.06	2.06	2.06
Mean thermal conductivity, λ_m [W/m ² K]	3.57	3.57	3.57	3.57
Thermal expansion coefficient, α_{th} [1/K]	7.7e-6	7.7e-6	7.7e-6	7.7e-6
Biot coefficient, α [-]	1	1	1	1
Porosity, θ [-]	0.01	0.05	0.01	0.01
Permeability, k_f [m ²]	1.0e-15	1.0e-12	1.0e-15	1.0e-15

where S is the stress field, n is the normal vector of the boundary, k_A is the spring constant, and u is the displacement vector composed of the displacement on each side of the layer, and optional an additional pre-defined displacement. The layers allow fracture flow, according to a tangential derivative of the Darcy law, describing the flow along an internal boundary

$$q_f = -\frac{k_f}{\mu} d_f (\nabla_{TP} + \rho g \nabla_T D) \quad \text{Eq. (4.2)}$$

where, q_f is the volume flow rate per unit length of the fracture, κ_f is the fracture's permeability, μ is the fluid dynamic viscosity, d_f is the thickness of the fracture, ∇_T denotes the gradient operator restricted to the fracture's tangential plane, p is the pressure, ρ is the fluid density, g is the acceleration of gravity, and D represents the depth.

Outer model domain boundaries

The model domain boundaries facing towards NE and SW are modelled as symmetry boundaries. Symmetry boundaries can be understood as a combination of Dirichlet and Neumann condition, which prescribes no penetration and vanishing shear stresses. The boundaries facing towards NW, SE and downward are modelled as roller boundaries, where displacements are free in the plane of the boundary but fixed in the out-of-plane direction. The boundary facing upward, i.e. the biosphere, is free.

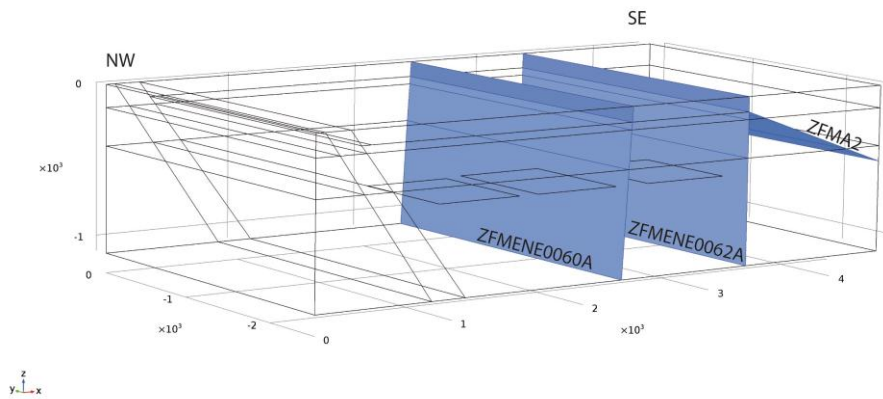


Figure 4.3: Deformation zones ZFMENE0060A, ZFMENE0062A and ZFMA2 and their relative position in the COMSOL model.

Implementation of the stress field

Within this study, positive stresses indicate compression and negative values indicate tension in accordance with typical rock mechanics convention.

Figure 4.4 exemplarily displays the stresses calculated within a stationary study, with SKB's "most likely" stress field as given in the respective section above.

Thermal evolution

The horizontal extension of the repository is presented e.g. SKB (TR-08-116, Figure 4.5). The future repository depth is planned to be at around 470 m (SKB TR-08-116, p.95). The geometry of the repository is modelled as a layer that consists of several patches (Figure 4.6), where a temperature function is assigned to each patch. In the model the depth of the repository is -500m. Note that patch D is larger than in SKB's Layout D2 (SKB TR-10-23, p.57), where the south corner is not assumed to be used. As our model uses a symmetry plane, the three patches are divided as shown in Figure 4.6.

The initial temperature gradient is 23°C/km, reaching 11.5°C at repository depth.

Table 4.2: Properties of the steep deformation zones in the model (SKB TR-08-05, Table 7-4).

Property	(for equivalent thin elastic layers)
Porosity, θ [-]	0.1
Permeability, k_f [m^2]	1.0e-8
Fracture thickness, d_f [m]	0.05
Normal stiffness, $k_{A,n}$ [GPa/m]	656
Shear stiffness, $k_{A,t}$ [GPa/m]	34

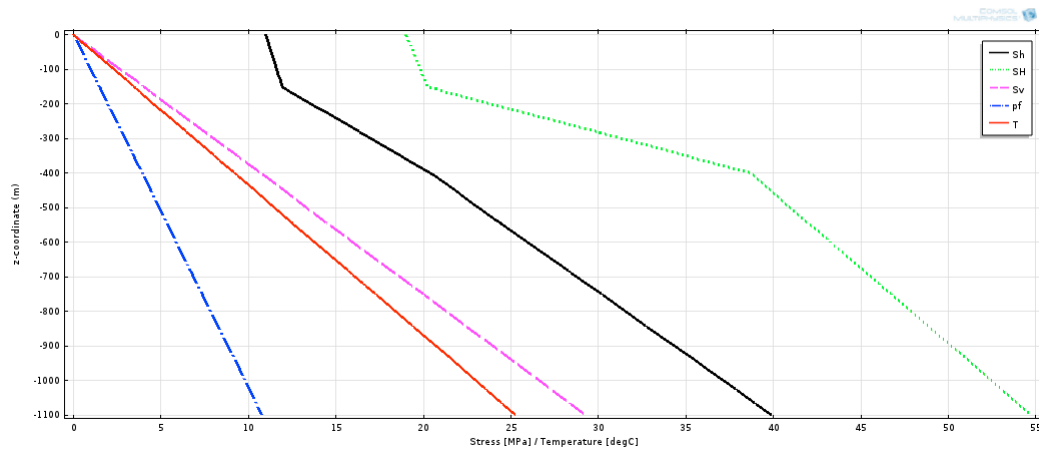


Figure 4.4: Stress and pore pressure change with depth as pre-inscribed to the model. The stress field by Martin (2007), i.e. SKB's "most likely" scenario, is represented here.

The effect of the thermal activity of the spent nuclear fuel on the rock temperature was simulated by Hökmark et al. (2010, SKB TR-10-23). The maximum rock wall temperature increase due to heating is about 48°C (Figure 4.7). Hökmark et al. (2010) simulated two different rock domains with different spacing of the deposition holes, leading to lower deposition hole wall temperatures in some areas of the repository. The authors only consider rock domain RFM029 simulation results for the sake of simplification. As the temperature increase in this rock domain is higher, the approach is conservative as leading to larger thermal expansions.

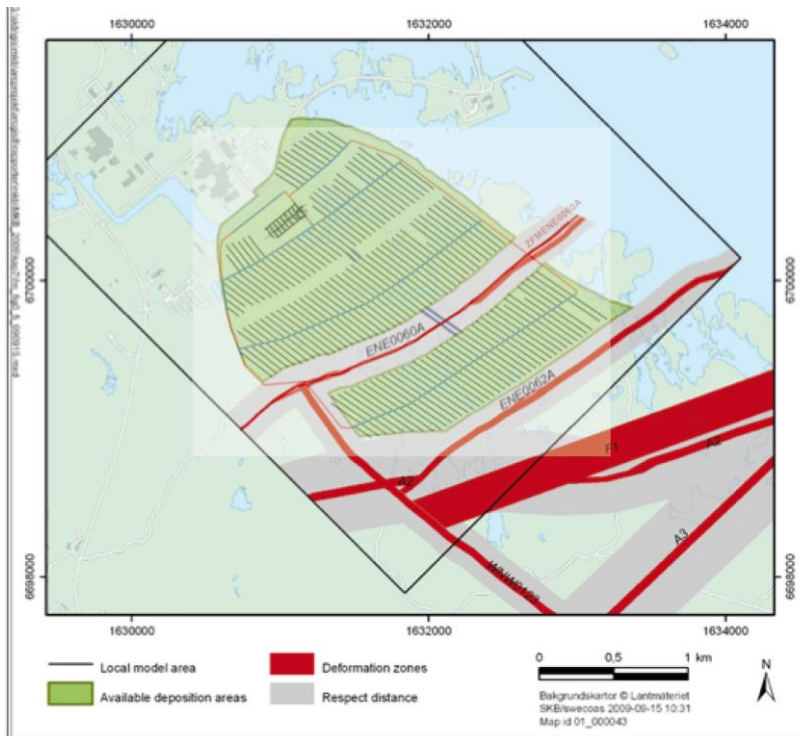


Figure 4.5: Deposition area, deposition tunnels and deformation zones (from R-08-116, Figures 4-8 and 4-9).

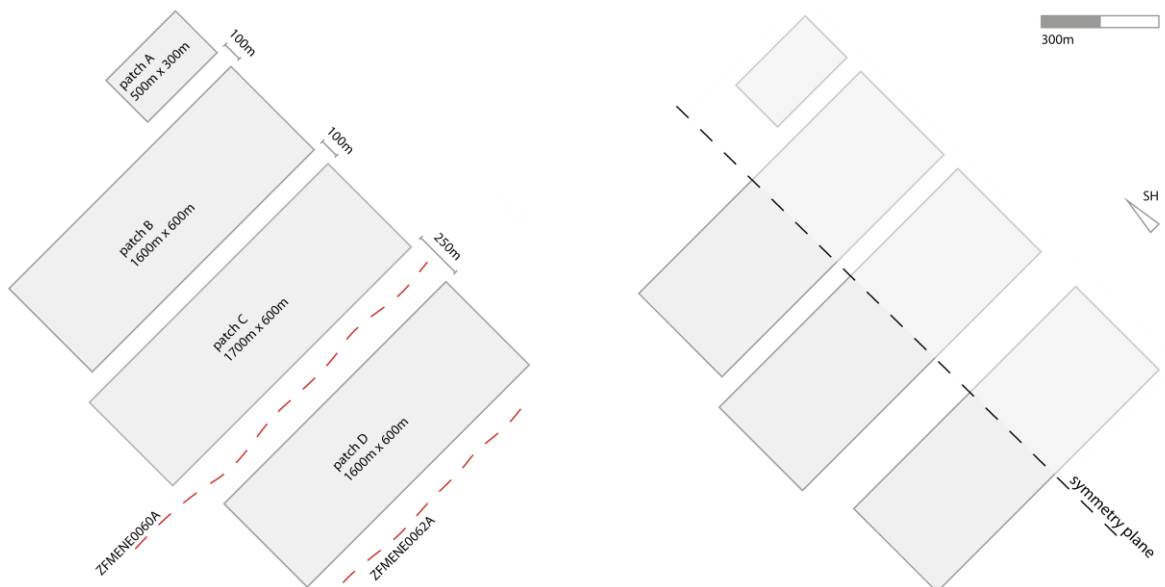


Figure 4.6: Model of the repository layout for simulation. (left) The repository layout is modelled as four patches of rectangular shape, for the basic simulations the model is cut into half (right) and only the lower left half with respect to the symmetry plane is used in the simulation.

According to Hökmark et al. (2009, SKB R-09-04) the average temperature increase in the deposition panels reaches peak values of 34°C after 30 years (Figure 4.8). In our model the temperature evolution of the three patches as described earlier will be decreasing exponentially from peak to the initial temperature of 11.5°C after 100.000 years (Figure 4.9).

The whole model for the site has an initial temperature of 11.5°C as measured at repository depth (SKB R-08-65). The repository itself is divided into three patches cut in half by the symmetry plane. The assigned temperature is a function of time and taken from SKB TR-10-23, Figure 5-14 (see Figure 4.9). Despite the symmetry boundaries, the remaining outer boundaries act as thermal insulation, which means that heat cannot be transferred across the boundary.

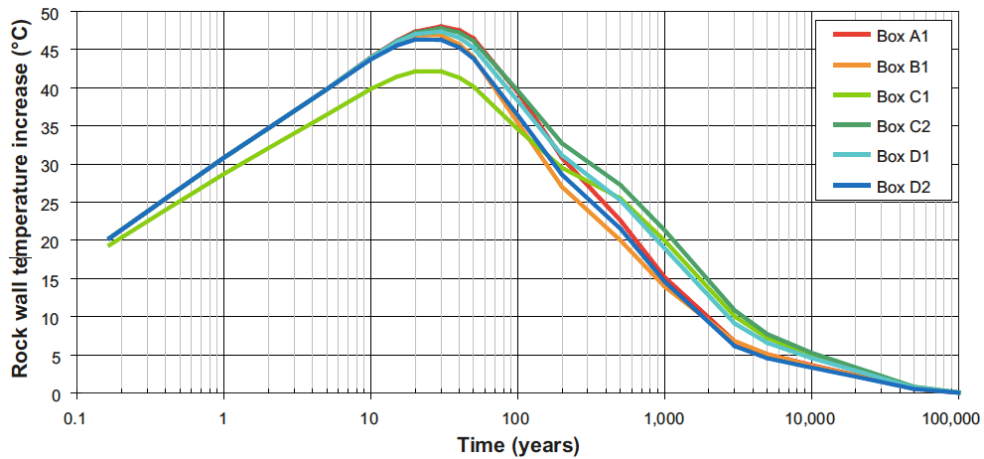


Figure 4.7: Rock wall temperature increase as simulated by Hökmark et al (2010, SKB TR-10-23, Figure 5-14).

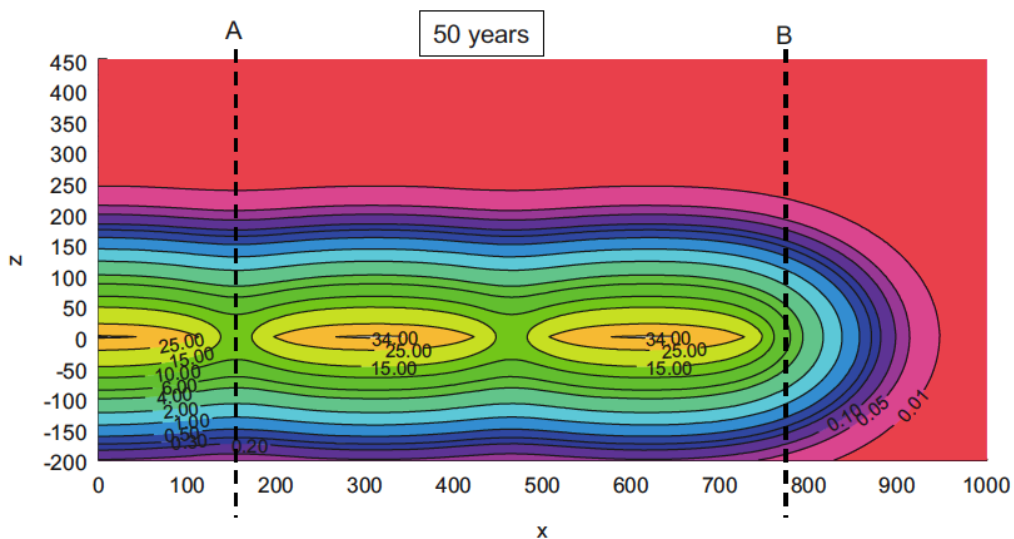


Figure 4.8: Rock temperature increase calculated using rectangular heat sources (Hökmark et al., 2009, SKB R-09-04, Fig. 4-2).

To model the thermally induced stresses due to thermal expansion of the material during heating the thermally induced strain, ε_{th} , is given by:

$$\varepsilon_{th} = \alpha_{th} (T - T_{ref}) \quad \text{Eq. (4.3)}$$

where α_{th} is the thermal expansion coefficient, T is the temperature and T_{ref} is the strain-free reference temperature.

Glacial Cover

As the repository for spent nuclear fuel will be exposed to the effects of a glaciation, the authors consider SKB's reference glaciation scenario in the long term safety assessment SR Site. The load of the ice sheet will induce stress changes which will potentially affect spalling. SKB's reference ice sheet evolution is derived from the Weichselian ice sheet of Näslund (2006, Figure 4.10). Lund (2009, SKB TR-09-15) modelled the stress evolution during this glacial cycle in order to evaluate fault stability.

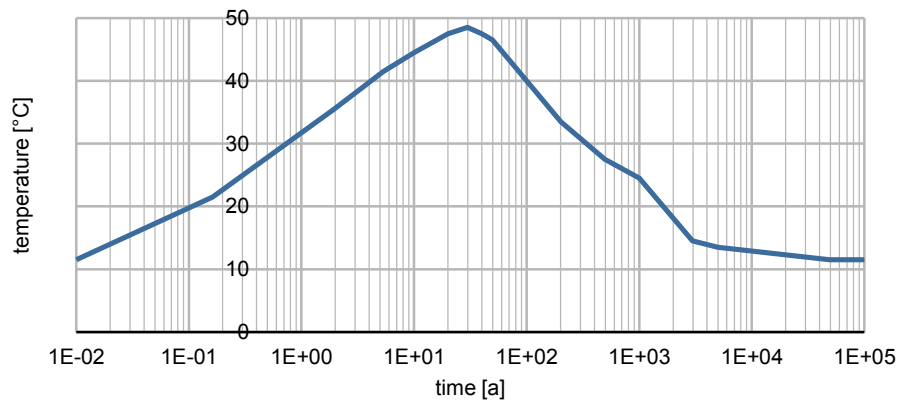


Figure 4.9: Temperature of the repository panels vs. time as modelled in this study.

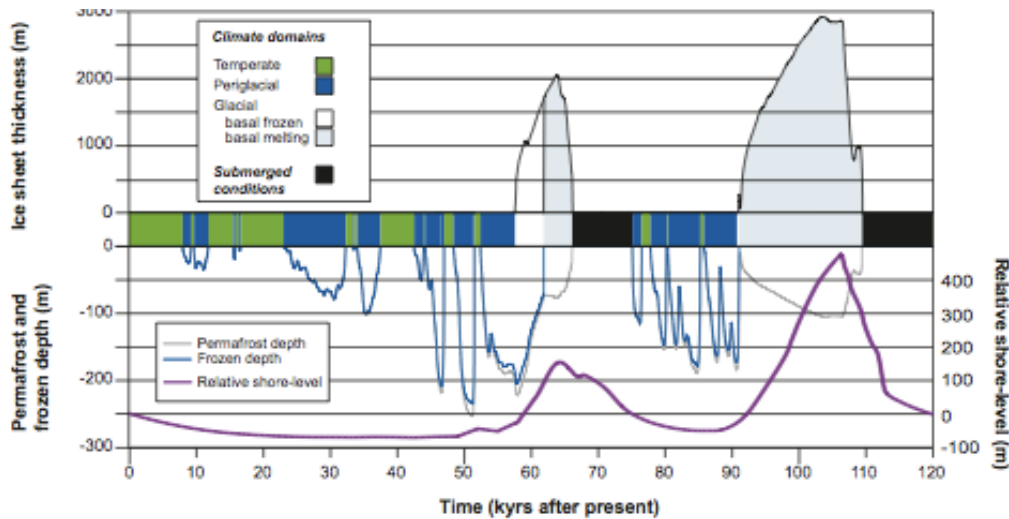


Figure 4.10. Reference glacial cycle (from SKB TR-11-01, Vol.1, Figure S-9).

The increase in vertical stress directly correlates with the ice sheet thickness (Figure 4.11). The glacial load is implemented by ascribing the vertical stress changes over time to the upper boundary plane in the COMSOL model. The resulting horizontal stresses will be simulated according to the elastic properties of the model domain and deformation zones. Any influence of isostatic rebound or tectonic stresses is not accounted for. Also any stress variations due to the movement of the ice sheet is not accounted for.

Computations during simulation and post-processing

For the analysis of spalling the tangential stress is calculated from the simulated stress components by means of the Kirsch equations as outlined elsewhere in this report.

According to SKB the centre-to-centre spacing for the deposition tunnels is planned to be 40 m horizontally (SKB TR-08-116, p.29). The deposition tunnels will have a length of < 300 m (SKB TR-08-116, p.37). The deposition tunnels will be aligned parallel to sub-parallel (at most $\pm 30^\circ$) to the maximum horizontal stress (SKB TR-08-116, p.37). The roof level of the highest located deposition tunnel shall be below the 450 m level (SKB TR-08-116, p.37). The centre-to-centre spacing for the deposition holes is set to 6 m in RFM029 and 6.8 m in RFM045 (SKB TR-08-116, p.29).

In this study the deposition tunnels are assumed to be oriented with their axis parallel S_H , and the vertical deposition holes are subject to S_H and S_h . The influence of the stress redistribution of the deposition tunnels on the deposition holes is not accounted for at this stage of analysis, i.e. a section of the deposition hole distant enough from the floor of the deposition tunnel is considered.

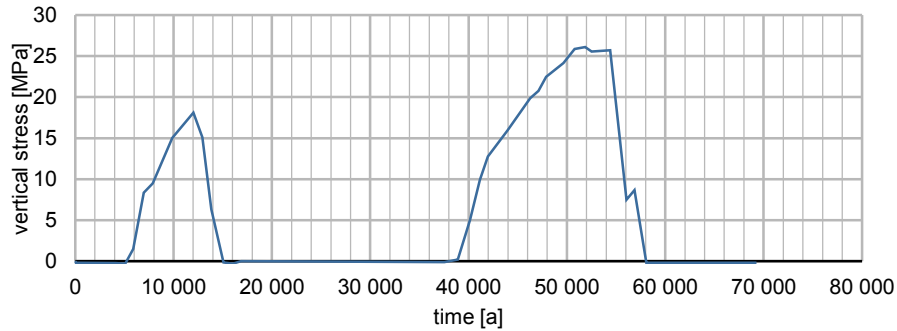


Figure 4.11: Glacially induced vertical stress changes corresponding to ice sheet thickness as modelled in this study.

4.3.2. Simulation of temperature evolution

The temperature function that was assigned to the models repository panels together with the thermal conductivity that allows conductive heat transport are the driving forces of the temperature evolution in the model. Depending on the spacing between the patches, the interference is more or less pronounced, as shown in Figure 4.12 for a series of time steps ranging from 1 year to 1,000 years. The thermal expansion of the rock domains causes changes in principal stresses, generally increasing their magnitudes. Due to the model's free upper boundary the vertical expansion component can be accommodated by uplift of the surface to a large extent, i.e. the model extends in z direction. The horizontal expansion component is accommodated by increase in horizontal principal stresses.

4.3.3. Simulation of stress evolution and spalling potential from initial stress field models

In the following, the simulation conditions are given for the respective simulation runs along with the key results. All models are built upon the base model as described before and the deviations from the base model are given in the description to the dedicated simulation.

The simulations analyse the influence of the initial stress field assumption on the evolution of the spalling potential. The stress difference as given in the various diagrams is always calculated from the respective principle stresses in the stated cross section, e.g. $S_H - S_h$ for a horizontal cross section (x-y-plane).

Effects of stress model variations

In order to assess the impact of different stress models and faulting regimes, the three proposed stress models are applied to the base model for simulation. The spalling potential of each of the three models throughout the complete loading history is presented in terms of tangential stress evolution.

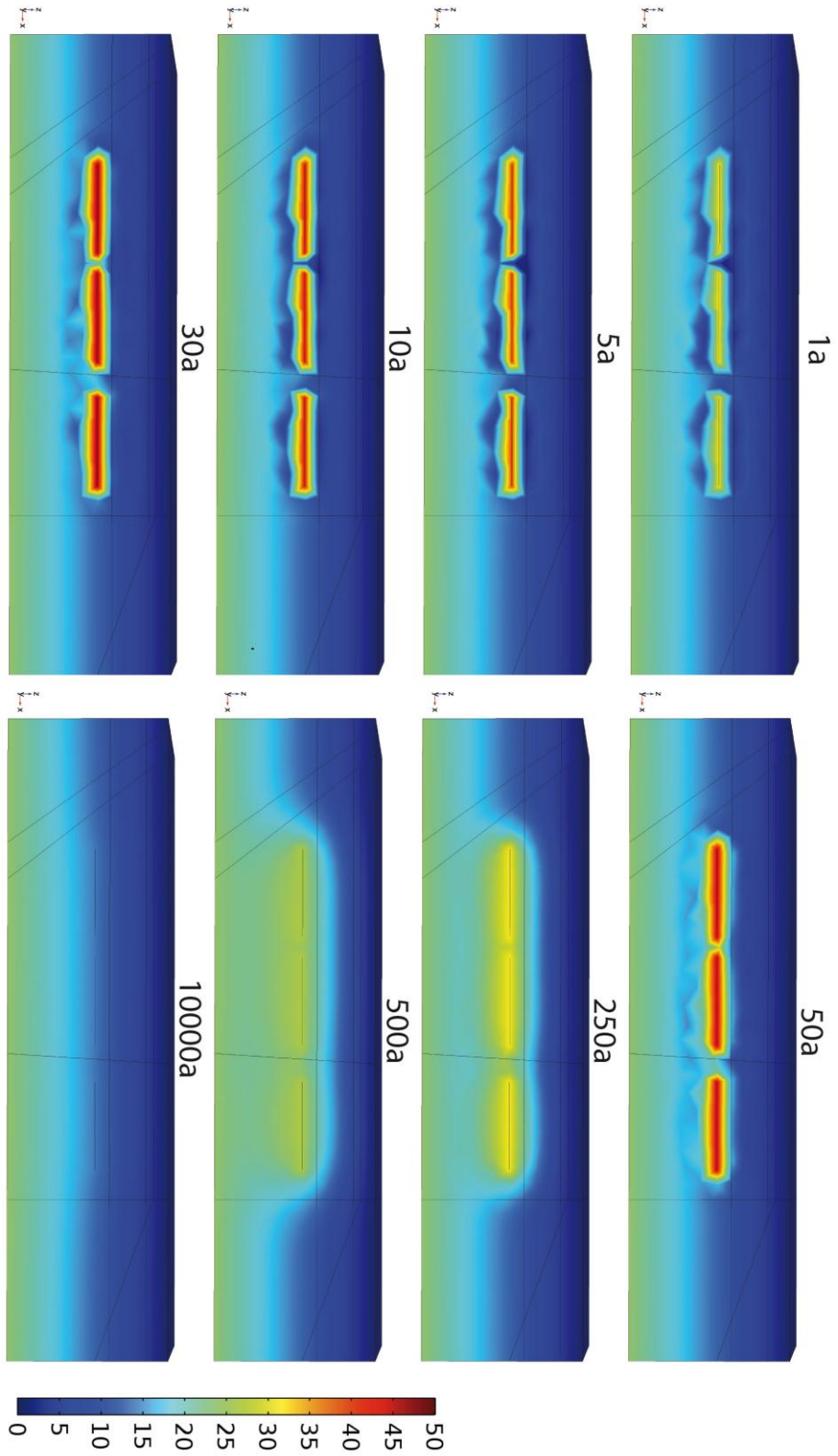


Figure 4.12. Simulated temperature evolution during the heating phase. The initial temperature gradient is 23°C/km, reaching 11.5°C at repository depth.

Table 4.3: Stress magnitudes at repository level for the three models considered in further analysis.

Simulation series	Variable	Parameterization	Simulation ID
MISF	initial stress field	Ask et al., (2007, SKB P-07-206)	MISF1
		Martin (2007, SKB R-07-26)	MISF2
		Geomecon (gmc)	MISF3

Simulation MISF1

The evolution of stress with the initial stress field model by Ask et al. (2007) and the base model is given in Figure 4.13 for the midpoint of patch B where maximum stress increase is observed. The stresses rise rapidly after deposition of the canisters due to the thermal heating and reach a maximum after 30 years. Subsequently the stresses drop according to the imposed temperature scheme. By the time the vertical stress increases due to the ice sheet cover the thermally induced stresses have declined and the ice cover increases the horizontal stresses also.

From initial strike-slip conditions the stress regime becomes a reverse faulting regime during the thermal phase. During the simulation of the glacial phase by increasing vertical load the stress regime changes from strike-slip to normal faulting.

Figure 4.14 shows the evolution of stress difference in the repository for the x-y-plane (for the analysis of deposition holes) along a horizontal scanline through the repository in NW-SE direction. The stress difference is shown for different time steps during the heating phase, which reaches peak values after 30 years after deposition of the canisters and coincides with the thermal peak as described earlier. The largest variation in stress difference is in the rock volumes between the patches.

The evolution of stress difference on a vertical cross section for the deposition tunnels is given in Figure 4.15. The change in stress difference is largest after 30 years and inside the patches. Between the patches the change in stress difference is smaller.

For the glaciation phase the change in stress difference is plotted in Figures 4.16 and 4.17. The change in stress difference is negligible for the deposition holes (horizontal cross section), whereas the deposition tunnels see a pronounced increase in stress difference due to the increase in vertical stress (vertical cross section).

Calculating the tangential stress on the deposition tunnels and deposition holes from the simulated stresses and their evolution yields an understanding for the evolution of spalling potential. Figure 4.18 shows the analysis. Both for the deposition tunnel and deposition hole the tangential stresses stay below the $0.53 \cdot \text{UCS}$ threshold at all times. However, during the thermal phase for both the deposition holes and tunnels also. During the glaciation phase for the tunnels the tangential stresses are above the 60 MPa threshold, which was the lowest measured crack initiation stress from crack initiation analysis by SKB.

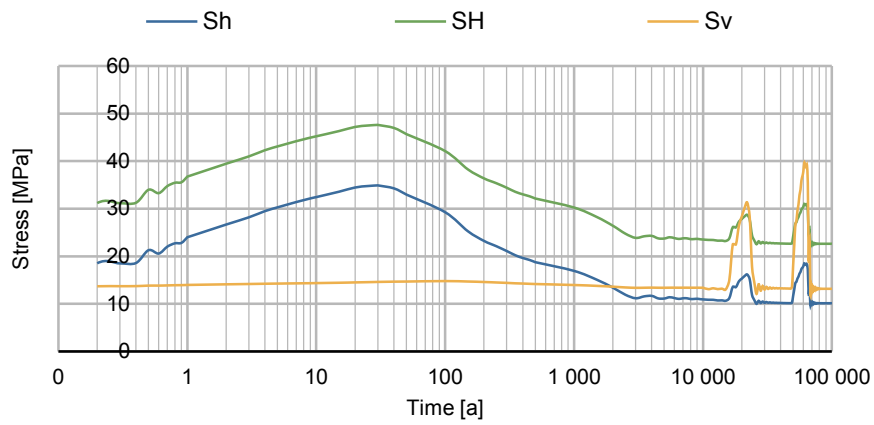


Figure 4.13: Temporal evolution of principal stresses for the stress model by Ask et al. (2007) at the centre point of patch B. The vertical stress component is reduced due to the free upper boundary of the model (see text).

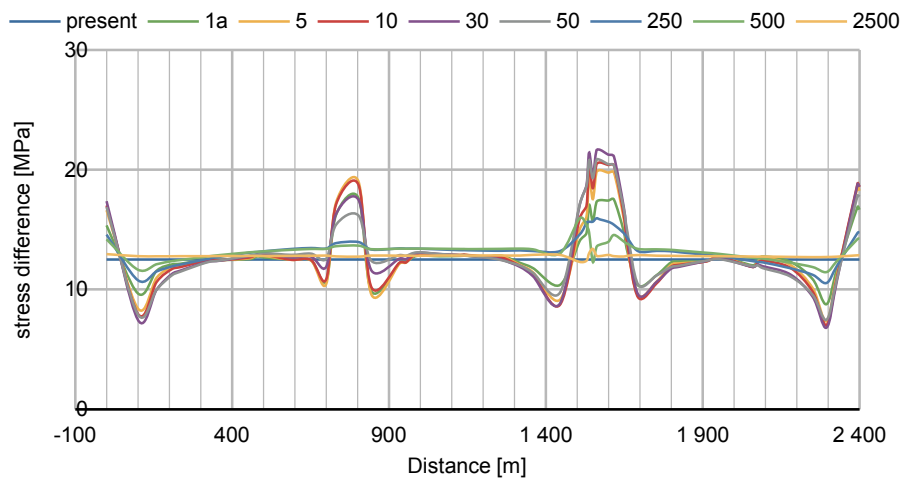


Figure 4.14: Evolution of stress difference for a horizontal cross-section (for deposition holes) vs. distance along the repository for various time steps during the thermal phase. The scanline lies 500 m from the symmetry plane in y-direction.

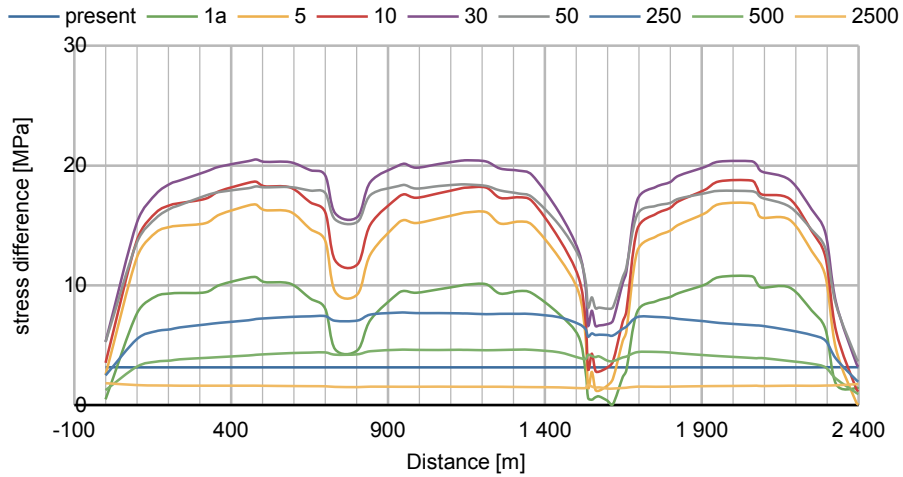


Figure 4.15: Evolution of stress difference for vertical cross-section (for deposition tunnels) vs. distance along the repository for various time steps during the thermal phase. The scanline lies 500 m from the symmetry plane in y-direction.

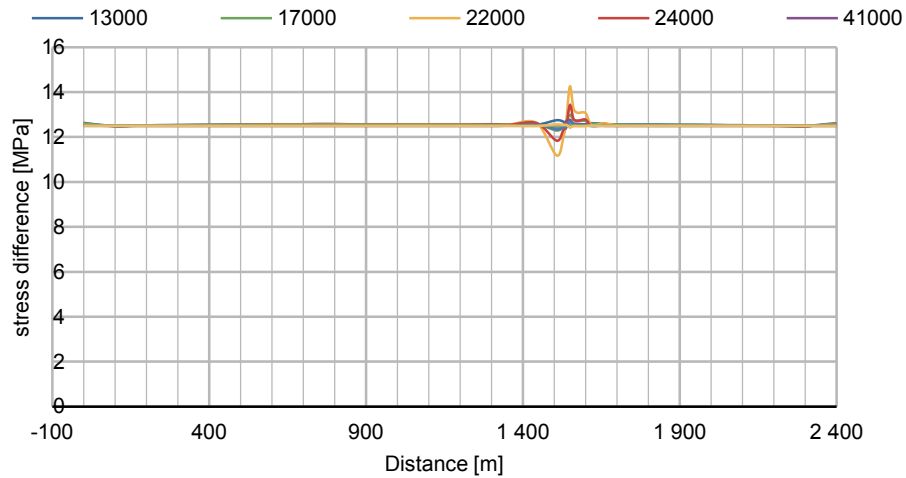


Figure 4.16: Evolution of stress difference for horizontal cross section (for deposition holes) vs. distance along the repository for various time steps during the glaciation phase. The scanline lies 500 m from the symmetry plane in y-direction. The small kink at 1.500 m is a mesh artifact.

The minimum tangential stress is positive at all times, indicating that tensile failure of the walls of the deposition tunnels and deposition holes is not to be expected with the base scenario during the thermal and glacial phase.

Simulation MISF2

The evolution of stress with the initial stress field model by Martin (2007, SKB's "most likely") and the base model is given in Figure 4.19 for midpoint of patch B where the stress increase is at its maximum. The stresses rise rapidly after deposition of the canisters due to the thermal heating and reach a maximum after 30 years.

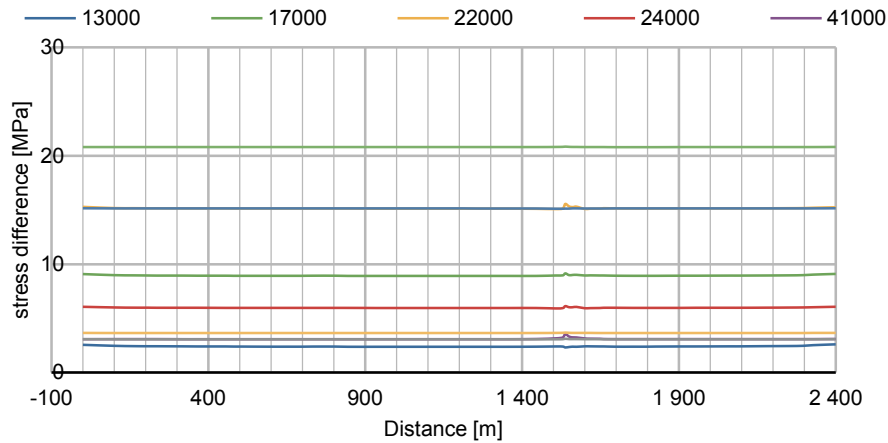


Figure 4.17: Evolution of stress difference for vertical cross section (for deposition tunnels) vs. distance along the repository for various time steps during the glaciation phase. The scanline lies 500 m from the symmetry plane in y-direction.

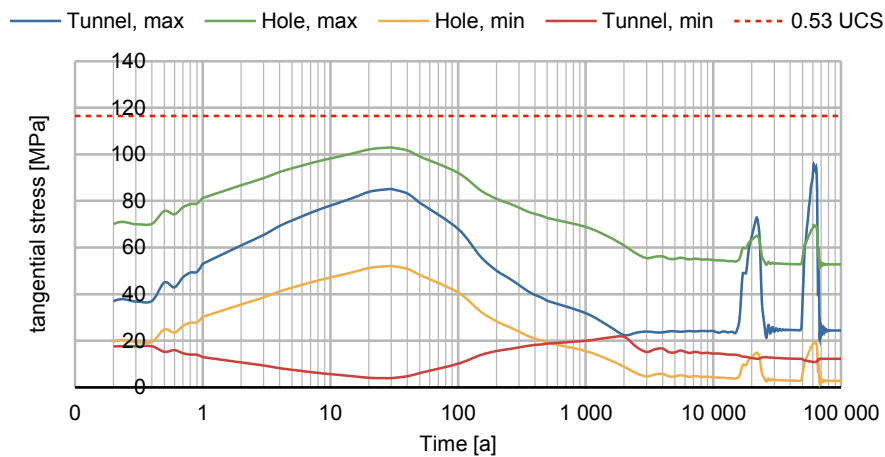


Figure 4.18: Temporal evolution of maximum and minimum tangential stress at deposition hole and deposition tunnel walls for the stress model by Ask et al. (2007) calculated for the centre point of patch B. Note that the lowest spalling strength (CIS) reported is 60 MPa, which is exceeded by the tunnel and hole tangential stress throughout certain stages.

Subsequently the stresses drop according to the imposed temperature scheme. After the thermally induced stresses have declined, the vertical and horizontal stresses increases due to the load from the ice sheet.

The stress regime is reverse during the excavation and thermal phase. During the simulation of the glacial phase by increasing vertical load the stress regime changes from reverse to strike-slip.

Figure 4.20 shows the evolution of stress difference in the repository for the x-y-plane (for deposition holes) along a horizontal scanline through the repository in NW-SE direction. The stress difference is shown for different time steps during the heating phase and reaches peak values after 30 years after deposition of the canisters and this coincides with the thermal peak as described earlier. The largest variation in stress difference is in the volumes between the patches.

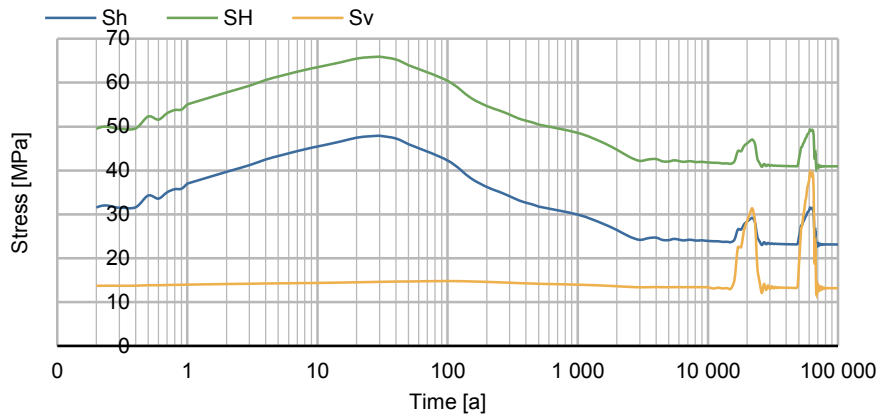


Figure 4.19: Temporal evolution of principal stresses for the stress model by Martin (2007; SKB's most likely) at the centre point of patch B. Increase in vertical stress component is reduced due to the free upper boundary of the model (see text).

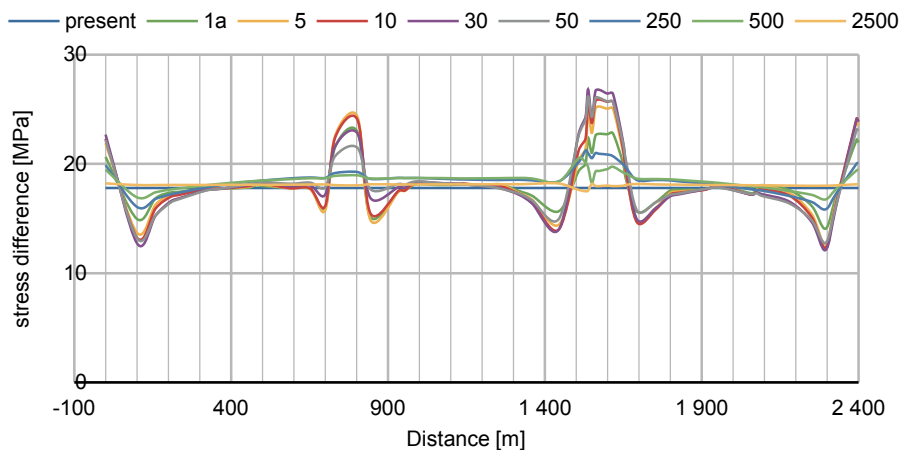


Figure 4.20: Evolution of stress difference for a horizontal cross-section (for deposition holes) vs. distance along the repository for various time steps during the thermal phase. The scanline lies 500 m from the symmetry plane in y-direction.

The evolution of stress difference for the horizontal cross section for the deposition tunnels is given in Figure 4.21. The change in stress difference is largest after 30 years and inside the patches. Between the patches the change in stress difference is smaller.

For the glaciation phase, the change in stress difference is plotted in Figures 4.22 and 4.23. The change in stress difference is negligible for the deposition holes, whereas the deposition tunnels see a pronounced increase in stress difference due to the increase in vertical stress.

Calculating the tangential stress on the deposition tunnels and deposition holes from the simulated stresses and their evolution yields an understanding for the evolution of spalling potential. Figure 4.24 shows the analysis. For the deposition holes the tangential stresses exceed the 0.53UCS threshold during the thermal phase. The deposition tunnels stay below the spalling criterion.

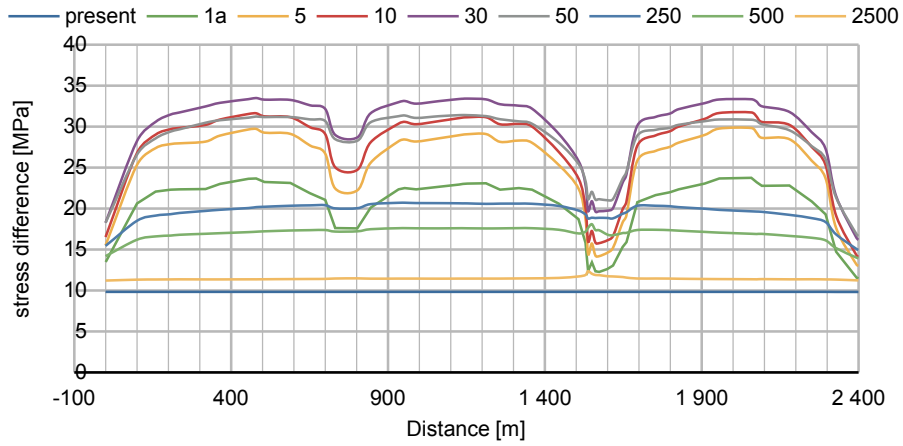


Figure 4.21: Stress difference for vertical cross-section (for deposition tunnels) vs. distance along the repository for various time steps during the heating phase. The scanline lies 500 m from the symmetry plane in y-direction.

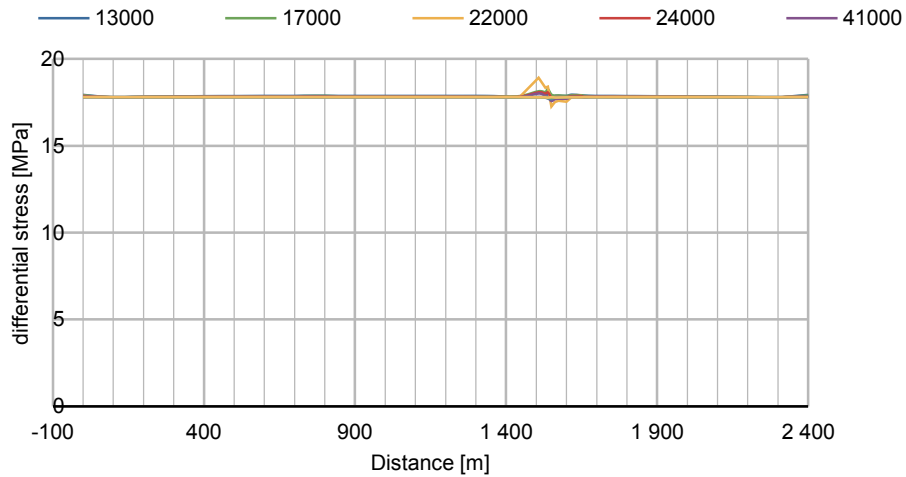


Figure 4.22: Stress difference for horizontal cross section (for deposition holes) vs. distance along the repository for various time steps during the glaciation phase. The scanline lies 500 m from the symmetry plane in y-direction. The small kink at 1.500 m is a mesh artifact.

However, during both the thermal as well as glaciation phase for both the deposition holes and also tunnels the tangential stresses are above the 60 MPa threshold at certain stages, which was the lowest measured spalling stress from crack initiation analysis by SKB.

The minimum tangential stress is positive at all times, indicating that tensile failure of the walls of the deposition tunnels and deposition holes is not to be expected with the base scenario.

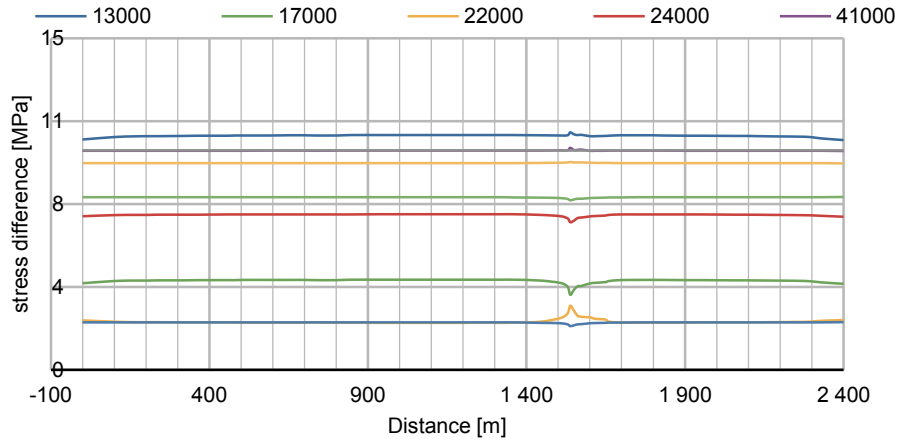


Figure 4.23: Stress difference for vertical cross section (for deposition tunnels) vs. distance along the repository for various time steps during the glaciation phase. The scanline lies 500 m from the symmetry plane in y-direction.

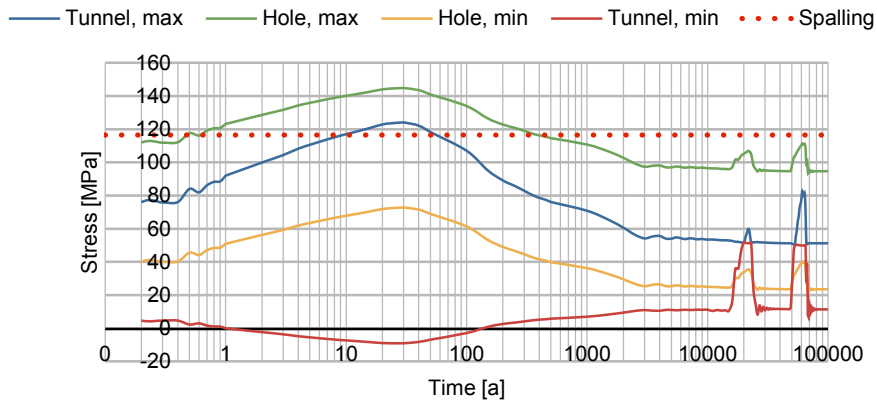


Figure 4.24: Temporal evolution of maximum and minimum tangential stress at deposition hole and deposition tunnel walls for the stress model by Martin (2007) calculated for the centre point of patch B. Note that the lowest spalling strength (CIS) reported is 60 MPa, which is exceeded by the tunnel and hole tangential stress throughout certain stages.

Simulation MISF3

The evolution of stress with the alternative initial stress field model by Geomecon and the base model is given in Figure 4.25 for midpoint patch B where the stress increase appears to be maximum. The stresses rise rapidly after deposition of the canisters due to the thermal heating and reach a maximum after 30 years. Subsequently the stresses drop according to the imposed temperature scheme. By the time the thermally induced stresses have declined, the vertical and horizontal stresses increase due to the load of the ice sheet cover.

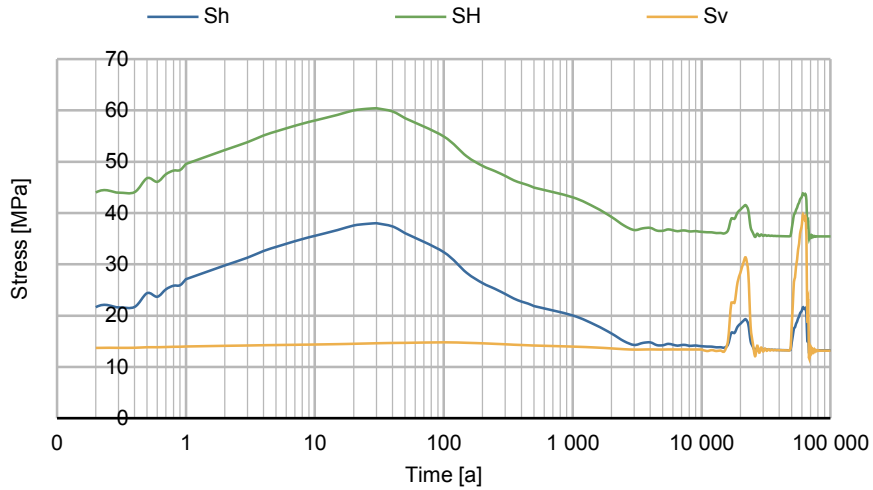


Figure 4.25: Temporal evolution of principal stresses for the alternative stress model by Geomecon at the centre point of patch B. Increase in vertical stress component is reduced due to the free upper boundary of the model (see text).

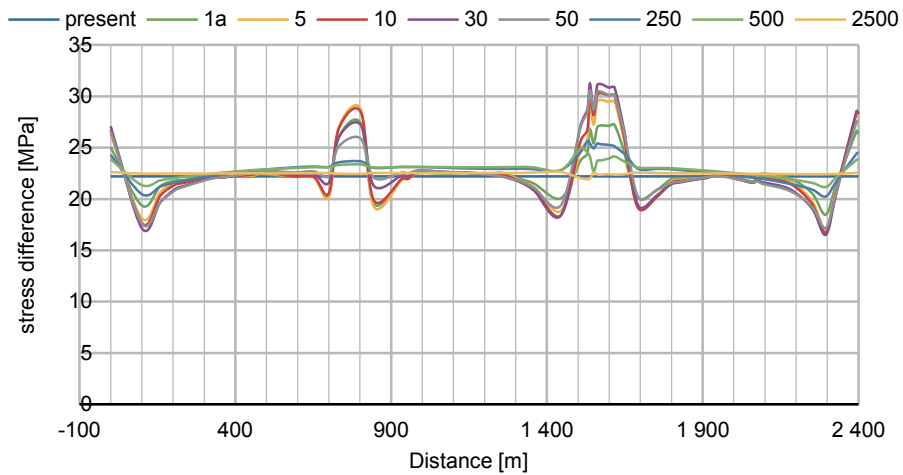


Figure 4.26: Differential stress for a horizontal cross-section (for deposition holes) vs. distance along the repository for various time steps during the heating phase. The scanline lies 500m from the symmetry plane in y-direction.

From initial transpressional conditions, the stress regime becomes reverse during the thermal phase. During the simulation of the glacial phase by increasing vertical load the stress regime changes from transitional to normal faulting.

Figure 4.26 shows the evolution of differential stress in the repository for the x-y-plane (for deposition holes) along a horizontal scanline through the repository in NW-SE direction. The differential stress is shown for different time steps during the heating phase and reaches peak values after 30 years after deposition of the canisters and coincides with the thermal peak as described earlier. The largest variation in stress difference is between the patches.

The evolution of stress difference for the crosscut plane for the deposition tunnels is given in Figure 4.27. The change in stress difference is largest after 30 years and within the patches. Between the patches the change in stress difference is less.

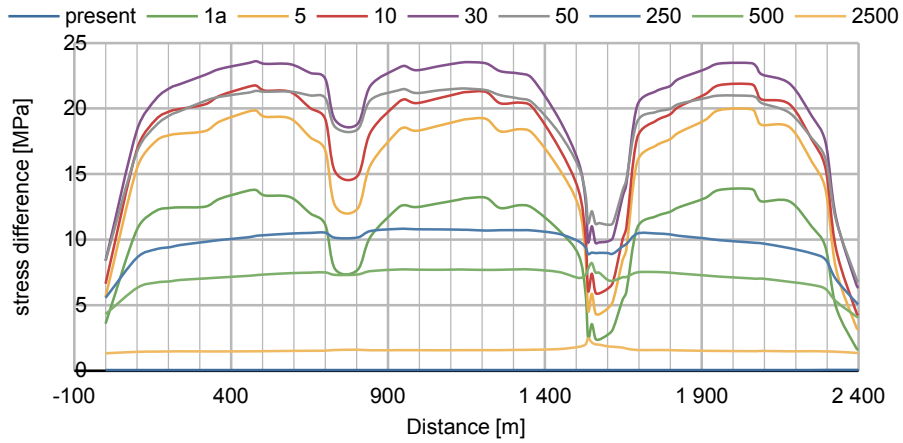


Figure 4.27: Stress difference for vertical cross-section (for deposition tunnels) vs. distance along the repository for various time steps during the heating phase. The scanline lies 500 m from the symmetry plane in y-direction.

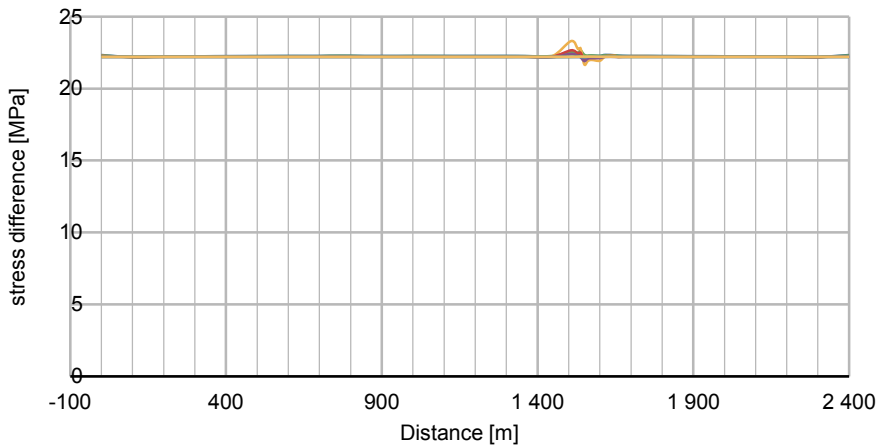


Figure 4.28: Stress difference for horizontal cross section (for deposition holes) vs. distance along the repository for various time steps during the glaciation phase. The scanline lies 500 m from the symmetry plane in y-direction.

For the glaciation phase the change in stress difference is plotted in Figures 4.28 and 4.29. The change in stress difference is negligible for the deposition holes, whereas the deposition tunnels see a pronounced increase in stress difference due to the increase in vertical stress.

Calculating the tangential stress on the deposition tunnels and deposition holes from the simulated stresses and their evolution yields an understanding for the evolution of spalling potential. Figure 4.30 shows the analysis. For the deposition holes the tangential stresses exceed the $0.53 \cdot \text{UCS}$ threshold during the thermal phase. The deposition tunnels stay below the spalling criterion. However, during both the thermal as well as glaciation phase for both the deposition holes and also tunnels the tangential stresses are above the 60 MPa threshold at certain stages, which was the lowest measured spalling stress from crack initiation analysis by SKB.

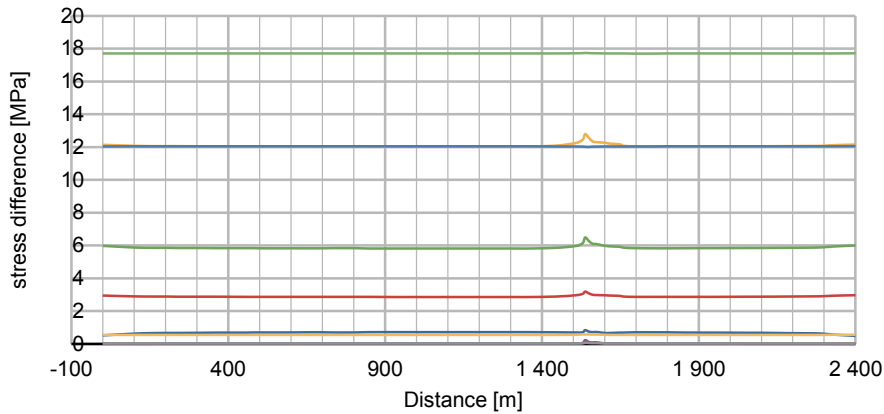


Figure 4.29: Stress difference for vertical cross section (for deposition tunnels) vs. distance along the repository for various time steps during the glaciation phase. The scanline lies 500 m from the symmetry plane in y-direction.

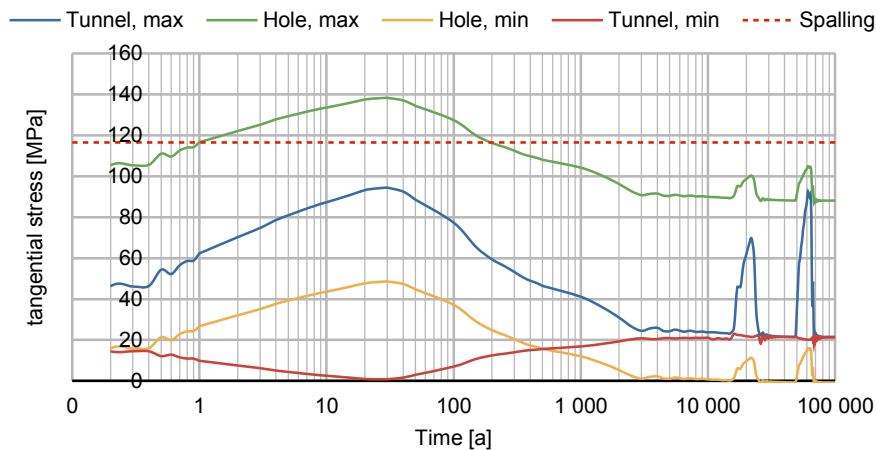


Figure 4.30: Temporal evolution of maximum and minimum tangential stress at deposition hole and deposition tunnel walls for the alternative stress model by Geomecon calculated for the centre point of patch B. Note that the lowest spalling strength (CIS) reported is 60 MPa, which is exceeded by the tunnel and hole tangential stress throughout certain stages.

The minimum tangential stress is positive at all times, indicating that tensile failure of the walls of the deposition tunnels and deposition holes is not to be expected with the base scenario.

4.4. The Consultants' assessment on the numerical simulation of spalling

For none of the initial stress models examined spalling on both deposition holes and tunnels may be excluded at all times. The stresses and their evolution with time exceed the spalling criterion as defined by SKB for SKB's "most likely" stress model at several stages, for the alternative stress model by Geomecon also at some stages, and only for the low stress model by Ask et al. (2007) spalling is not predicted.

However, as spalling starts according to SKB when the tangential stress at the excavation wall exceeds the crack initiation stress, and the lowest reported crack initiation and hence spalling stress is 60 MPa, spalling may not be excluded for any of the stress models. For both the deposition tunnels and holes the tangential stress reaches the 60 MPa threshold during most stages for the SKB model, at certain stages for the alternative stress model by Geomecon, and even for the low stress Ask et al. (2007) model during some stages.

These results from the simulations comply with the general results from the analytical calculations as reported in Chapter 2 of this report.

5. The Consultants' overall assessment on spalling

A good understanding of the in situ stress field is fundamental for any mechanical analysis. Therefore the stress field models presented were revisited. The analysis of the background and the assumptions to SKB's stress field model gave rise to doubts about the robustness of the stress field model.

The issues concerning the presented "most likely" stress model mainly are:

- the selective and inconsistent use of measured field data without consistent presentation of the rationale
- the omission of the hydraulic data without constructive explanation
- the inconsistent use of non-linear stress gradients
- the fact that the stress model presented is not very likely from a geomechanical point of view.

Therefore, an alternative model was developed that takes into account all findings and inconsistencies found while discussing the stress model proposed by SKB. However, it needs to be made clear that the data set for stress is very limited and additional measurements for the site are recommended.

The analysis of the spalling potential was carried out both analytical and numerical and it clearly showed, that the presentation by SKB makes the stability margin of the excavations appear quite positive. Several stress models including the one by SKB and the newly proposed one by Geomecon were considered in the spalling analysis. It became clear that spalling is an issue for the deposition holes already from the excavation phase and becomes severe during the thermal phase. Some hundred deposition holes might be affected by spalling of varying depth during excavation, but about 90% of the deposition holes might be subjected to a certain degree of spalling during the thermal phase.

It needs to be emphasized that the scoping calculations of the spalling potential were based on very limited laboratory data by SKB. The available laboratory data was not reevaluated or reviewed in the context of this study. However, in the light of recent publications (Ghazvinian et al., 2012), the interpretation of the data appears to be unfavorable for SKB's prediction of spalling. While SKB's data on the crack initiation strengths spans about 100 MPa with a mean of about 120 MPa, recent data (Ghazvinian et al., 2012) suggests a mean value of about 100 MPa and spans an interval of 30-50 MPa. It may be suspected that there is an issue with the estimation of CIS in SKB's data and the authors recommend to review the data in detail and probably to complement the database with additional, perhaps independent evidence for the CIS, which is the basis for the spalling analysis for Forsmark.

The spalling criterion itself appears to be suitable for the purpose of estimating the spalling potential. It has been successfully applied in Canada (AECL), and the criterion in itself is also state-of-the-art in borehole stability analysis. However, the spalling strength limit to be used in the analysis might need revisitation, as the critical value of $0.53 \cdot \text{UCS}$ gives the impression of more stable conditions than would be expected from the available laboratory data.

Although SKB's understanding of the initial stress field is poor, their stress model is serving as a conservative approach, as with their stress model spalling is to be expected throughout most phases of the repository future. This has been brought forward by SKB and is initially confirmed by the analyses as carried out in this study. However, as the analysis has been based on glaciation models and thermal heating scenarios as presented by SKB without verifying those simulations, some unfavorable scenarios might be not identified.

However, SKB's proposed stress model is non-conservative regarding the estimation of tensile reactivation of existing fractures or even creation of new excavation-parallel tensile fracture. There is some indication from the analysis in this study that this might be an issue depending on the adopted stress model. Tensile reactivated fractures or newly created fractures have the potential to serve as high permeable pathways for fluids and radionuclides. Therefore the issue of tensile fracture generation needs to receive attention, which has not been done by SKB as far as the consultants are aware.

6. References

- Andersson J.C., 2007. Rock mass response to coupled mechanical thermal loading: Äspö pillar stability experiment. Ph. D. thesis TRITA-JOB PHD 1008. Royal Institute of Technology, Stockholm, Sweden.
- Byerlee J., 1978. Friction of rocks. *Pure and Applied Geophysics*, 116: 615-626.
- Cornet F.H., 1993. The HTPF and the integrated stress determination methods. In: *Comprehensive Rock Engineering*, 3, (J. Hudson, Ed.). Pergamon Press, Oxford, UK, pp. 413–32.
- Diedrich M., 2007. Mechanistic interpretation and practical application of damage and spalling prediction criteria for deep tunnelling. The 2003 Canadian Geotechnical Colloquium. *Can. Geotech. J.* 44: 1082 - 1116.
- Ghazvinian E., Perras M., Diederichs M., Labrie D., 2012. Formalized approaches to defining damage thresholds in brittle rock; Granite and Limestone. 46th US Rock Mechanics/Geomechanics Symposium (Bobet, A. ed.), June 2012, Chicago, Illinois, Curran Associates, Inc., USA.
- Hakala M., Hudson J.A., Christiansson R., 2003. Quality control of overcoring stress measurement data. *Int. J. Rock Mech. Min. Sci.* 40, No. 7–8, pp. 1141–1159.
- Hakala M., 2006. Quality control for overcoring stress measurement data. Posiva Report 2006-03, Posiva Oy, Finland.
- Heidbach O., Tingay M., Barth A., Reinecker J., Kurfeß D., Müller B., 2008. The World Stress Map database release 2008, doi:10.1594/GFZ.WSM.Rel2008.
- Ingevald K., Strindell L., 1981. Mätning av bergspänningar (bergtryck) i djupa vertikala borrhål. Statens Vattenfallsverk, rapport L-543:2 (in Swedish).
- Jaeger J.C., Cook N.G.W., Zimmermann R.W., 2007. *Fundamentals of Rock Mechanics*, 4th ed., Blackwell Publishing, Oxford, UK.
- Martin C.D., Christiansson R., 2009. Estimating the potential spalling around a deep nuclear waste repository in crystalline rock. *Int. J. Rock Mech. Min. Sci.* 46(2), 219-228.
- Peška P., Zoback M.D., 1995. Compressive and tensile failure of inclined well bores and determination of in-situ stress and rock strength. *Journal of Geophysical Research*, 100, 12, 791-12, 811.
- SKB AR 88-54. Bjarnason B., Stephansson O., 1988. Hydraulic fracturing stress measurements in borehole Fi-6 Finnsjön study site, central Sweden. Swedish Nuclear Fuel and Waste Management Co (SKB).
- SKB P-03-119. Perman F., Sjöberg J., 2003. Transient strain analysis of overcoring measurements in boreholes DBT-1 and DBT-3. Swedish Nuclear Fuel and Waste Management Co (SKB).

SKB P-04-83. Sjöberg J., 2004. Overcoring rock stress measurements in borehole KFM01B. Swedish Nuclear Fuel and Waste Management Co (SKB).

SKB P-04-311. Klee G., Rummel F., 2004. Forsmark site investigation – rock stress measurements with hydraulic fracturing and hydraulic testing of pre-existing fractures in borehole KFM01A, KFM01B, KFM02A and KFM04A results of in-situ tests. Swedish Nuclear Fuel and Waste Management Co (SKB).

SKB P-04-312. Rummel F., Weber U., 2004. Rock stress measurements with hydraulic fracturing and hydraulic testing of pre-existing fractures in borehole KFM01A, KFM01B, KFM02A and KFM04A. Swedish Nuclear Fuel and Waste Management Co (SKB).

SKB P-05-66. Lindfors U., Perman F., Sjöberg J., 2005. Forsmark site investigation: Evaluation of the over-coring results from borehole KFM01B. Swedish Nuclear Fuel and Waste Management Co (SKB).

SKB P-06-93. Lindfors U., 2007. Forsmark site investigation, Overcoring rock stress measurements in borehole KFM07B. Swedish Nuclear Fuel and Waste Management Co (SKB).

SKB P-07-130. Lindfors U., Perman F., Ask M., 2007. Forsmark site investigation, Overcoring rock stress measurements in borehole KFM07C. Swedish Nuclear Fuel and Waste Management Co (SKB).

SKB P-07-205. Lindfors U., Berg S., Perman F., 2007. Forsmark site investigation, Overcoring rock stress measurements in borehole KFM02B. Swedish Nuclear Fuel and Waste Management Co (SKB).

SKB P-07-206. Ask D., Cornet F., Brunet C., Fontbonne F., 2007. Forsmark site investigation. Stress measurements with hydraulic methods in boreholes KFM07A, KFM07C, KFM08A, KFM09A and KFM09B. Swedish Nuclear Fuel and Waste Management Co (SKB).

SKB P-07-234. Ask D., 2007. Forsmark site investigation. Stress measurements with hydraulic methods in boreholes KFM07A, KFM07C, KFM08A, KFM09A and KFM09B. Swedish Nuclear Fuel and Waste Management Co (SKB).

SKB R-05-18. 2005. Forsmark Site Description Model v1.2. Swedish Nuclear Fuel and Waste Management Co (SKB).

SKB R-05-35. Sjöberg J., Lindfors U., Perman F., Ask D., 2005. Evaluation of the state of stress at the Forsmark site. Preliminary site investigation Forsmark area – version 1.2. Swedish Nuclear Fuel and Waste Management Co (SKB).

SKB R-05-71. Martin C.D., 2005. Preliminary assessment of potential underground stability (wedge and spalling) at Forsmark, Simpevarp and Laxemar sites. Swedish Nuclear Fuel and Waste Management Co (SKB).

SKB R-05-59. Mas Ivars D., Hakami H., 2005. Effect of a sub-horizontal fracture zone and rock mass heterogeneity on the stress field in Forsmark area – A numerical study using 3DEC Preliminary site description Forsmark area – version 1.2. Swedish Nuclear Fuel and Waste Management Co (SKB).

SKB R-06-89. Fälth B., Hökmark H., 2007. Mechanical and thermo-mechanical discrete fracture near-field analyses based on preliminary data from the Forsmark,

Simpevarp and Laxemar sites. Swedish Nuclear Fuel and Waste Management Co (SKB).

SKB R-07-26. Martin C.D., 2007. Quantifying in situ stress magnitudes and orientations for Forsmark Design Step D2. Swedish Nuclear Fuel and Waste Management Co (SKB).

SKB R-07-31. Glamheden R., Fredriksson A., Röshoff K., Karlsson J., Hakami H., Christiansson R., 2007. Rock mechanics Forsmark. Site descriptive modelling Forsmark stage 2.2. Swedish Nuclear Fuel and Waste Management Co (SKB).

SKB R-07-45. Stephens M.B., Fox A., La Pointe P., Simeonov A., Isaksson H., Hermanson J., Öhman J., 2007. Geology Forsmark. Site descriptive modelling Forsmark stage 2.2. Swedish Nuclear Fuel and Waste Management Co (SKB).

SKB R-08-65. Sundberg J., Wrafter J., Ländell M., 2008. Thermal properties Forsmark Modelling stage 2.3. Complementary analysis and verification of the thermal bedrock model, stage 2.2. Swedish Nuclear Fuel and Waste Management Co (SKB).

SKB R-08-83. 2009. Site Engineering Report Forsmark, Guideline for underground design, Step D2. November 2009. Swedish Nuclear Fuel and Waste Management Co (SKB).

SKB R-08-115. Eriksson M., Petersson J., Danielsson P., Leander M., 2009. Underground design Forsmark Layout D2, Rock mechanics and rock support. Swedish Nuclear Fuel and Waste Management Co (SKB).

SKB R-08-116. 2009. Underground design Forsmark Layout D2, Swedish Nuclear Fuel and Waste Management Co (SKB).

SKB R-09-04. Hökmark H., Lönnqvist M., Kristensson O., Sundberg J., Hellström G., 2009. Strategy for thermal dimensioning of the final repository for spent nuclear fuel. Swedish Nuclear Fuel and Waste Management Co (SKB).

SKB TR-06-23. Näslund J.-O., 2006. Ice sheet dynamics, in climate and climate related issues for the safety assessment SR-Can. Swedish Nuclear Fuel and Waste Management Co (SKB).

SKB TR-08-05. 2008. Site description of Forsmark at completion of the site investigation phase. SDM-Site Forsmark. Swedish Nuclear Fuel and Waste Management Co (SKB).

SKB TR-09-15. Lund B., Schmidt P., Hieronymus C., 2009. Stress evolution and fault stability during the Weichselian glacial cycle. Swedish Nuclear Fuel and Waste Management Co (SKB).

SKB TR-10-23. Hökmark H., Lönnqvist M., Fälth B., 2010. THM-issues in repository rock. Thermal, mechanical, thermo-mechanical and hydromechanical evolution of the rock at the Forsmark and Laxemar sites. Swedish Nuclear Fuel and Waste Management Co (SKB).

SKB TR-10-37. Glamheden R., Fälth B., Jacobsson L., Harrström J., Berglund J., Bergkvist L., 2010. Counterforce applied to prevent spalling. Swedish Nuclear Fuel and Waste Management Co (SKB).

SKB TR-10-52. 2010. Data report for the safety assessment SR-Site. Swedish Nuclear Fuel and Waste Management Co (SKB).

SKB TR-11-01. 2011. Long-term safety for the final repository for spent nuclear fuel at Forsmark. Main report of the SR-Site project. Swedish Nuclear Fuel and Waste Management Co (SKB).

SSPB, 1982. Characterization of Deep-Seated Rock Masses by Means of Borehole Investigations. In-Situ Rock Stress Measurements, Hydraulic Testing and Core-Logging. Final Report, April 1982, Research and Development Report 5:1. The Swedish State Power Board (SSPB).

Stephansson O., Ångman P., 1986. Hydraulic Fracturing Stress Measurements at Forsmark and Stidsvig, Sweden. Geological Society of Finland, Bulletin, 58, 1, 307-333.

Stephansson O., Ljunggren C., Jing L., 1991. Stress measurements and tectonic implications for Fennoscandia. Tectonophysics, 189, pp 317–322.

Zoback M.D., Moos D., Mastin L., Anderson R.N., 1985. Wellbore breakouts and in situ stress. Journal of Geophysical Research: Solid Earth, JGR 90, Issue B7, 5523-5530.

Zoback M.D., 2007. Reservoir Geomechanics. Cambridge University Press, Cambridge, UK, p. 461.

Coverage of SKB reports

Table A1.1: Reports covered in the assignment.

Reviewed report	Reviewed sections	Comments
SKB R-08-116, Underground design Forsmark, Layout D2	3.1 - 3.6	
SKB TR-11-01 SR-Site	S1-S5, 4.3, 4.4, 4.5, 4.6, 10.2.2, 10.3.5, 10.4.4, 15.5.12	
SKB R-08-83 Site Engineering Report	2.1 - 2.4, 2.7, 8.1 - 8.4	
SKB TR-10-23 T-H-M issues in repository rock	4.1- 4.6, 4.8, 9,	Figure 4-12 probably corresponds to Model MT 9 from Lund et al. (2009), some inconsistency between density of the rock, e.g. Table 4-5, and vertical stress gradients.
SKB TR-10-37 Counterforce to prevent spalling	9.5, 10, 11	
SKB R-09-04 Strategy for thermal dimensioning of the repository	1.1.3, 4, 8.1, 8.2 ,Appendix E	
SKB R-06-94 Creep in jointed rock masses	3, 4, 5, 6	
SKB R-05-35, Evaluation of the state of stress at the Forsmark site. Preliminary site investigation Forsmark area – version 1.2.	3, 4, 5, 6,	
SKB TR-10-52, Data report for the safety assessment SR-Site	6.2, 6.3, 6.4, 6.5	
SKB TR-08-05, Site description of Forsmark at completion of the site investigation phase – SDM-Site Forsmark	2.2.2, 2.3, 6, 7, 11.3, 11.4	

Reviewed report	Reviewed sections	Comments
SKB P-07-206, Forsmark site investigation. Stress measurements with hydraulic methods in boreholes KFM07A, KFM07C, KFM08A, KFM09A and KFM09B.	5.3, 5.4, 6, 7, 8	
SKB R-06-89, Mechanical and thermo-mechanical discrete fracture near-field analyses based on preliminary data from the Forsmark, Simpevarp and Laxemar sites	relevant sections for Forsmark in 5, 6, 7	
SKB R-08-65, Thermal properties Forsmark Modelling stage 2.3. Complementary analysis and verification of the thermal bedrock model, stage 2.2.	7, 8, 9	
SKB TR-09-15, Stress evolution and fault stability during the Weichselian glacial cycle.	complete report	
SKB R-07-26, Quantifying in situ stress magnitudes and orientations for Forsmark Design Step D2.	complete report	
SKB P-03-119, Transient strain analysis of overcoring measurements in boreholes DBT-1 and DBT-3	complete report	
SKB P-04-83, Overcoring rock stress measurements in borehole KFM01B	complete report	
SKB P-04-311, Rock stress measurements with hydraulic fracturing and hydraulic testing of pre-existing fractures in borehole KFM01A, KFM01B, KFM02A and KFM04A	complete report	
Results of in-situ tests		
SKB P-04-312, Rock stress measurements with hydraulic fracturing and hydraulic testing of pre-existing fractures in borehole KFM01A, KFM01B, KFM02A and KFM04A	5, 6	

Reviewed report	Reviewed sections	Comments
Laboratory Core Investigations		
SKB P-05-66, Evaluation of the overcoring results from borehole KFM01B	complete report	
SKB P-06-93, Overcoring rock stress measurements in borehole KFM07B	complete report	
SKB P-07-130, Overcoring rock stress measurements in borehole KFM07C	complete report	
SKB P-07-205, Overcoring rock stress measurements in borehole KFM02B	complete report	
SKB P-07-234, Evaluation of overcoring stress measurements in boreholes KFM01B, DBT-1 and DBT-3 and hydraulic stress measurements in boreholes KFM01A, KFM01B, KFM02A and KFM04A at the Forsmark site	complete report	

Results from analytical spalling analyses

Spalling in deposition holes

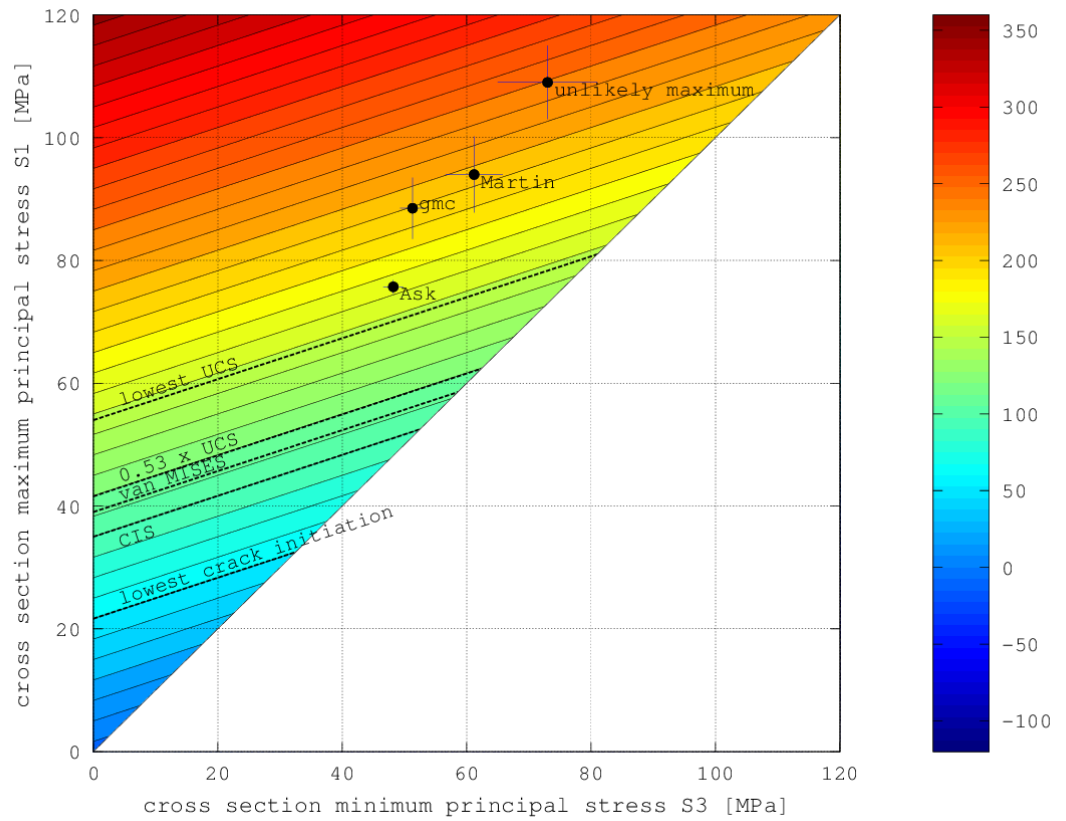


Figure A2.1. Spalling potential diagram for deposition holes during glaciation (model scenario #6). The colour code depicts tangential stress in [MPa].

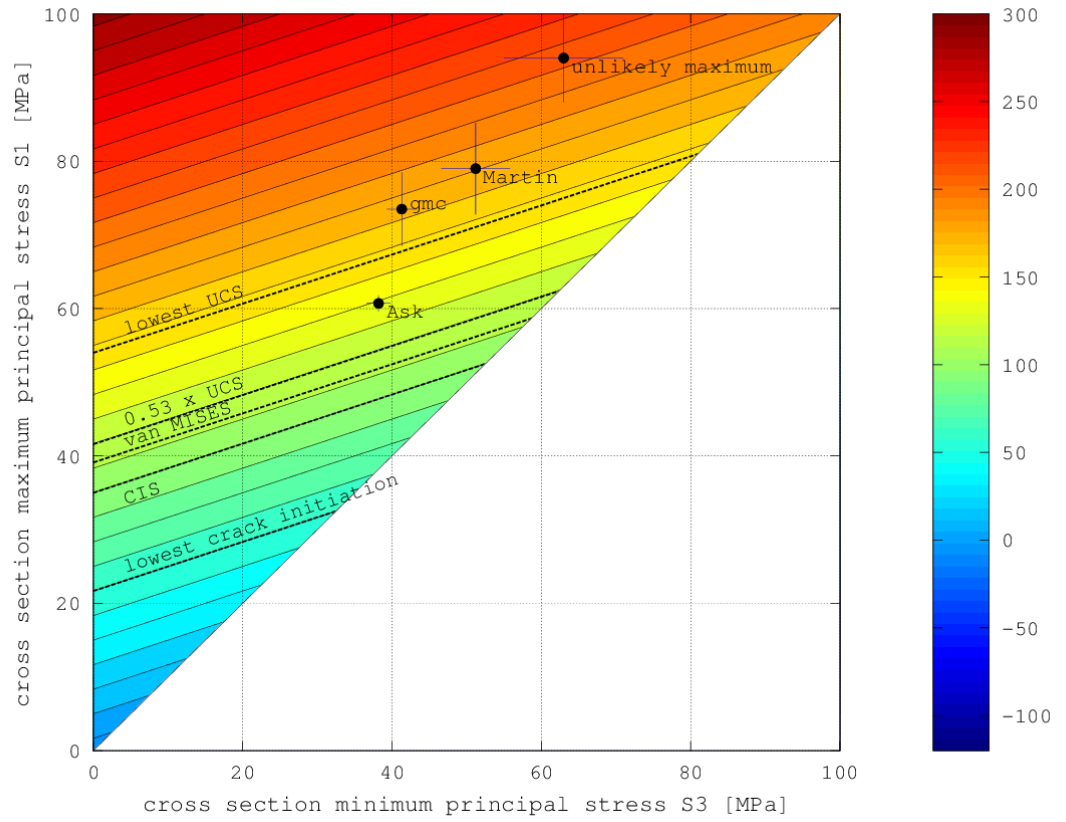


Figure A2.2. Spalling potential diagram for deposition holes during glaciation (model scenario #7). The colour code depicts tangential stress in [MPa].

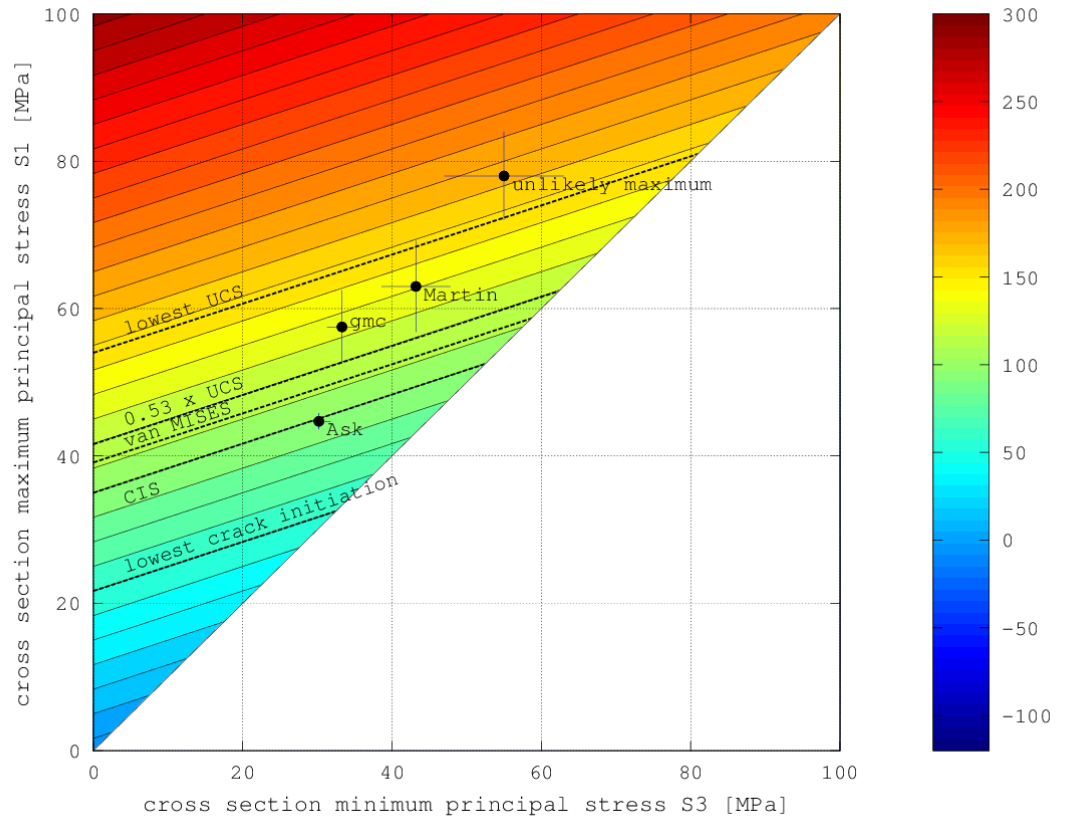


Figure A2.3. Spalling potential diagram for deposition holes during glaciation (model scenario #8). The colour code depicts tangential stress in [MPa].

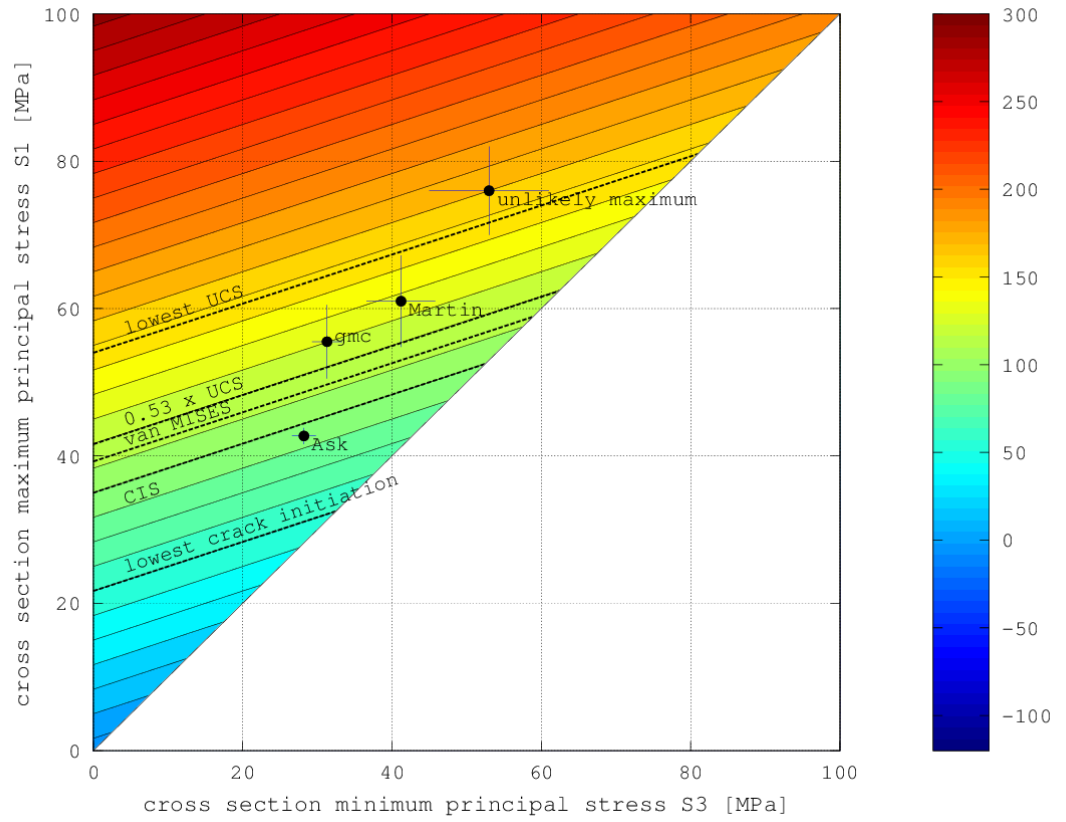


Figure A2.4. Spalling potential diagram for deposition holes during glaciation (model scenario #9). The colour code depicts tangential stress in [MPa].

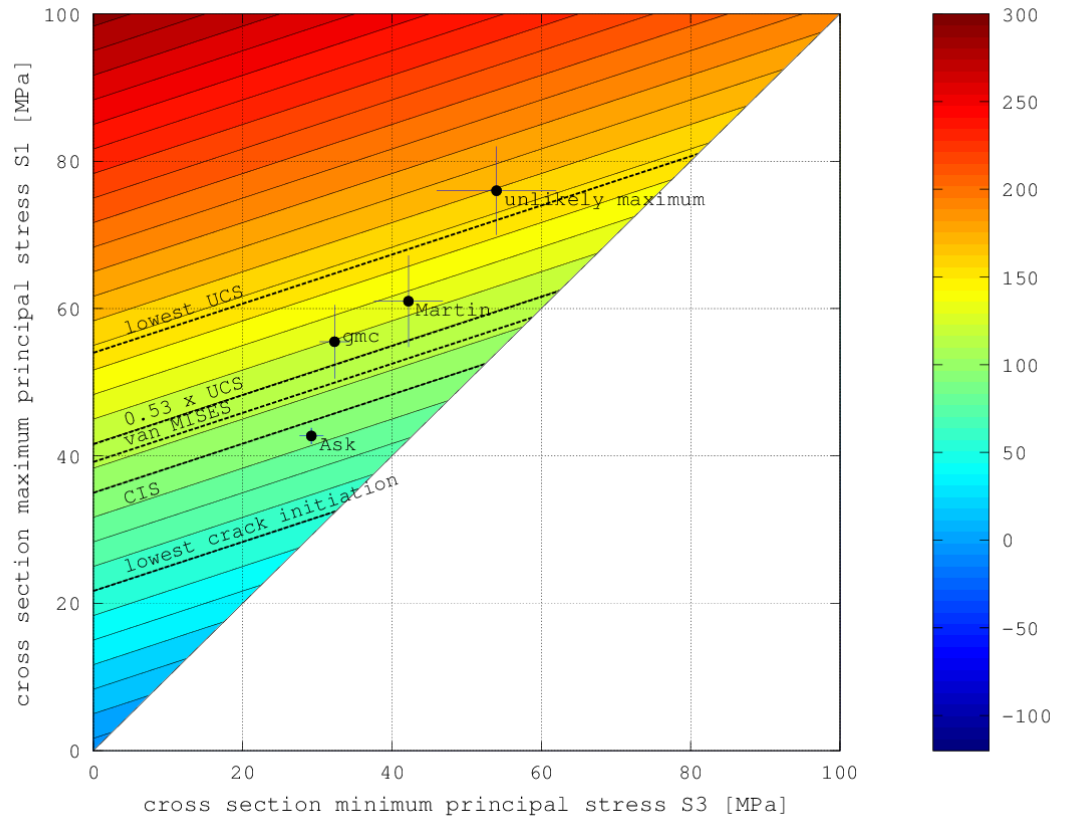


Figure A2.5. Spalling potential diagram for deposition holes during glaciation (model scenario #10). The colour code depicts tangential stress in [MPa].

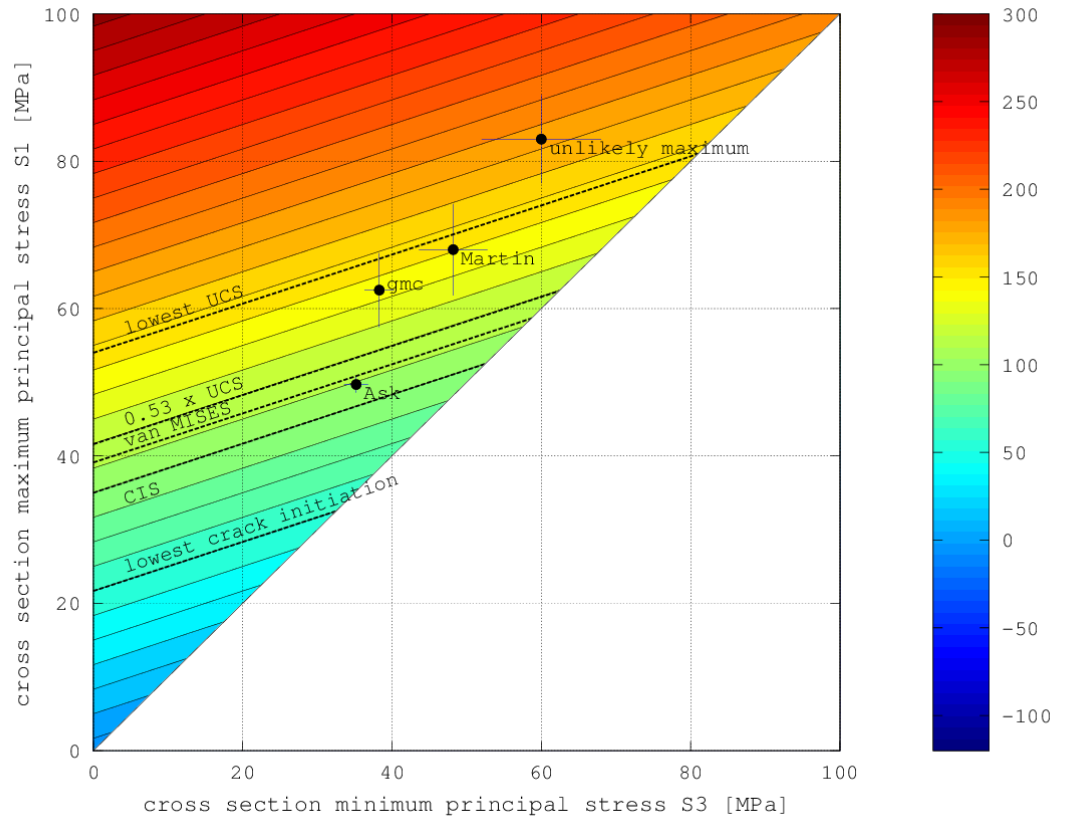


Figure A2.6. Spalling potential diagram for deposition holes during glaciation (model scenario #11). The colour code depicts tangential stress in [MPa].

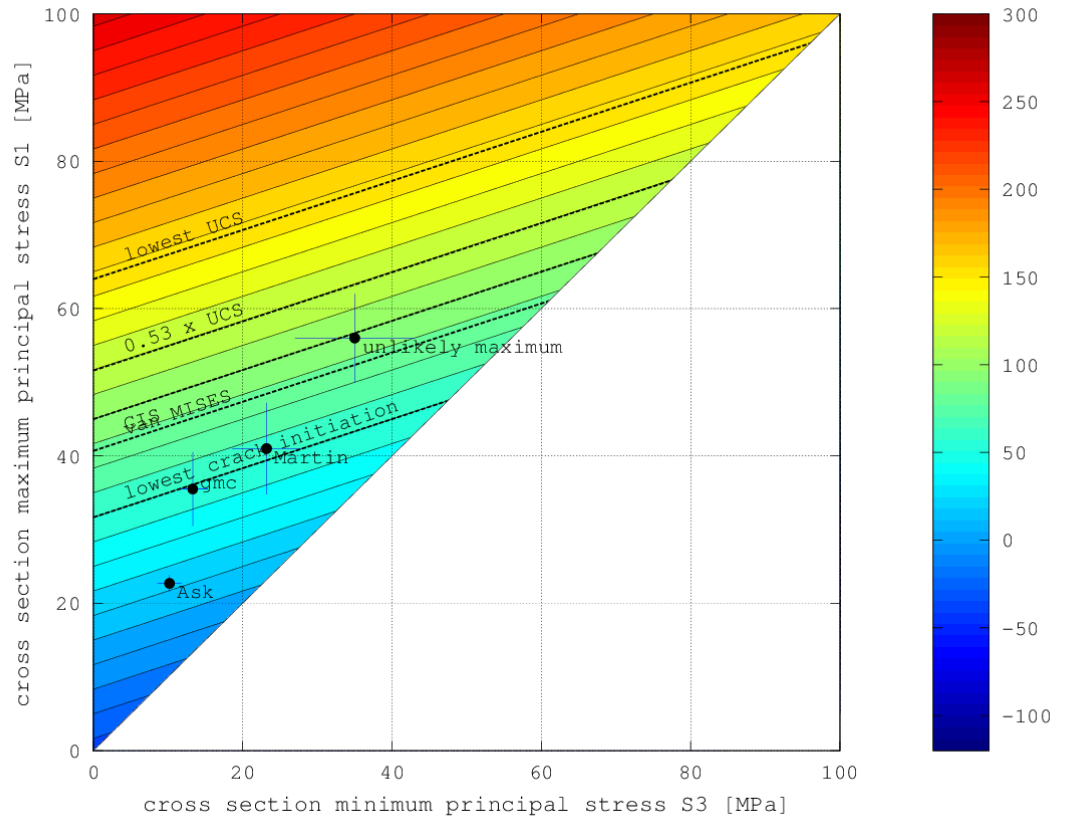


Figure A2.7. Spalling potential diagram for deposition holes during glaciation (model scenario #12). The colour code depicts tangential stress in [MPa].

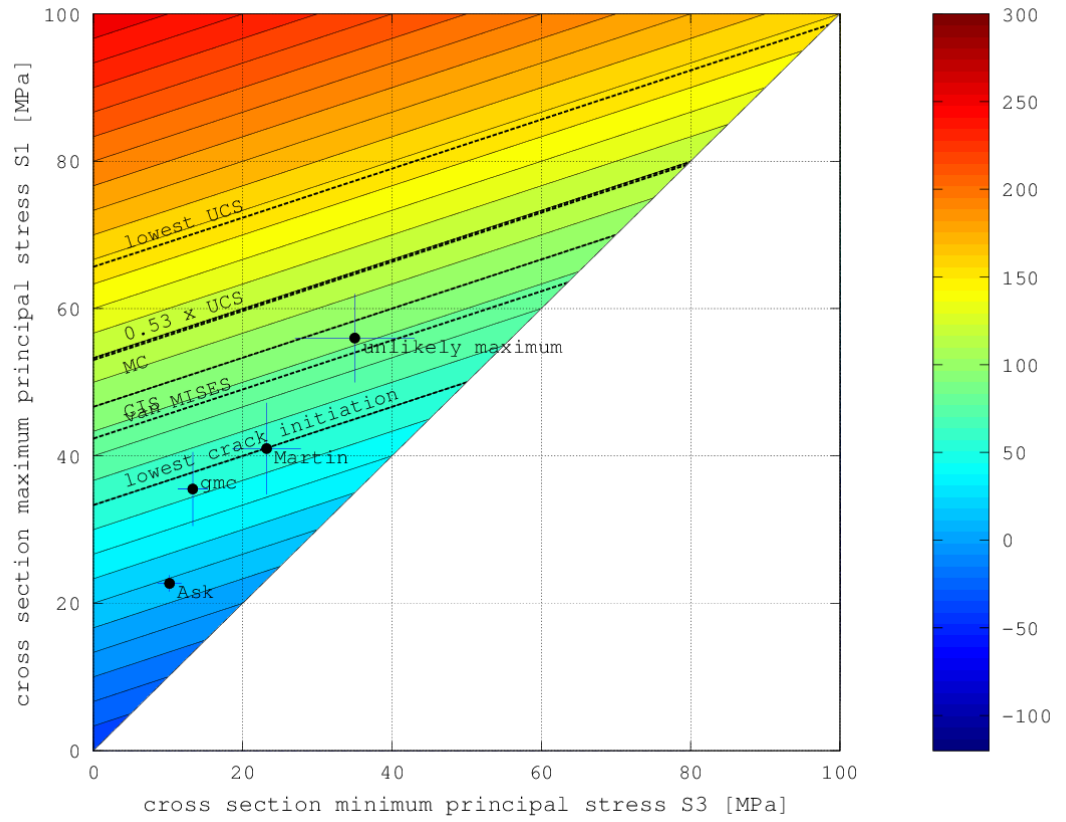


Figure A2.8. Spalling potential diagram for deposition holes during glaciation (model scenario #13). The colour code depicts tangential stress in [MPa].

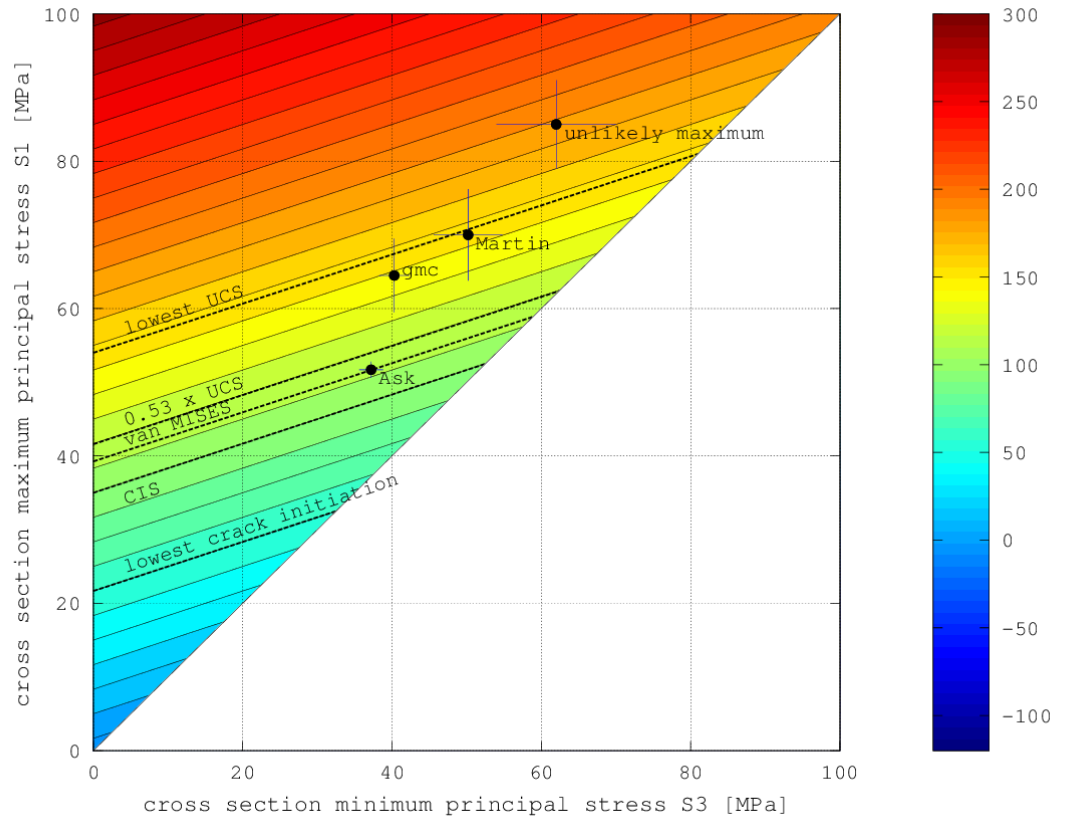


Figure A2.9. Spalling potential diagram for deposition holes during glaciation (model scenario #14). The colour code depicts tangential stress in [MPa].

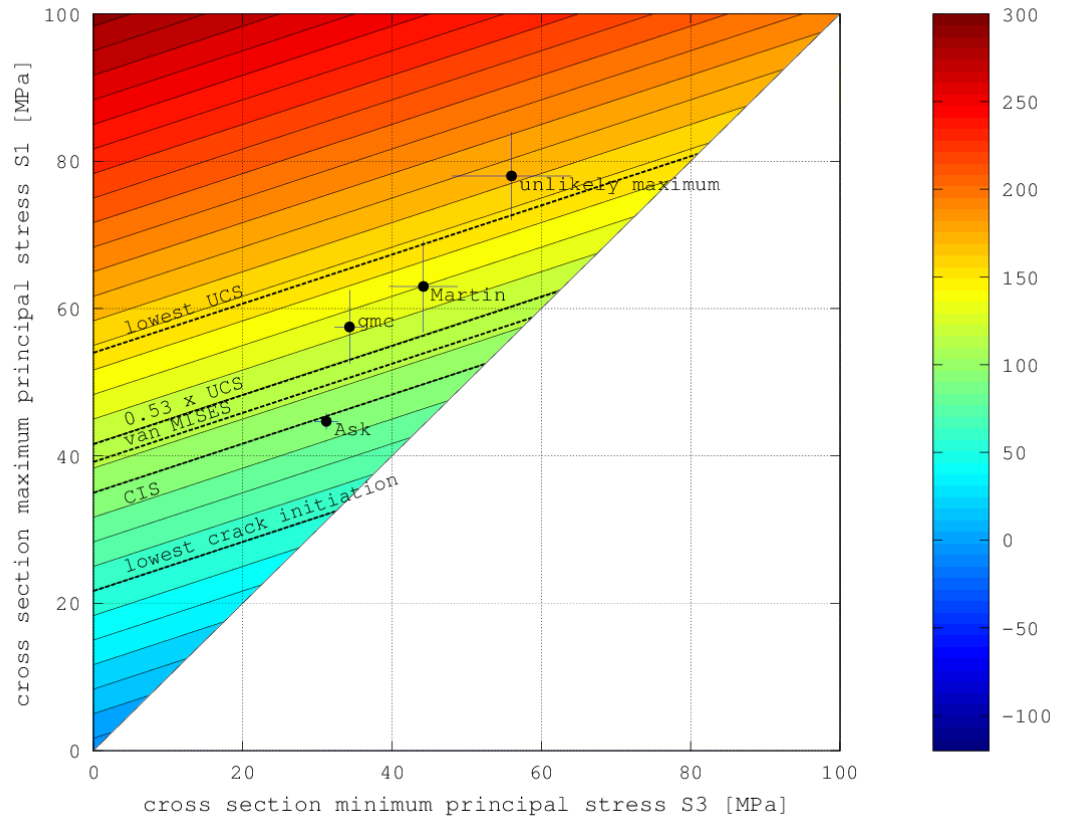


Figure A2.10. Spalling potential diagram for deposition holes during glaciation (model scenario #15). The colour code depicts tangential stress in [MPa].

Spalling in deposition tunnels

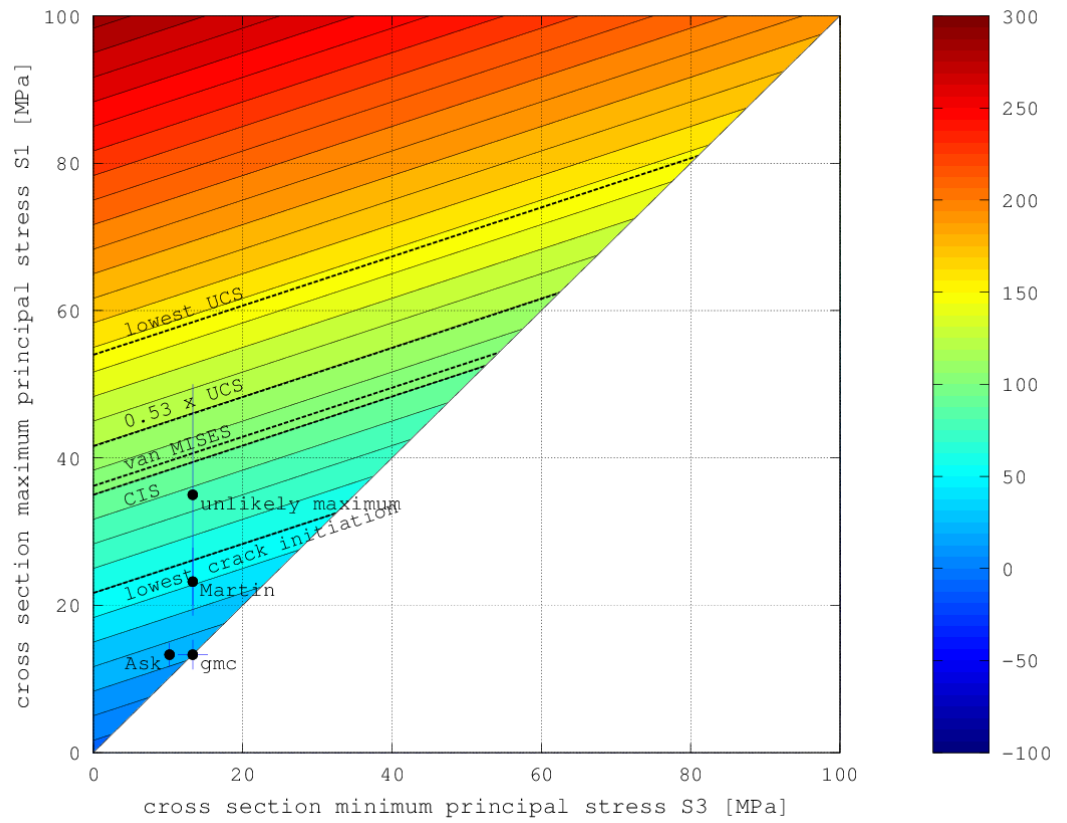


Figure A2.11. Spalling potential diagram for deposition tunnels model scenario #1. The colour code depicts tangential stress in [MPa].

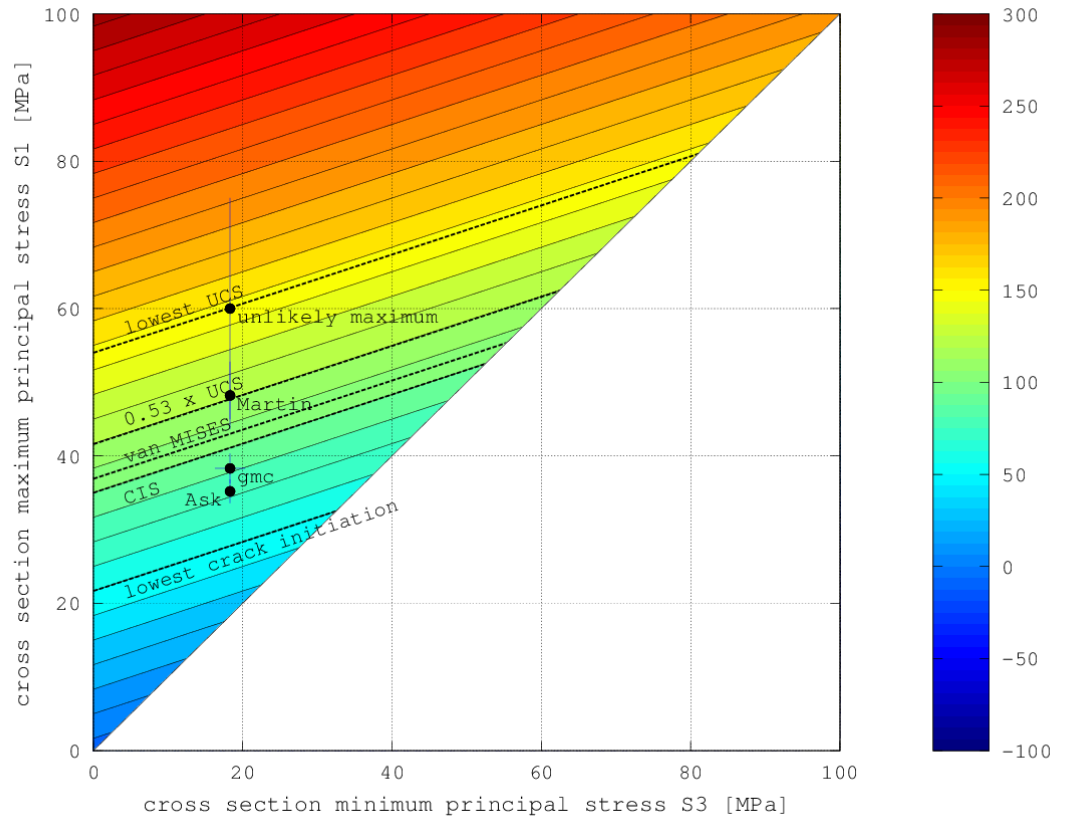


Figure A2.12. Spalling potential diagram for deposition tunnels model scenario #2. The colour code depicts tangential stress in [MPa].

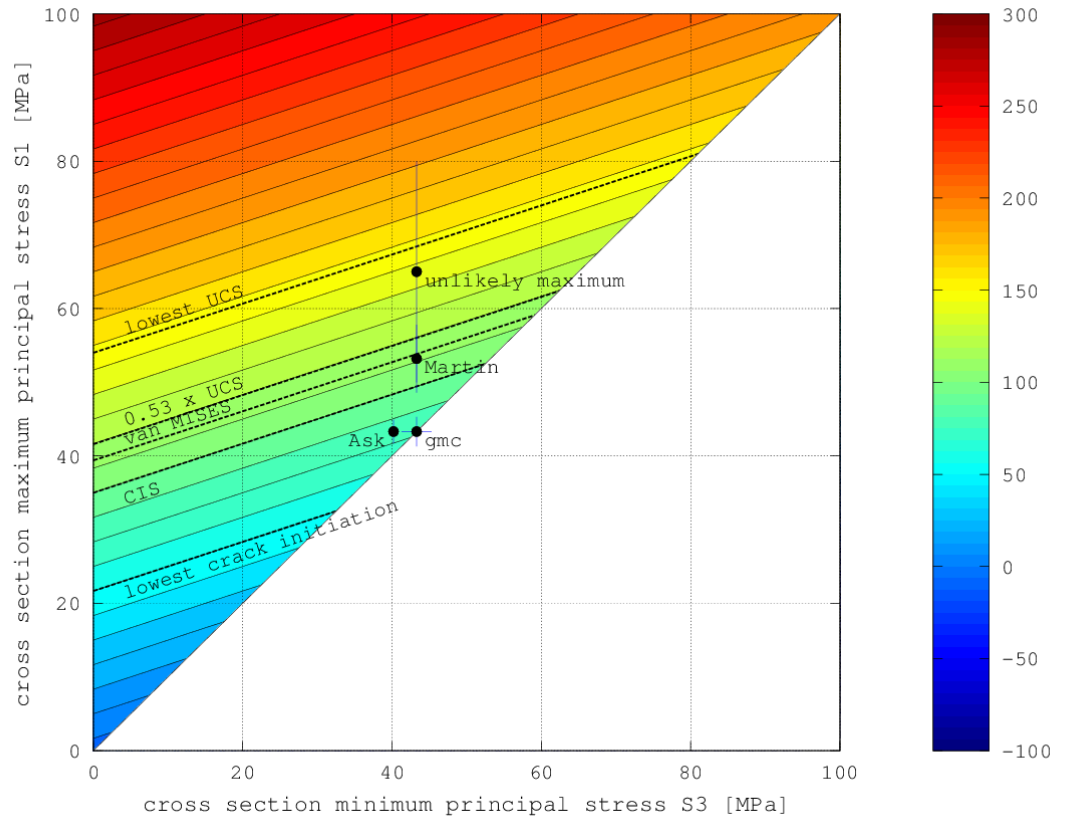


Figure A2.13. Spalling potential diagram for deposition tunnels model scenario #3. The colour code depicts tangential stress in [MPa].

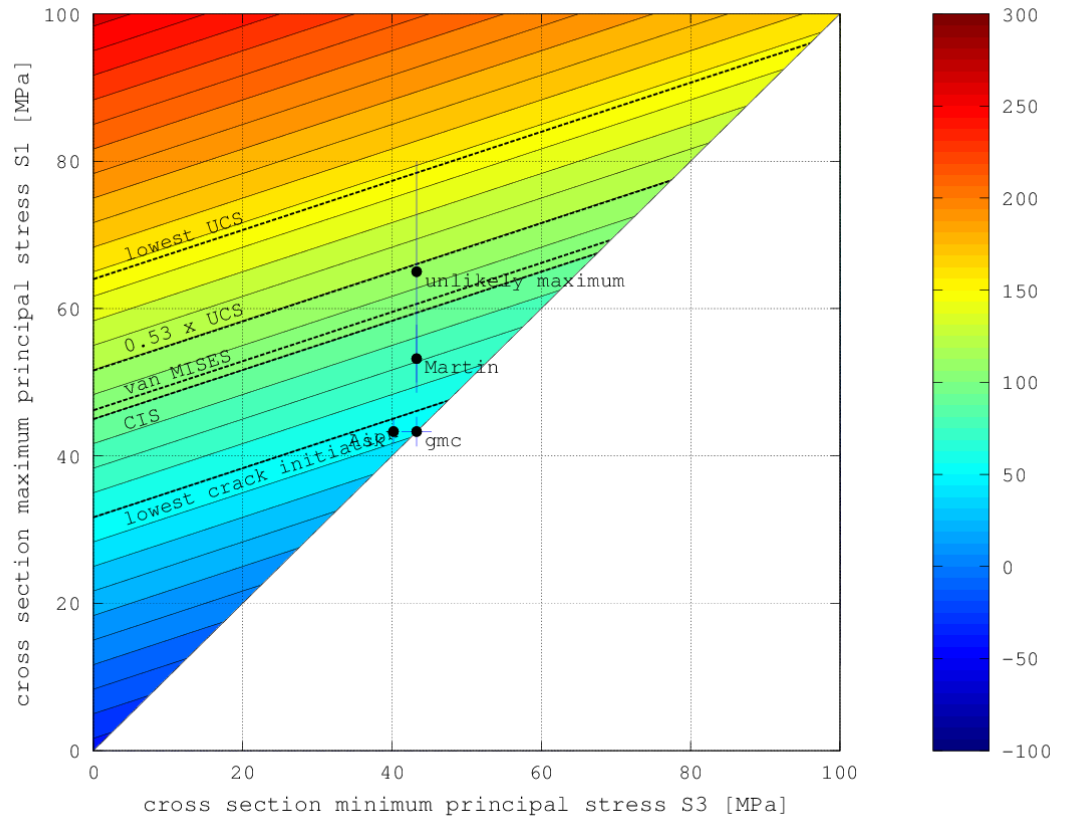


Figure A2.14. Spalling potential diagram for deposition tunnels model scenario #4. The colour code depicts tangential stress in [MPa].

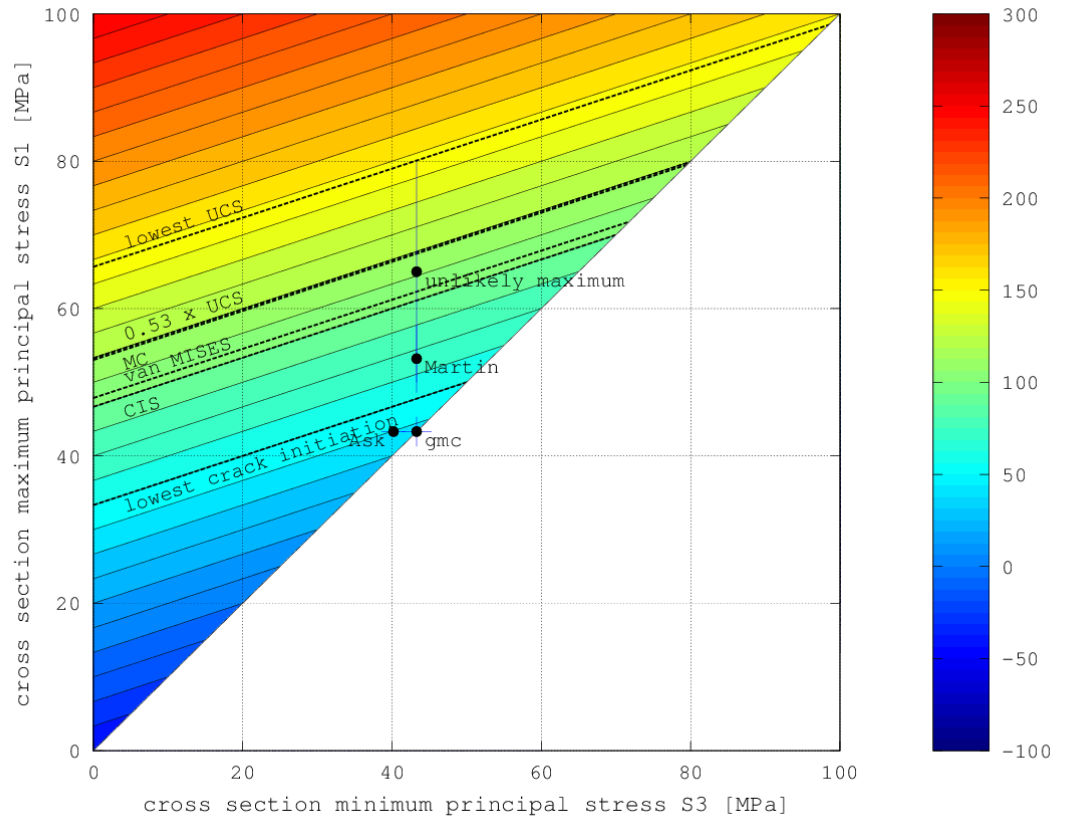


Figure A2.15. Spalling potential diagram for deposition tunnels model scenario #5. The colour code depicts tangential stress in [MPa].

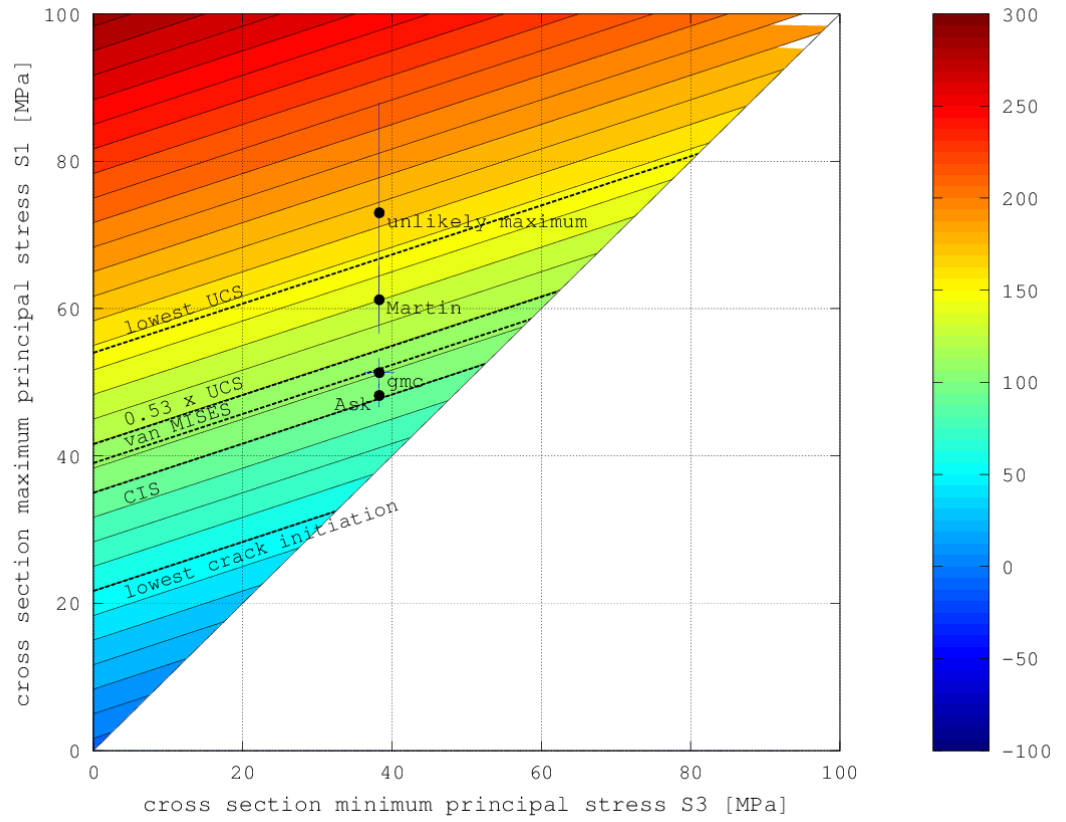


Figure A2.16. Spalling potential diagram for deposition tunnels model scenario #6. The colour code depicts tangential stress in [MPa].

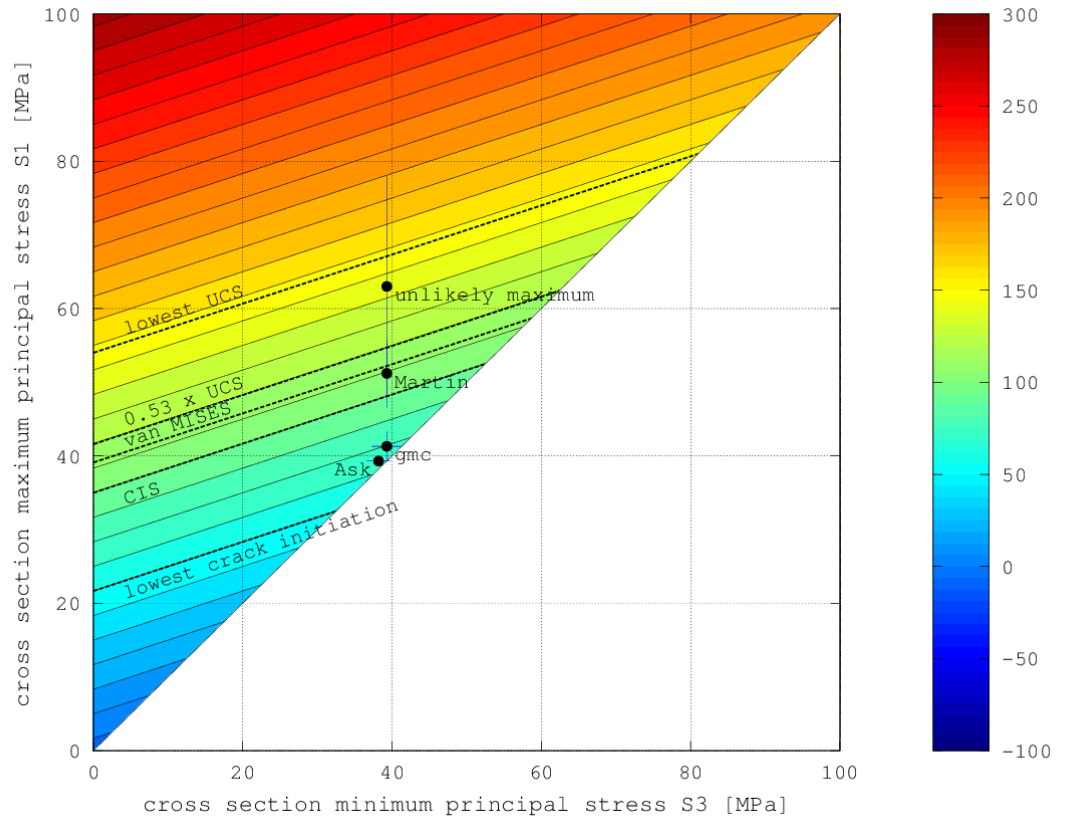


Figure A2.17. Spalling potential diagram for deposition tunnels model scenario #7. The colour code depicts tangential stress in [MPa].

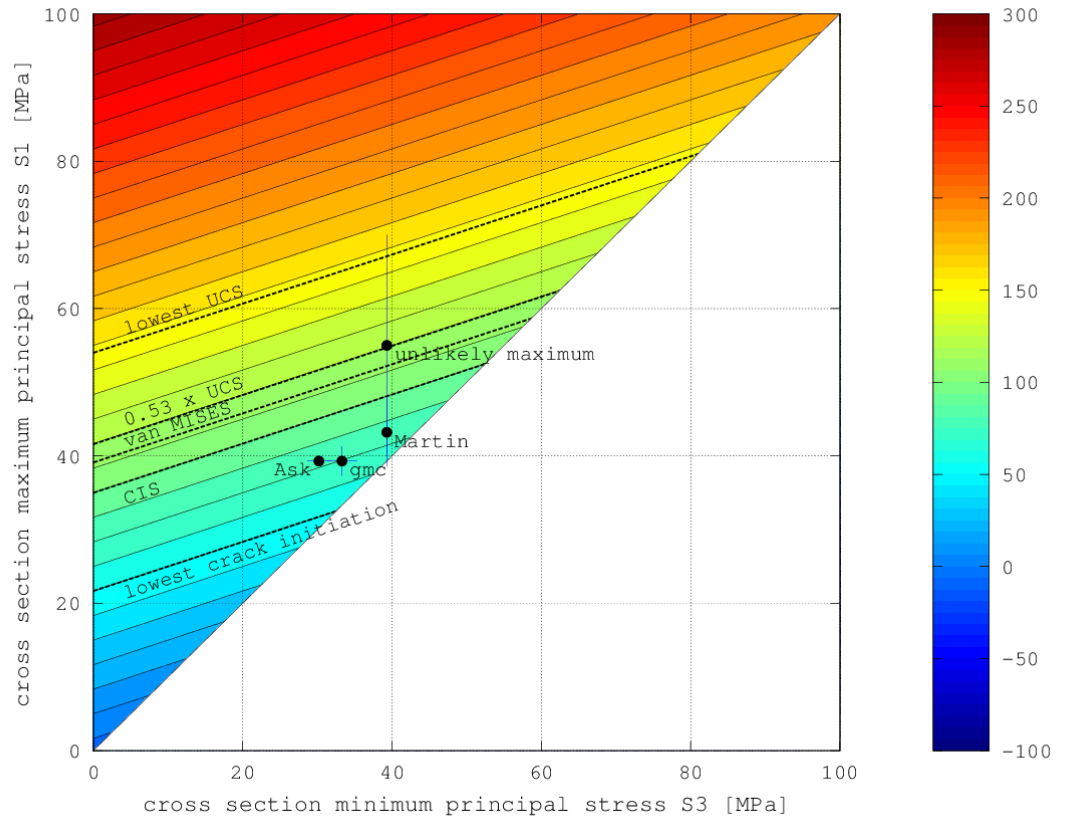


Figure A2.18. Spalling potential diagram for deposition tunnels model scenario #8. The colour code depicts tangential stress in [MPa].

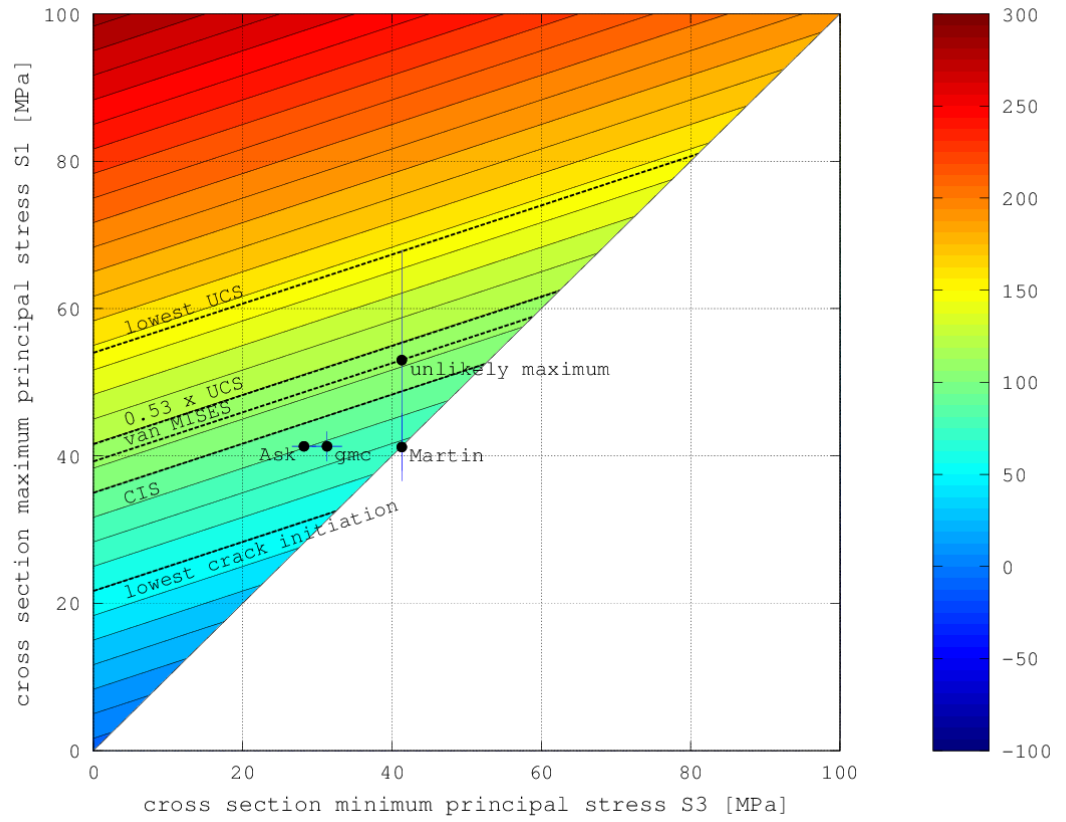


Figure A2.19. Spalling potential diagram for deposition tunnels model scenario #9. The colour code depicts tangential stress in [MPa].

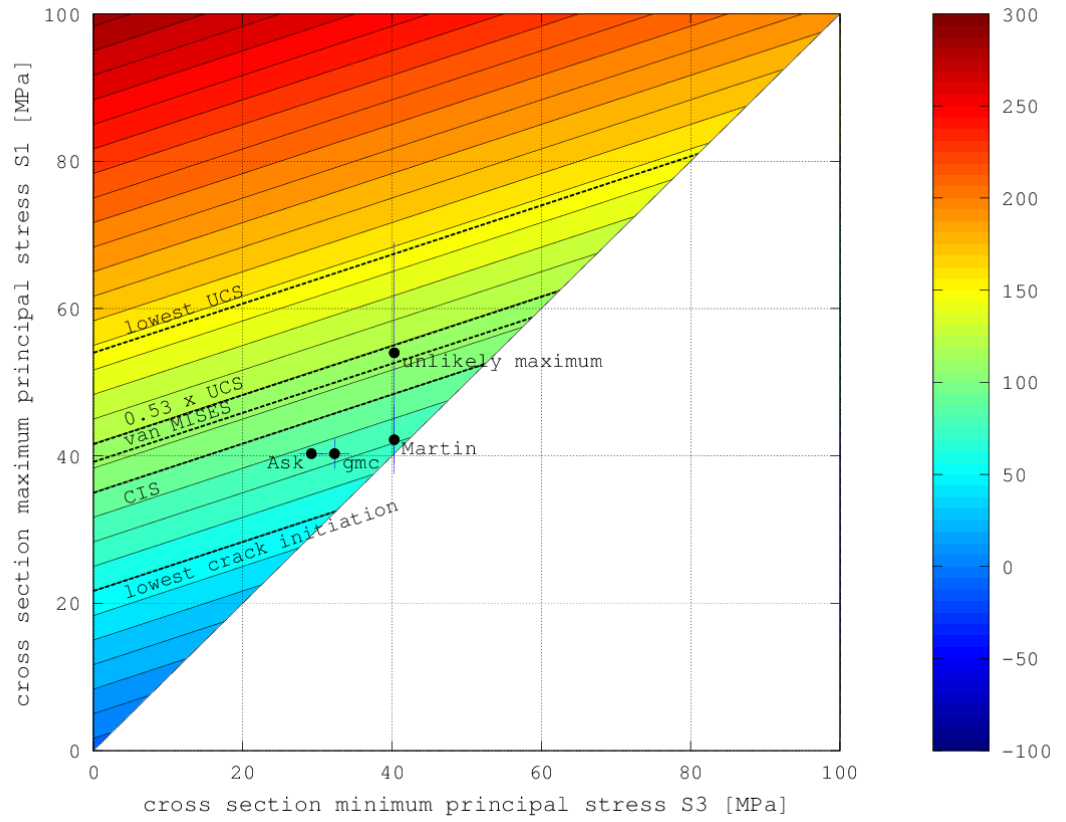


Figure A2.20. Spalling potential diagram for deposition tunnels model scenario #10. The colour code depicts tangential stress in [MPa].

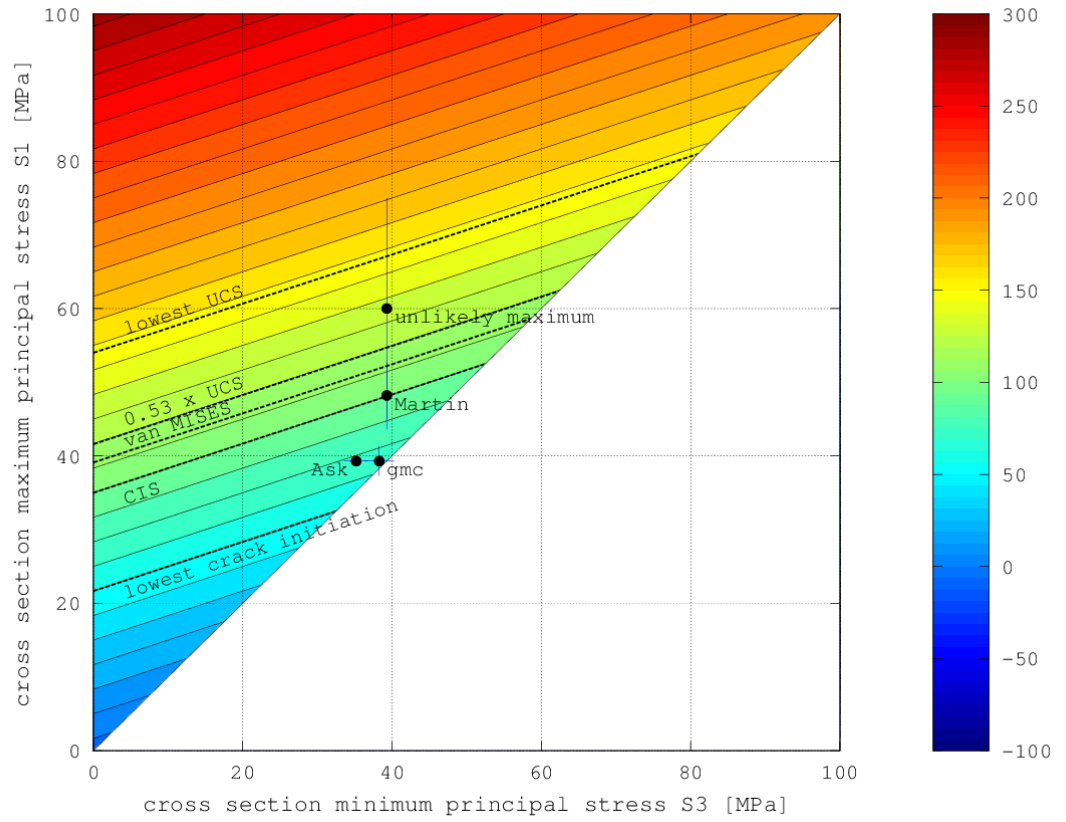


Figure A2.21. Spalling potential diagram for deposition tunnels model scenario #11. The colour code depicts tangential stress in [MPa].

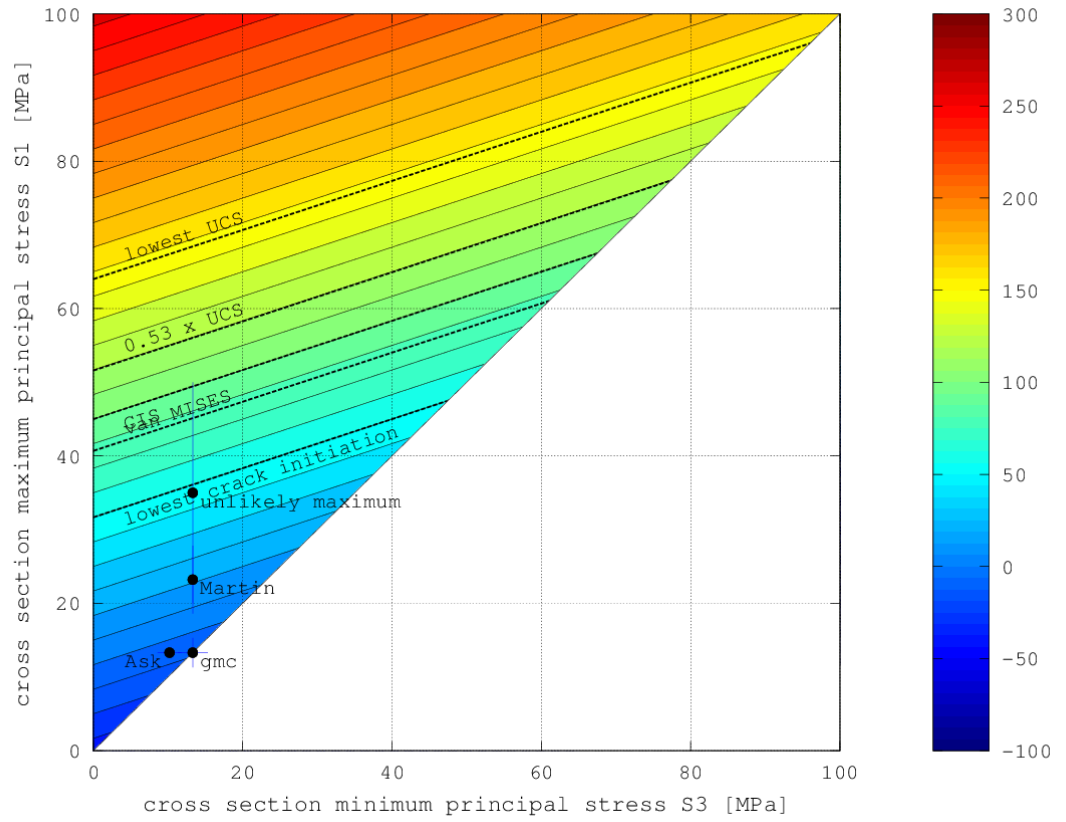


Figure A2.22. Spalling potential diagram for deposition tunnels model scenario #12. The colour code depicts tangential stress in [MPa].

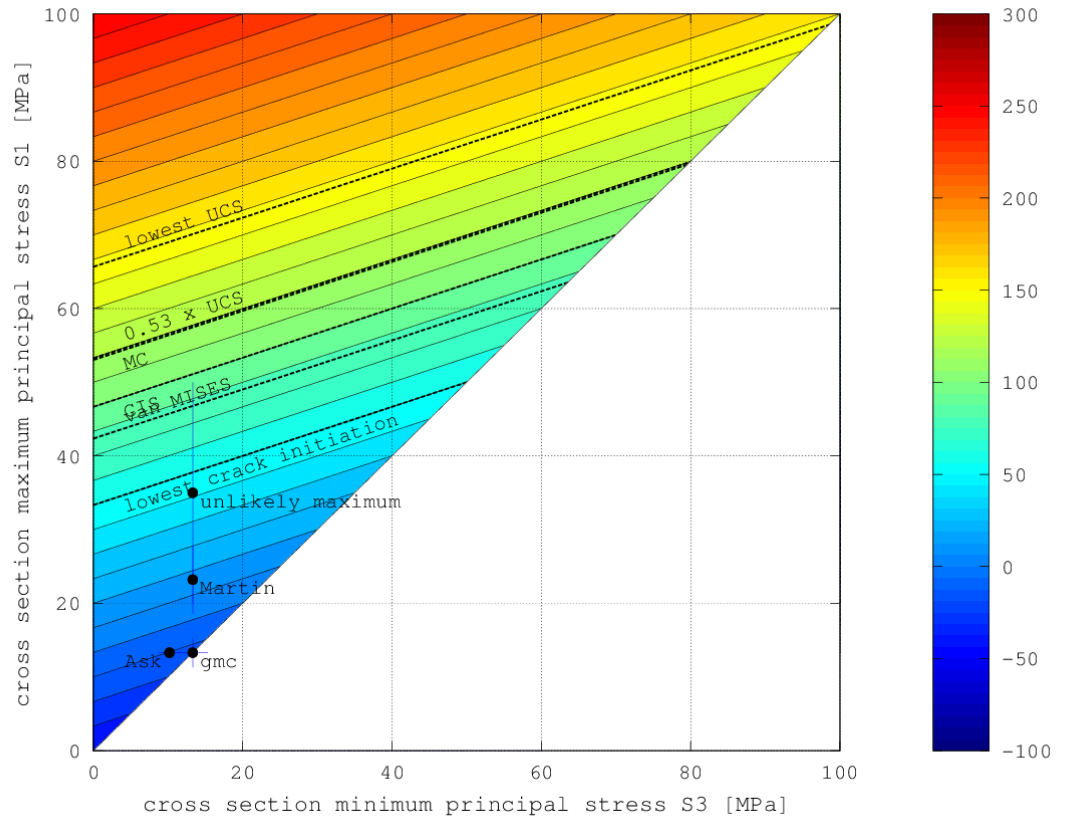


Figure A2.23. Spalling potential diagram for deposition tunnels model scenario #13. The colour code depicts tangential stress in [MPa].

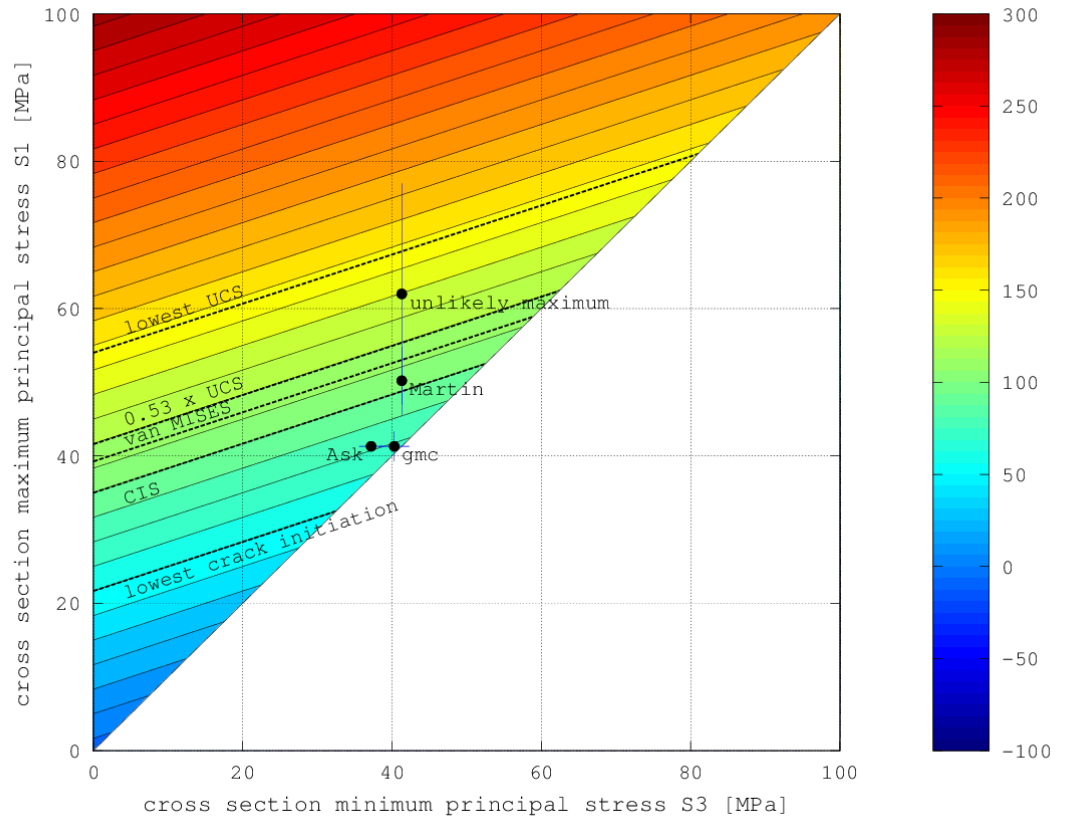


Figure A2.24. Spalling potential diagram for deposition tunnels model scenario #14. The colour code depicts tangential stress in [MPa].

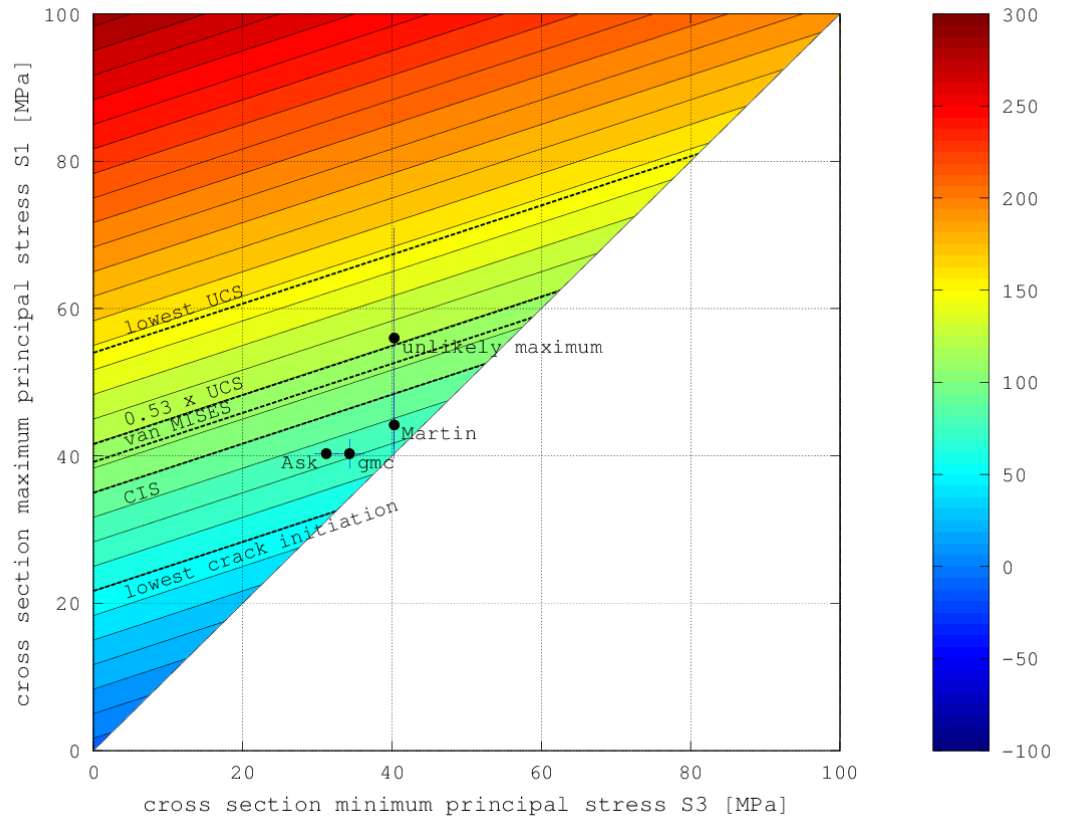


Figure A2.25. Spalling potential diagram for deposition tunnels model scenario #15. The colour code depicts tangential stress in [MPa].

Tensile failure in deposition holes

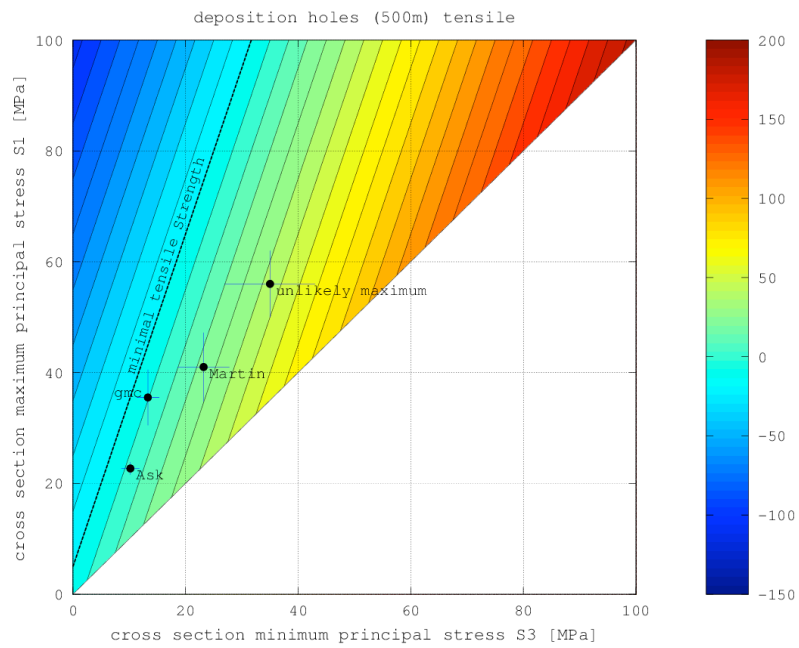


Figure A2.26. Tensile failure potential diagram for deposition holes during excavation (model scenario #1). The colour code depicts tangential stress in [MPa].

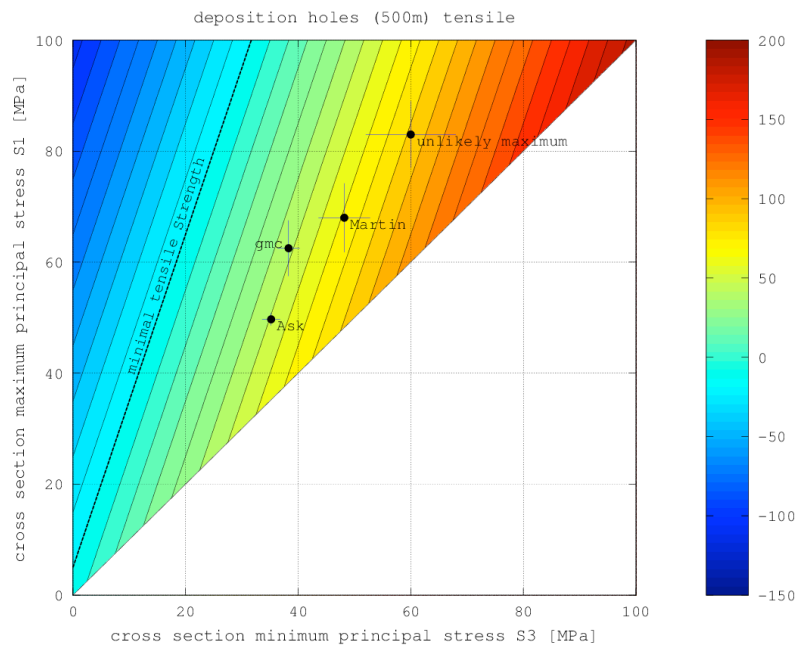


Figure A2.27. Tensile failure potential diagram for deposition holes during thermal phase (model scenario #2). The colour code depicts tangential stress in [MPa].

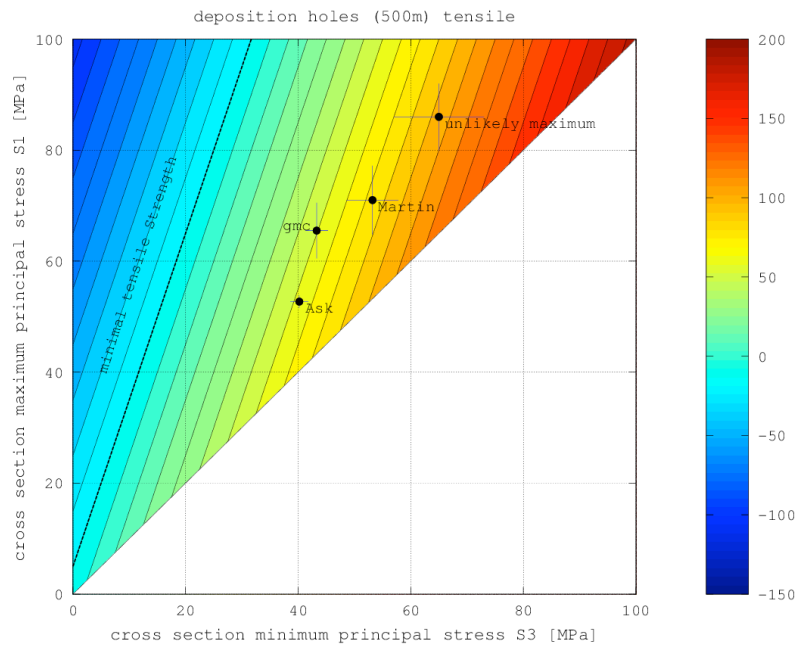


Figure A2.28. Tensile failure potential diagram for deposition holes during glaciation (model scenario #3). The colour code depicts tangential stress in [MPa].

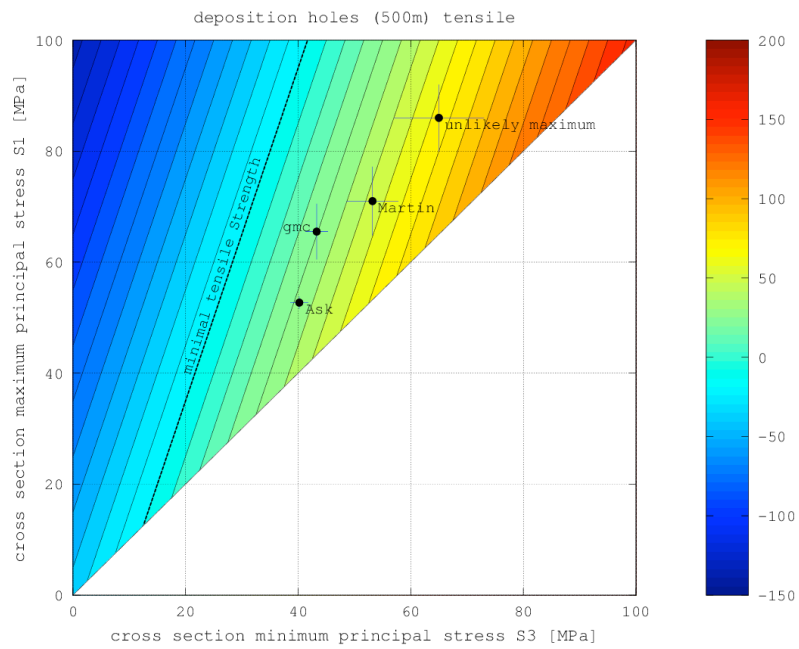


Figure A2.29. Tensile failure potential diagram for deposition holes during glaciation (model scenario #4). The colour code depicts tangential stress in [MPa].

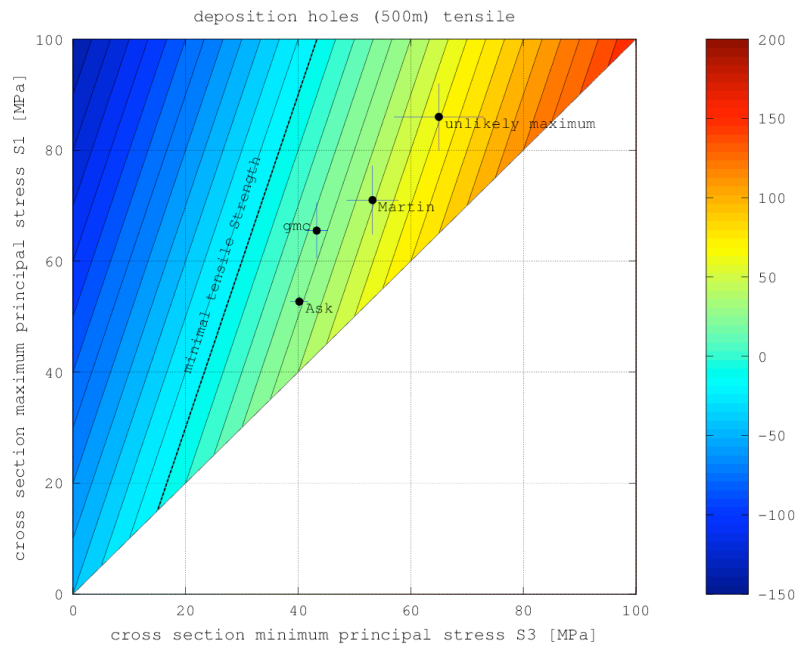


Figure A2.30. Tensile failure potential diagram for deposition holes during glaciation (model scenario #5). The colour code depicts tangential stress in [MPa].

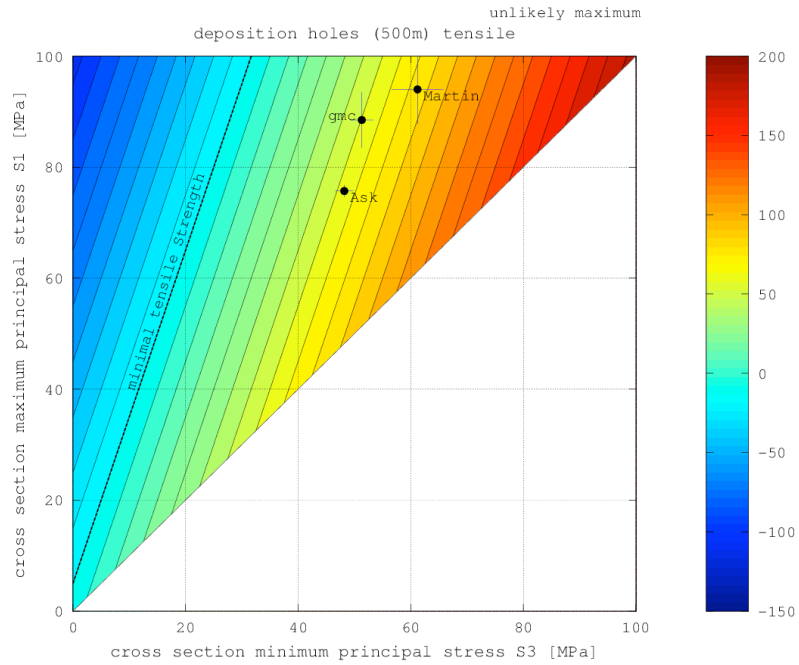


Figure A2.31. Tensile failure potential diagram for deposition holes during glaciation (model scenario #6). The colour code depicts tangential stress in [MPa].

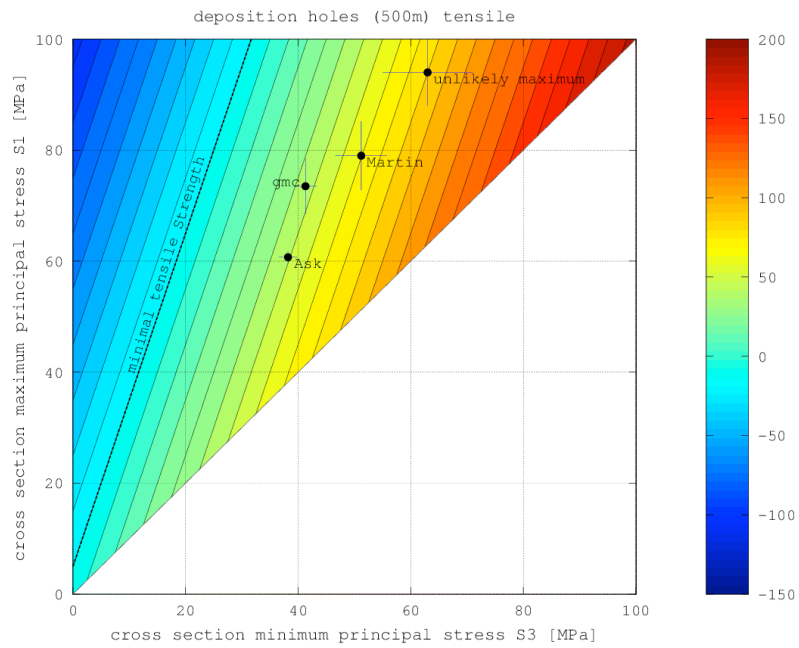


Figure A2.32. Tensile failure potential diagram for deposition holes during glaciation (model scenario #7). The colour code depicts tangential stress in [MPa].

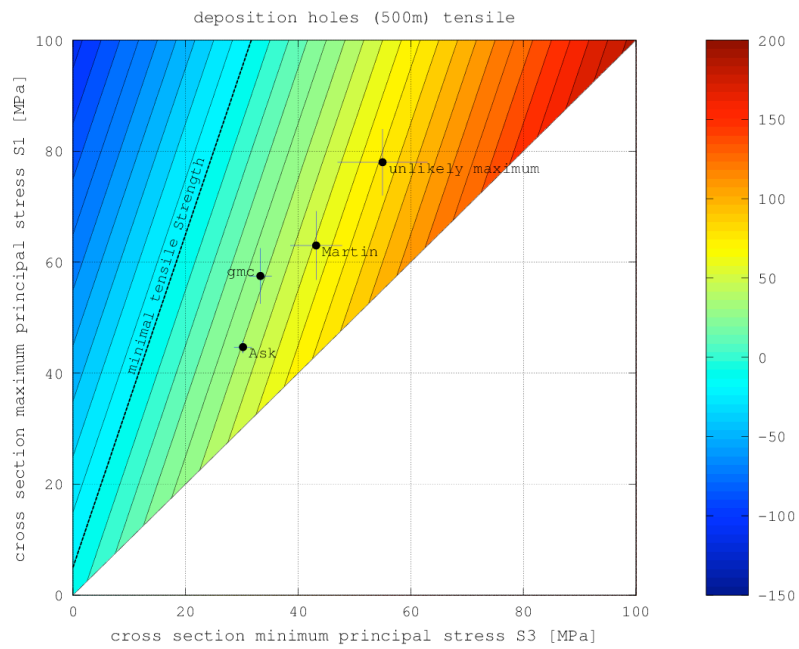


Figure A2.33. Tensile failure potential diagram for deposition holes during glaciation (model scenario #8). The colour code depicts tangential stress in [MPa].

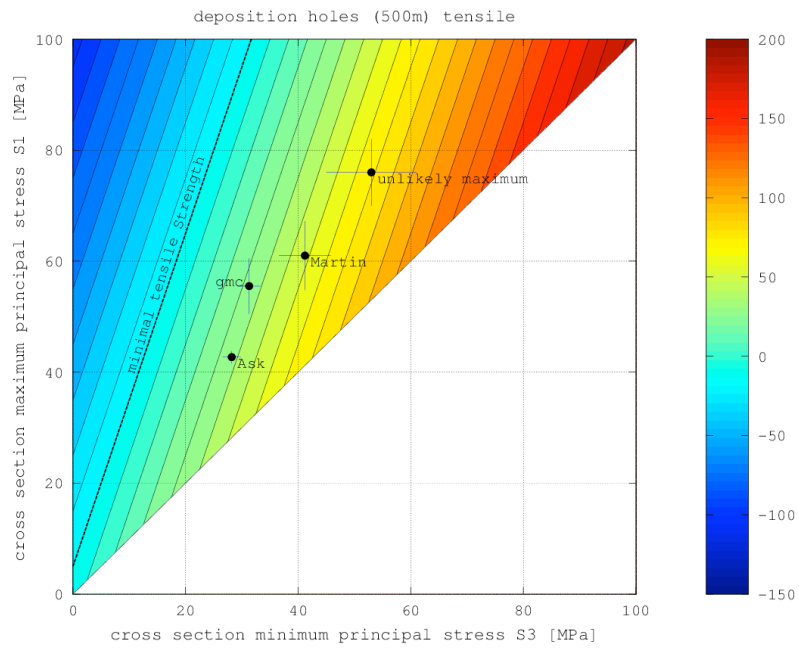


Figure A2.34. Tensile failure potential diagram for deposition holes during glaciation (model scenario #9). The colour code depicts tangential stress in [MPa].

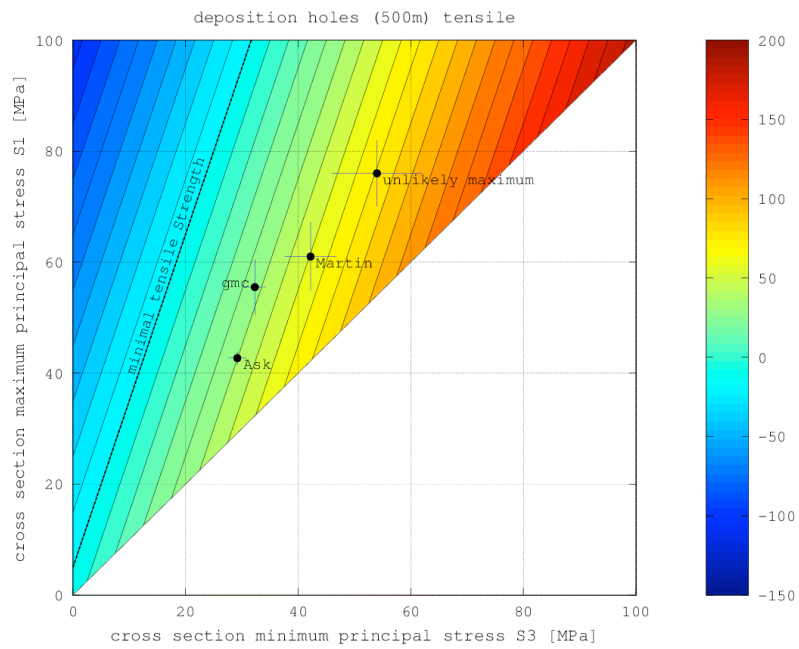


Figure A2.35. Tensile failure potential diagram for deposition holes during glaciation (model scenario #10). The colour code depicts tangential stress in [MPa].

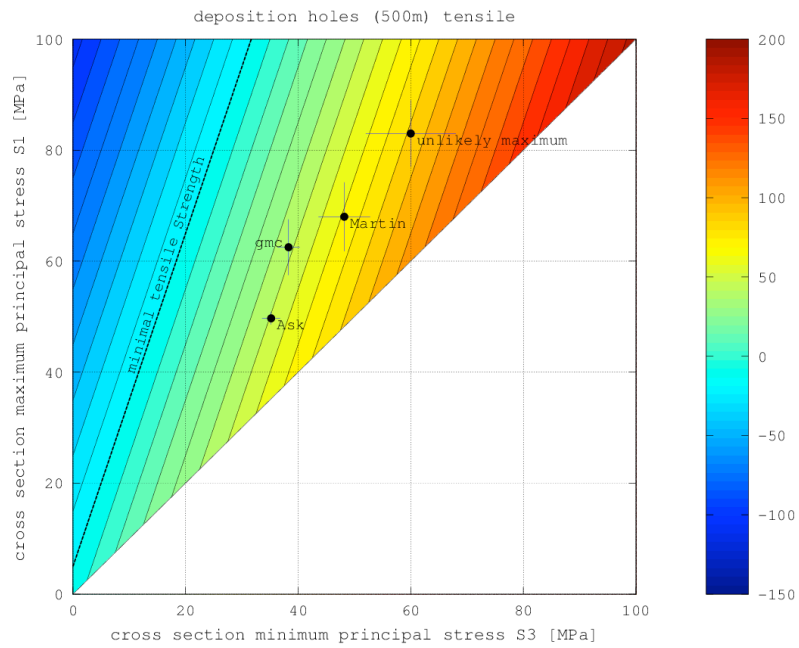


Figure A2.36. Tensile failure potential diagram for deposition holes during glaciation (model scenario #11). The colour code depicts tangential stress in [MPa].

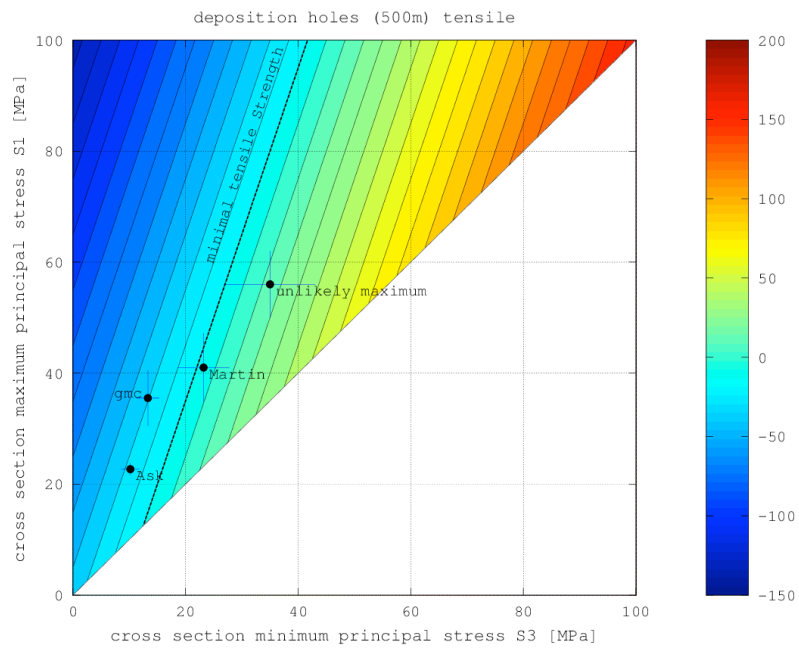


Figure A2.37. Tensile failure potential diagram for deposition holes during glaciation (model scenario #12). The colour code depicts tangential stress in [MPa].

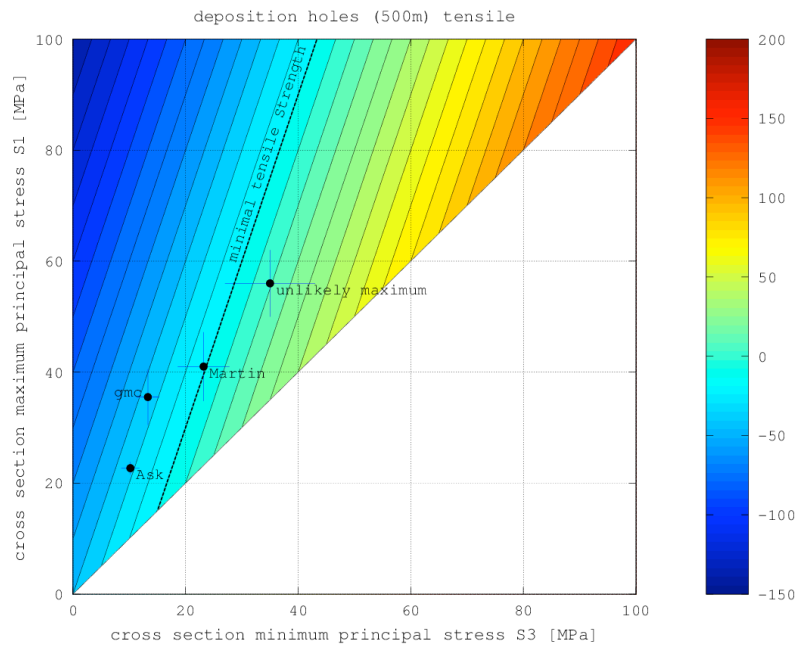


Figure A2.38. Tensile failure potential diagram for deposition holes during glaciation (model scenario #13). The colour code depicts tangential stress in [MPa].

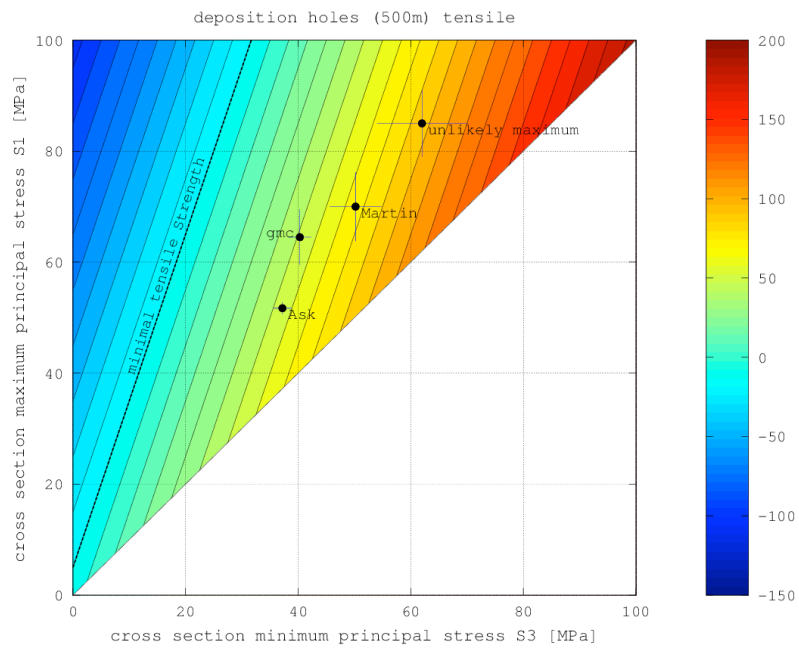


Figure A2.39. Tensile failure potential diagram for deposition holes during glaciation (model scenario #14). The colour code depicts tangential stress in [MPa].

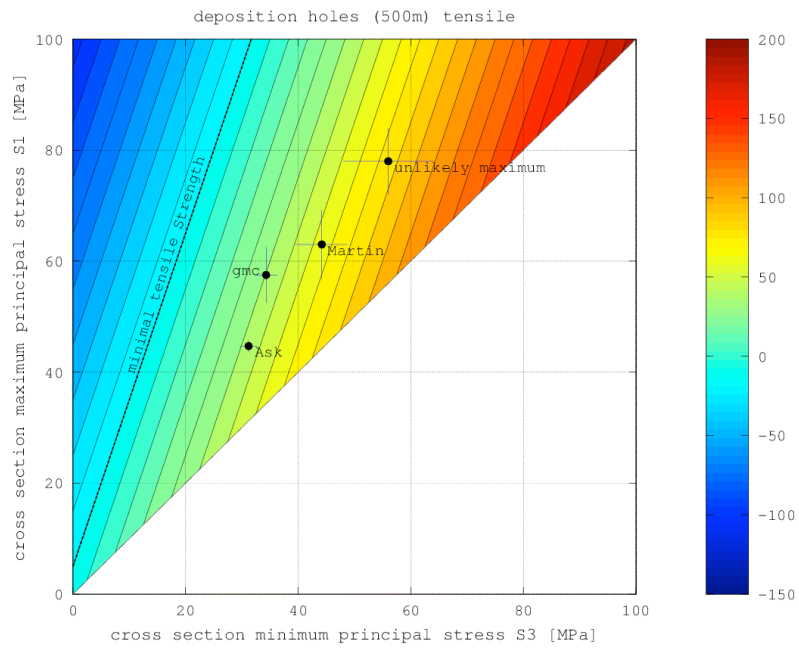


Figure A2.40. Tensile failure potential diagram for deposition holes during glaciation (model scenario #15). The colour code depicts tangential stress in [MPa].

Tensile failure in deposition tunnels

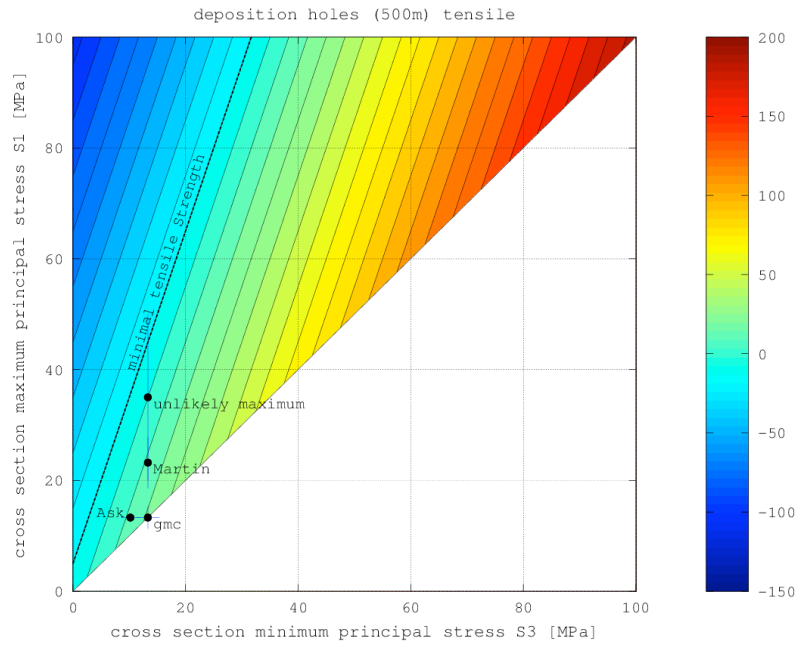


Figure A2.41. Tensile failure potential diagram for deposition tunnels (model scenario #1). The colour code depicts tangential stress in [MPa].

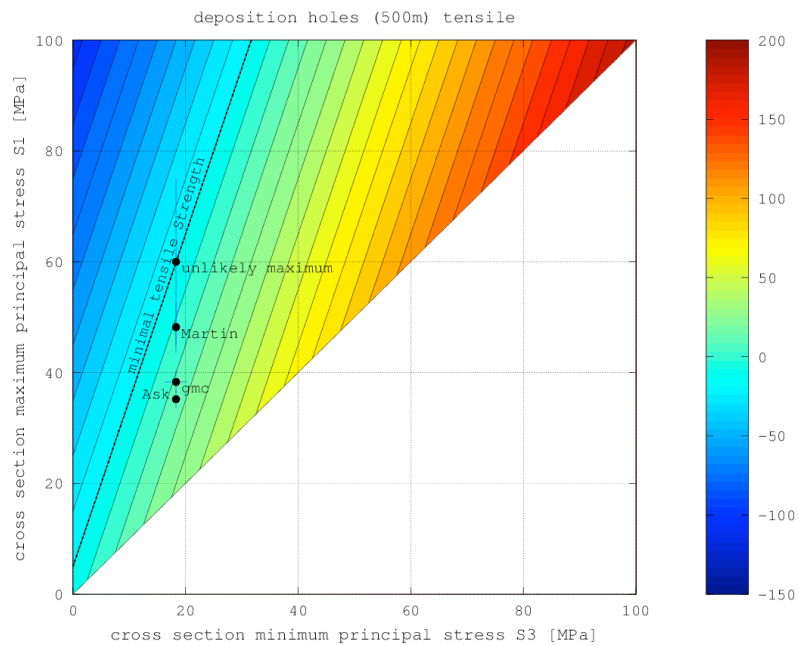


Figure A2.42. Tensile failure potential diagram for deposition tunnels (model scenario #2). The colour code depicts tangential stress in [MPa].

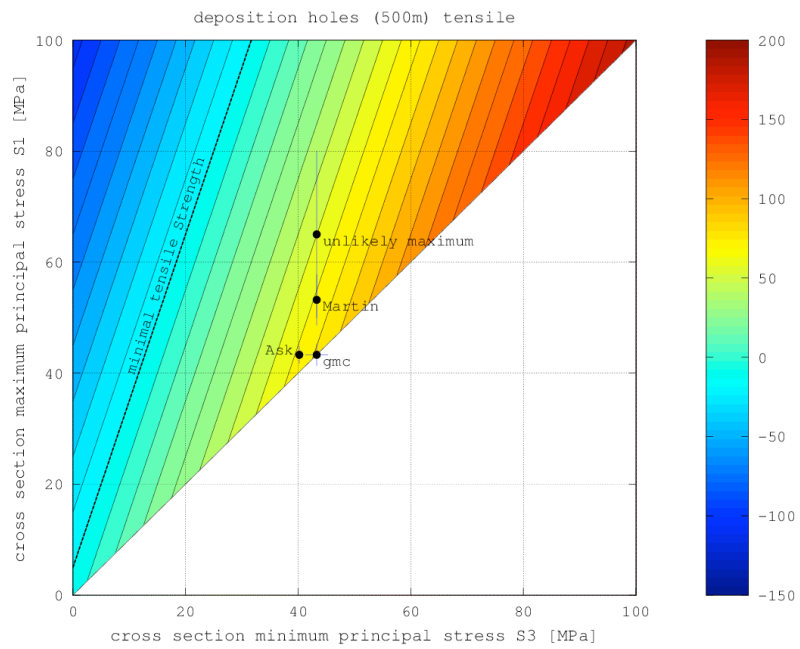


Figure A2.43. Tensile failure potential diagram for deposition tunnels (model scenario #3). The colour code depicts tangential stress in [MPa].

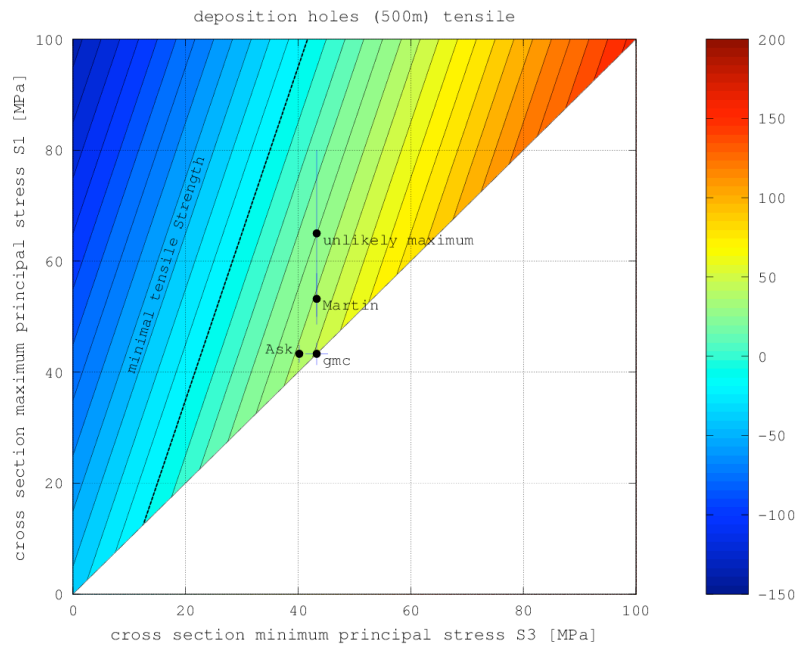


Figure A2.44. Tensile failure potential diagram for deposition tunnels (model scenario #4). The colour code depicts tangential stress in [MPa].

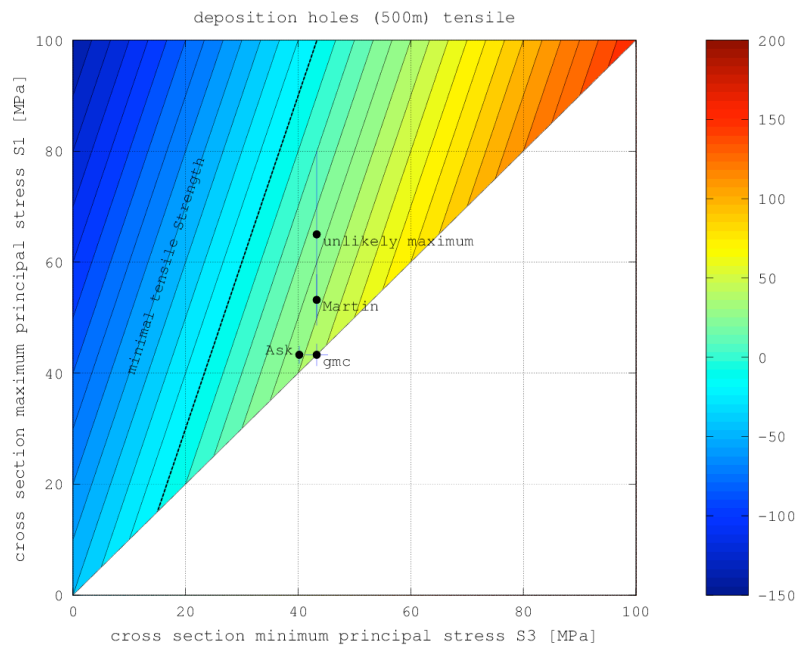


Figure A2.45. Tensile failure potential diagram for deposition tunnels (model scenario #5). The colour code depicts tangential stress in [MPa].

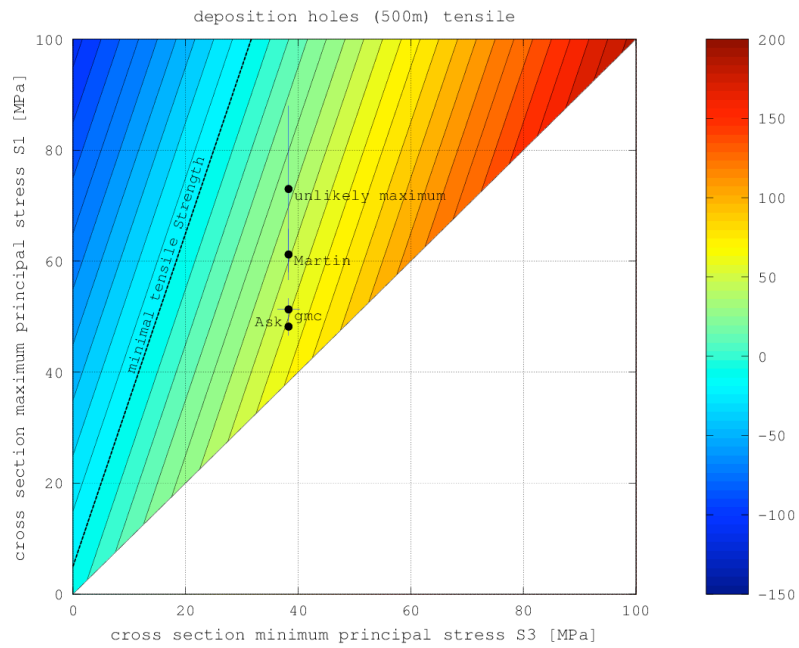


Figure A2.46. Tensile failure potential diagram for deposition tunnels (model scenario #6). The colour code depicts tangential stress in [MPa].

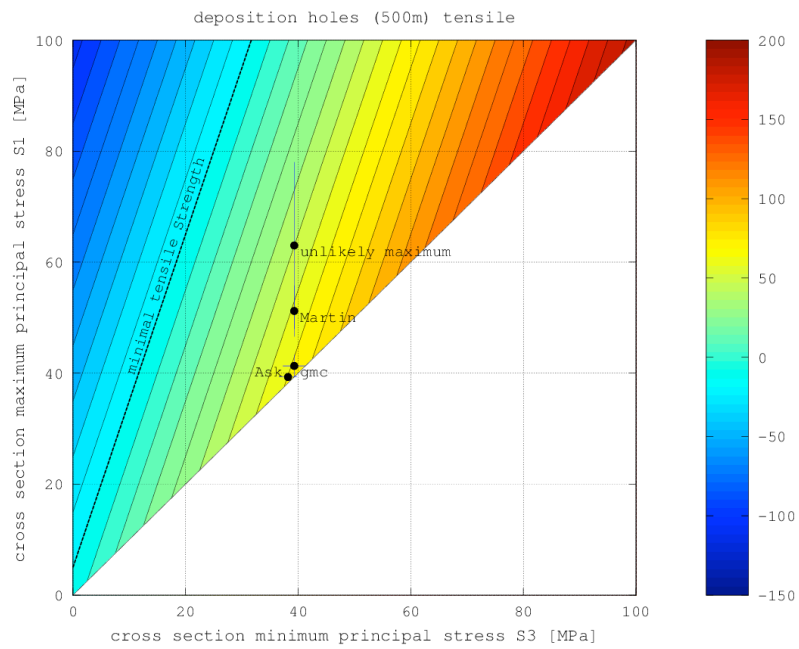


Figure A2.47. Tensile failure potential diagram for deposition tunnels (model scenario #7). The colour code depicts tangential stress in [MPa].

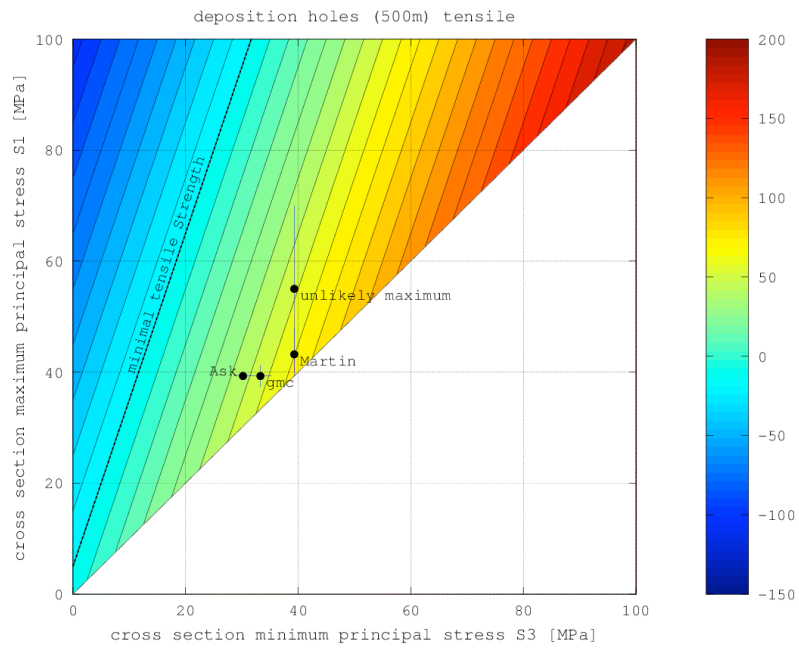


Figure A2.48. Tensile failure potential diagram for deposition tunnels (model scenario #8). The colour code depicts tangential stress in [MPa].

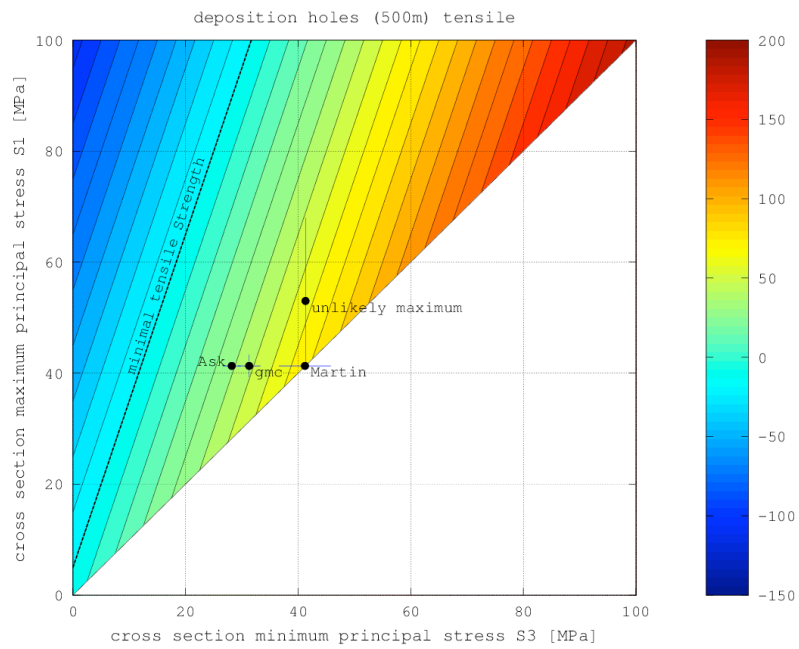


Figure A2.49. Tensile failure potential diagram for deposition tunnels (model scenario #9). The colour code depicts tangential stress in [MPa].

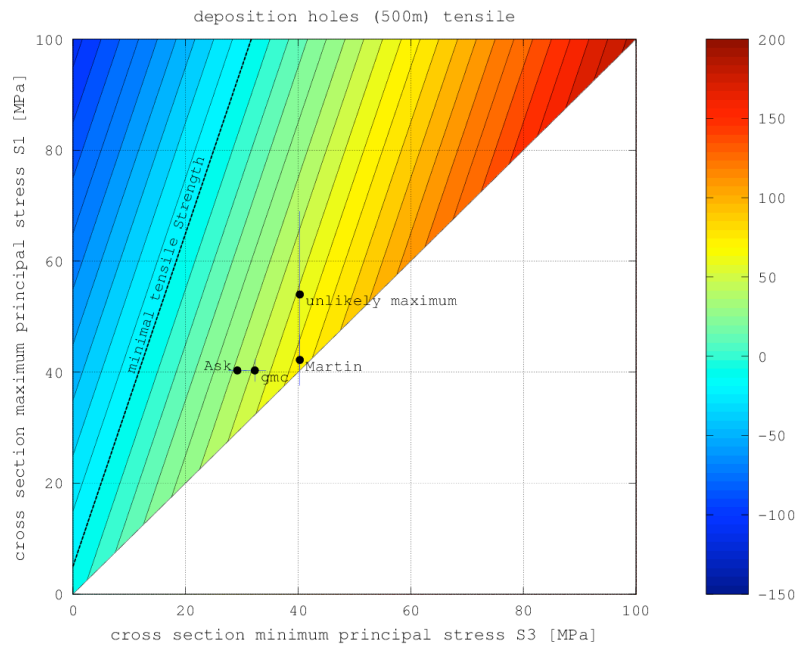


Figure A2.50. Tensile failure potential diagram for deposition tunnels (model scenario #10). The colour code depicts tangential stress in [MPa].

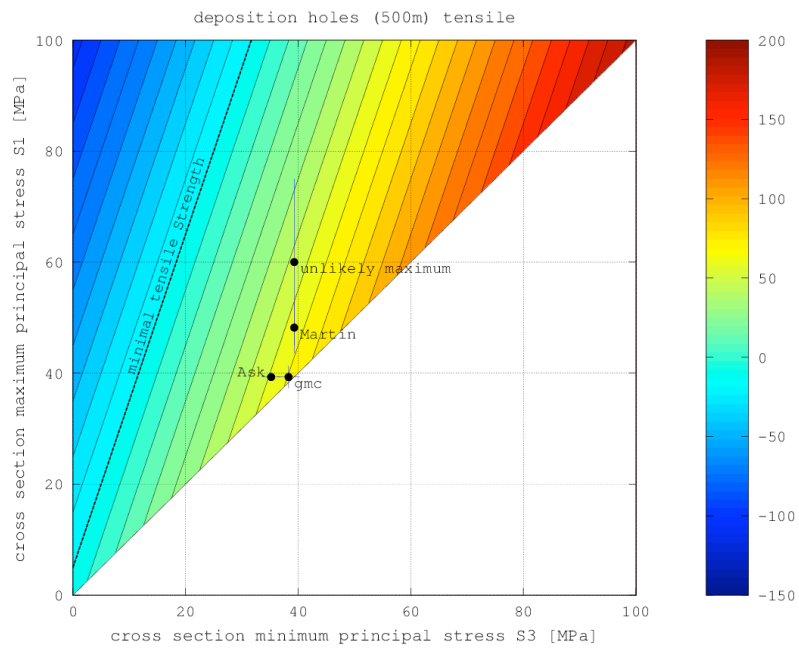


Figure A2.51. Tensile failure potential diagram for deposition tunnels (model scenario #11). The colour code depicts tangential stress in [MPa].

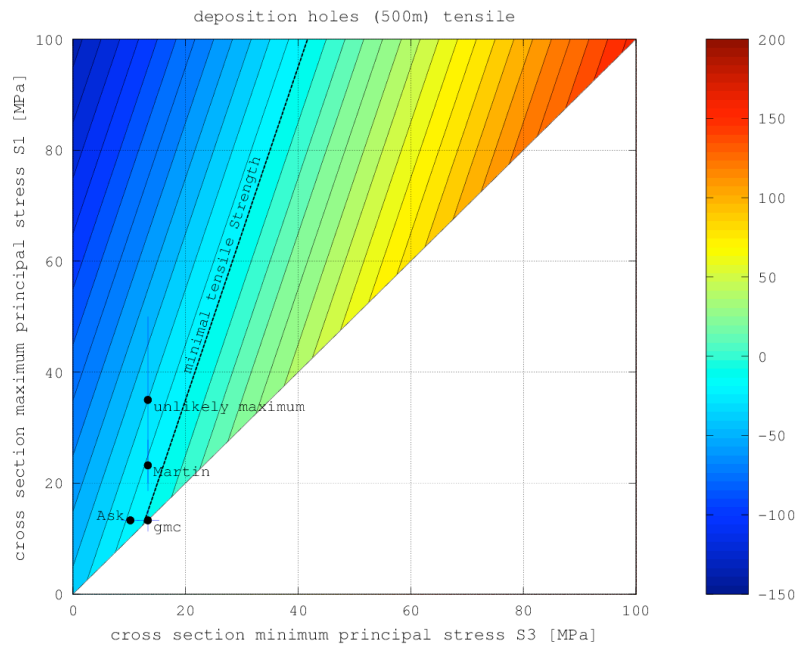


Figure A2.52. Tensile failure potential diagram for deposition tunnels (model scenario #12). The colour code depicts tangential stress in [MPa].

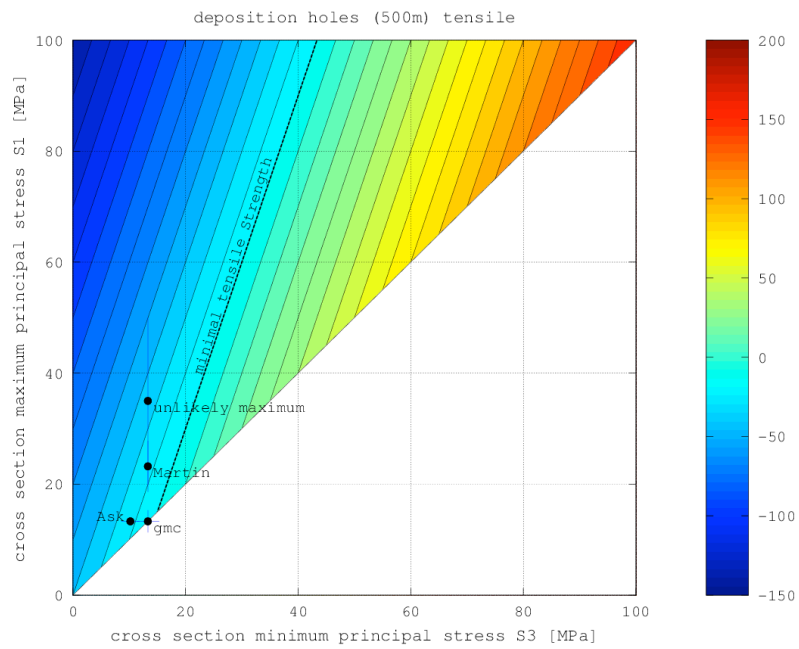


Figure A2.53. Tensile failure potential diagram for deposition tunnels (model scenario #13). The colour code depicts tangential stress in [MPa].

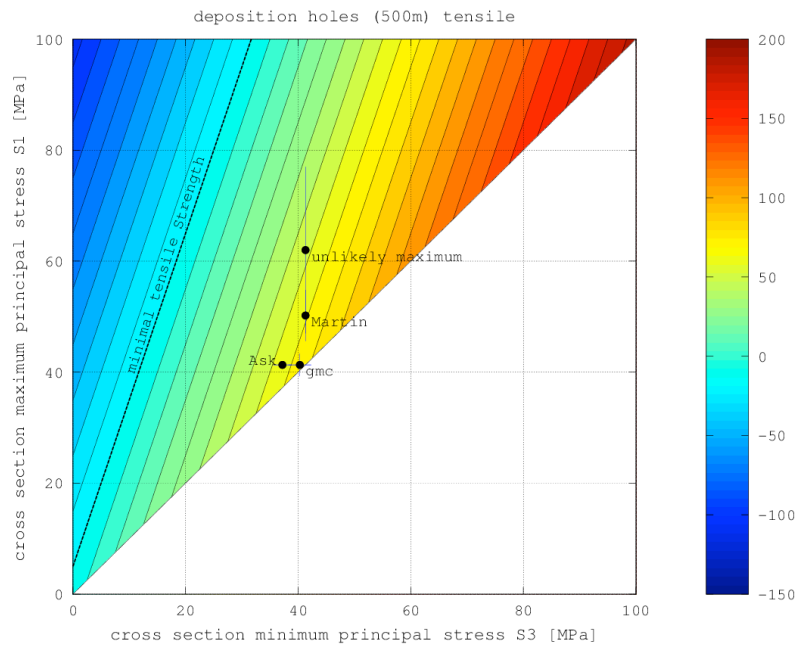


Figure A2.54. Tensile failure potential diagram for deposition tunnels (model scenario #14). The colour code depicts tangential stress in [MPa].

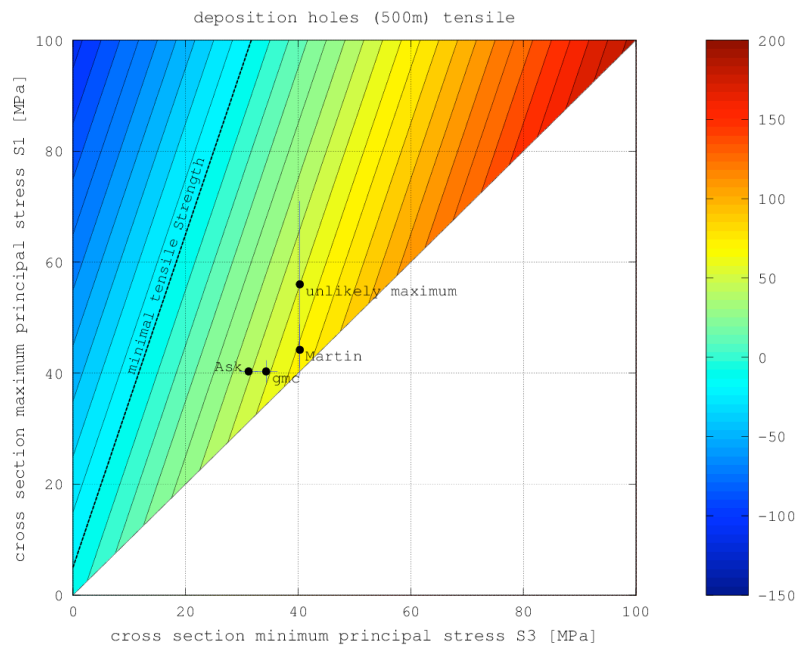


Figure A2.55. Tensile failure potential diagram for deposition tunnels (model scenario #15). The colour code depicts tangential stress in [MPa].

Stress data

Table A3.1. List of principal stresses as derived from stress measurements that were used for this report. The data is taken from the original reports as given in the first column, with exception of HF/HTPF data on borehole KFM04A, which was taken from Table B-2 in SKB TR-07-26.

Reference	Borehole	TVD [m]	measurement no.	S_v [MPa]	S_h [MPa]	S_H [MPa]	$\varphi (S_H)$ [°]	Rating
P-04-83	KFM01B	229,83	1:1:1					c
P-04-83	KFM01B	230,92	1:2:1					c
P-04-83	KFM01B	231,85	1:3:1					c
P-04-83	KFM01B	232,77	1:4:1	11,9	17,1	41	112	a
P-04-83	KFM01B	233,8	1:5:1	17,4	21,6	37,7	103	a
P-04-83	KFM01B	234,7	1:6:1					c
P-04-83	KFM01B	235,76	1:7:1	21,1	31,1	39,4	114	a
P-04-83	KFM01B	393,59	2:1:3					a
P-04-83	KFM01B	395,16	2:2:2					c
P-04-83	KFM01B	399,18	2:3:1	21,9	18,6	37,2	152	a
P-04-83	KFM01B	400,17	2:4:1					c
P-04-83	KFM01B	401,43	2:5:1					b
P-04-83	KFM01B	442,76	2:6:1					c
P-04-83	KFM01B	448,84	2:7:3					b
P-04-83	KFM01B	455,15	2:8:2	19,3	10,4	41,7	157	a
P-04-83	KFM01B	456,36	2:9:1					a
P-04-83	KFM01B	457,57	2:10:1					b
P-04-83	KFM01B	458,6	2:11:1					b
P-06-93	KFM07B	53,82	1:1:1	6	2,1	5,8	31	B
P-06-93	KFM07B	55,36	1:2:1	6,7	0,1	7,6	73	B
P-06-93	KFM07B	56,27	1:3:1	2,9	0	5,8	60	b

Reference	Borehole	TVD [m]	measurement no.	S _v [MPa]	S _h [MPa]	S _H [MPa]	φ (S _H) [°]	Rating
P-06-93	KFM07B	57	1:4:1	10,7	5,3	10	107	a
P-06-93	KFM07B	58,15	1:5:1	6,6	-1,1	13,4	32	b
P-07-130	KFM07C	98,29	1:1:5	4,3	19,2	27,9	177	a
P-07-130	KFM07C	104,03	1:2:4	3,4	10,5	25,7	168	b
P-07-130	KFM07C	107,9	1:4:1	3,8	10,1	21,1	178	b
P-07-130	KFM07C	157,46	2:1:3	-6,9	2,5	22,2	101	b
P-07-130	KFM07C	159,54	2:3:1	7	12,9	27,9	139	b
P-07-130	KFM07C	161,85	2:4:1	9	20,8	39,6	35	a
P-07-130	KFM07C	173,69	2:8:1	5,7	17,4	37,9	175	b
P-07-130	KFM07C	174,7	2:9:1	4,1	8,7	23,5	176	b
P-07-130	KFM07C	175,72	2:10:1	9,3	12,3	26,1	50	b
P-07-130	KFM07C	176,72	2:11:1	12,5	19,6	26,6	90	b
P-07-130	KFM07C	191,46	3:1:1	10,8	10,8	25,9	116	b
P-07-130	KFM07C	194,28	3:4:1	10,7	8,2	20,7	144	b
P-07-130	KFM07C	196,23	3:6:1	12,1	15,9	31	42	a
P-07-130	KFM07C	236,93	4:1:2	-0,2	9	26,9	28	b
P-07-130	KFM07C	241,4	4:2:3	24,8	21,9	44,7	140	b
P-07-130	KFM07C	257,35	4:4:2	11,9	11,8	32,1	0	b
P-07-205	KFM02B	112,25	1:7:1	0,2	3,7	10,7	115,6	b
P-07-205	KFM02B	134,02	1:13:3	-4,8	-0,8	7,1	171	b
P-07-205	KFM02B	142,28	1:17:2	3,2	4,8	14,2	125,1	b
P-07-205	KFM02B	154,66	2:1:3	12,5	4,3	12,2	167,9	a
P-07-205	KFM02B	161,94	2:3:4	1,6	4,9	6,8	120	b
P-07-205	KFM02B	175,68	2:6:2	2	-0,6	9,9	149,9	b
P-07-205	KFM02B	177,49	2:7:2	6	9	19,5	151,3	b
P-07-205	KFM02B	249,42	3:18:1	7,1	10,1	21,2	126,5	b
P-07-205	KFM02B	250,35	3:19:1	2,2	11	15,5	133,3	a
P-07-205	KFM02B	252,67	3:21:1	2,3	7,9	16,2	127,1	a
P-07-205	KFM02B	298,22	4:3:1	5,8	6,1	16,3	116,4	a
P-07-205	KFM02B	302,03	4:7:1	5,9	3,3	14,2	143,9	b

Reference	Borehole	TVD [m]	measurement no.	S _v [MPa]	S _h [MPa]	S _H [MPa]	φ (S _H) [°]	Rating
P-07-205	KFM02B	302,88	4:8:1	0,8	7,5	14,4	101	b
P-04-311	KFM01A	419	24		15,1	29,9	105	
P-04-311	KFM01A	452,87	8		11	21,6	121	
P-04-311	KFM01A	492,11	3		12,4	24,05	140	
P-04-311	KFM01A	498,03	2		17,2	33,75	86	
P-04-311	KFM01A	687,51	13		15,6	30,5	108	
P-04-311	KFM01A	939,52	11		26,9	54,9	87	
P-04-311	KFM01A	960,32	10		25,1	51,8	102	
P-04-311	KFM01B	183,46	2		5	8,1	77	
P-04-311	KFM02A	220,09	35		7,1	11,8	110	
P-04-311	KFM02A	222,88	34		6,8	10,7	125	
P-04-311	KFM02A	549,53	20		16,4	32,9	128	
P-04-311	KFM02A	600,58	12		18,3	37,5	137	
P-04-311	KFM02A	698,3	4		21,6	44,5	142	
P-04-311	KFM02A	701,08	3		22,6	47,5	136	
P-04-311	KFM04A	171,43			5,1	13,6	172	
P-04-311	KFM04A	173,47			5,2	13,6	125	
P-04-311	KFM04A	233,61			6,7	14,4	59	
P-04-311	KFM04A	243,63			7	14,5	131	
P-04-311	KFM04A	322,95			9,1	15,4	140	
P-04-311	KFM04A	345,3			9,6	15,7	120	
P-04-311	KFM04A	457,03			12,5	17	21	
P-04-311	KFM04A	471,33			12,9	17,2	99	
P-04-311	KFM04A	474,84			13	17,2	46	
P-04-311	KFM04A	479,34			13,1	17,3	114	

Reference	Borehole	TVD [m]	measurement no.	S _v [MPa]	S _h [MPa]	S _H [MPa]	φ (S _H) [°]	Rating
P-04-311	KFM04A	502,91			13,7	17,6	77	
P-07-206	KFM07A	270		6,5	13,1	15,2	127	
P-07-206	KFM07A	370		8,9	14,1	17,6	144	
P-07-206	KFM07A	470		11,2	14,9	20,2	151	
P-07-206	KFM07A	570		13,6	15,6	22,9	154	
P-07-206	KFM07A	670		16	16,2	25,6	155	
P-07-206	KFM07C	180			7	18,7	134	
P-07-206	KFM07C	300			9,8	18,9	134	
P-07-206	KFM07C	420			12,7	19,2	134	
P-07-206	KFM08A-2	580		12,6	8,4	20,1	153	
P-07-206	KFM08A-2	650		14,1	10,1	24,5	153	
P-07-206	KFM08A-2	720		15,6	11,8	28,9	153	
P-07-206	KFM08A-1	420		8,4	11,3	12,8	122	
P-07-206	KFM08A-1	455		9	10,8	14	122	
P-07-206	KFM08A-1	490		9,7	10,4	15,3	122	
P-07-206	KFM09A	450		9,8	1,8	11,9	108	
P-07-206	KFM09A	475		10,3	2,3	12,4	108	
P-07-206	KFM09A	500		10,9	2,8	12,9	108	
P-07-206	KFM09A	525		11,4	3,4	13,2	108	
P-07-206	KFM09A	550		12	3,9	13,8	108	
P-07-206	KFM09B	270		6	3	25,6	133	
P-07-206	KFM09B	310		6,9	5,6	28,1	133	
P-07-206	KFM09B	350		7,8	8,2	30,6	133	
P-07-206	KFM09B	390		8,7	10,8	33	133	
P-07-206	KFM09B	430		9,6	13,4	35,5	133	

Reference	Borehole	TVD [m]	measurement no.	S _v [MPa]	S _h [MPa]	S _H [MPa]	φ (S _H) [°]	Rating
P-07-206	KFM07A/C	170		5	7	19,4	117	
P-07-206	KFM07A/C	250		7,4	7,3	20	118	
P-07-206	KFM07A/C	330		9,8	7,7	20,5	118	
P-07-206	KFM07A/C	410		12,2	8,1	21,1	118	
P-07-206	KFM07A/C	490		14,6	8,4	21,6	118	
P-07-206	KFM07A/C const.	190			7,4	12	125	
P-07-206	KFM07A/C const.	290			8,3	15,5	125	
P-07-206	KFM07A/C const.	390			9,2	18,9	124	
P-07-206	KFM07A/C const.	490			10,1	22,4	124	
P-07-206	KFM09A/B	260		6	5,5	11,7	133	
P-07-206	KFM09A/B	320		7,4	7,3	20,5	128	
P-07-206	KFM09A/B	380		8,7	9,1	29,4	127	
P-07-206	KFM09A/B	440		10,1	10,9	38,3	126	
P-07-206	KFM09A/B	500		11,5	12,7	47,1	126	
P-03-319	DBT-1	133,61	3:1	2,9	13,4	15	148,3	
P-03-319	DBT-1	134,18	3:2	8	10,8	14,4	118,9	
P-03-319	DBT-1	134,74	3:3	12,2	10,4	15,8	94,2	
P-03-319	DBT-1	136,41	3:4	9,2	12	16,3	99,9	
P-03-319	DBT-1	165,54	4:1	4,6	12	13,3	49,9	
P-03-319	DBT-1	166,8	4:2	6,6	14,9	23,7	90,7	
P-03-319	DBT-1	194,77	5:1	7,1	18,5	22,2	96,3	
P-03-319	DBT-1	195,39	5:2	-4,8	11,3	18,6	102,7	
P-03-319	DBT-1	218,9	6:1	8,2	17,7	18,2	31,2	
P-03-319	DBT-1	219,63	6:2	9,2	16,6	21,7	13,9	
P-03-319	DBT-1	246,94	6:3	9,1	11,1	18,4	44,7	

Reference	Borehole	TVD [m]	measurement no.	S _v [MPa]	S _h [MPa]	S _H [MPa]	φ (S _H) [°]	Rating
P-03-319	DBT-1	75,65	7:1	9,8	20,1	40,3	142,6	
P-03-319	DBT-1	276,31	7:2	10,5	20,3	37,4	90	
P-03-319	DBT-1	299,71	8:1	10	13,7	21,4	129	
P-03-319	DBT-1	300,34	8:2	8,7	10,6	24,8	152,7	
P-03-319	DBT-1	374,63	9:1	6,5	29,3	42,2	149,1	
P-03-319	DBT-1	377,37	9:2	6,3	26	42,4	165	
P-03-319	DBT-1	378,16	9:3	3,9	22	46,6	122,3	
P-03-319	DBT-1	422,59	10:1	13,7	42,3	63	129,1	
P-03-319	DBT-1	460,48	10:2	22,2	33,1	59,3	139,1	
P-03-319	DBT-1	485,72	11:1	32,8	45,9	66,1	118,6	
P-03-319	DBT-1	499,87	11:2	16,3	28,8	56,6	158,5	
P-03-319	DBT-1	501,76	11:3	14,7	35,8	53,9	154,6	
P-03-319	DBT-3	133,61	4:1	3,6	9,5	21	132,9	
P-03-319	DBT-3	134,18	4:2	0,5	10,8	22,4	161,8	
P-03-319	DBT-3	134,74	4:3	3,6	7,5	17	133,1	
P-03-319	DBT-3	136,41	5:1	8,2	12,4	22,8	136,9	
P-03-319	DBT-3	165,54	5:2	9,7	9	18,1	140,1	
P-03-319	DBT-3	166,8	5:3	-1,2	5,6	20,1	134,1	
P-03-319	DBT-3	194,77	6:1	7,5	8,9	18,8	1,7	
P-03-319	DBT-3	195,39	6:2	10,8	13,1	17,6	145,9	
P-03-319	DBT-3	218,9	7:1	12,9	12,7	31,5	141	
P-03-319	DBT-3	219,63	7:2	5,5	8,1	13,4	22,1	
P-03-319	DBT-3	246,94	8:1	10,7	12,4	19,4	176,9	
P-03-319	DBT-3	75,65	8:2	5	6,4	17,1	162,4	
P-03-319	DBT-3	276,31	8:3	8,6	17	22,8	11,3	

Reference	Borehole	TVD [m]	measurement no.	S_v [MPa]	S_h [MPa]	S_H [MPa]	$\varphi (S_H)$ [°]	Rating
P-03-319	DBT-3	299,71	9:1	-0,8	11,9	27,6	174,8	
P-03-319	DBT-3	300,34	9:2	8	14,9	20,1	147,8	



2014:10

The Swedish Radiation Safety Authority has a comprehensive responsibility to ensure that society is safe from the effects of radiation. The Authority works to achieve radiation safety in a number of areas: nuclear power, medical care as well as commercial products and services. The Authority also works to achieve protection from natural radiation and to increase the level of radiation safety internationally.

The Swedish Radiation Safety Authority works proactively and preventively to protect people and the environment from the harmful effects of radiation, now and in the future. The Authority issues regulations and supervises compliance, while also supporting research, providing training and information, and issuing advice. Often, activities involving radiation require licences issued by the Authority. The Swedish Radiation Safety Authority maintains emergency preparedness around the clock with the aim of limiting the aftermath of radiation accidents and the unintentional spreading of radioactive substances. The Authority participates in international co-operation in order to promote radiation safety and finances projects aiming to raise the level of radiation safety in certain Eastern European countries.

The Authority reports to the Ministry of the Environment and has around 300 employees with competencies in the fields of engineering, natural and behavioural sciences, law, economics and communications. We have received quality, environmental and working environment certification.

Strålsäkerhetsmyndigheten
Swedish Radiation Safety Authority

SE-171 16 Stockholm
Solna strandväg 96
SSM 2014:10

Tel: +46 8 799 40 00
Fax: +46 8 799 40 10

E-mail: registrator@ssm.se
Web: stralsakerhetsmyndigheten.se